



AFAL TR-87-029

AD:

Final Report
for the period
October 1982 to
December 1986

Measurements of Particulates in Solid Propellant Rocket Motors

October 1987

Authors:
T. D. Edwards
R. K. Harris
K. G. Horton
M. G. Keith
A. Kertadidjaja
Y. S. Lee
D. N. Redman

Naval Postgraduate School
Monterey, CA 93943

F04611-83-X-0010

Approved for Public Release

Distribution is unlimited. The AFAL Technical Services Office has reviewed this report, and it is releasable to the National Technical Information Service, where it will be available to the general public, including foreign nationals.

Prepared for the: **Air Force
Astronautics
Laboratory**

Air Force Space Technology Center
Space Division, Air Force Systems Command
Edwards Air Force Base,
California 93523-5000

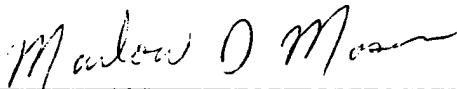
NOTICE

When U.S. Government drawings, specifications, or other data are used for any purpose other than a definitely related Government procurement operation, the fact that the Government may have formulated, furnished, or in any way supplied the said drawings, specifications, or other data, is not to be regarded by implication or otherwise, or in any way licensing the holder or any other person or corporation, or conveying any rights or permission to manufacture, use, or sell any patented invention that may be related thereto.

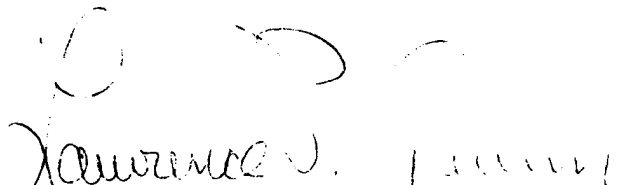
FOREWORD

This final report describes the work performed by the Naval Postgraduate School, Monterey, CA, under procurement identification number F04611-83-X-0010 for the Air Force Astronautics Laboratory (AFAL), Edwards Air Force Base, CA, 93523-5000. AFAL Project Manager was Lt Marlow Moser.

This report has been reviewed and is approved for release and distribution in accordance with the distribution statement on the cover and on the DD Form 1473.

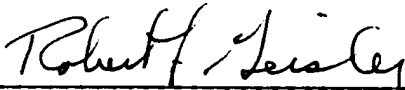


MARLOW D. MOSER, 1LT, USAF
Project Manager



LAWRENCE P. QUINN
Chief, Aerothermochemistry Branch

FOR THE COMMANDER



ROBERT L. GEISLER
Deputy Chief, Propulsion Analysis Division

REPORT DOCUMENTATION PAGE				Form Approved OMB No. 0704-0188		
1a. REPORT SECURITY CLASSIFICATION UNCLASSIFIED			1b. RESTRICTIVE MARKINGS			
2a. SECURITY CLASSIFICATION AUTHORITY			3. DISTRIBUTION/AVAILABILITY OF REPORT Approved for public release; distribution is unlimited.			
2b. DECLASSIFICATION/DOWNGRADING SCHEDULE						
4. PERFORMING ORGANIZATION REPORT NUMBER(S)			5. MONITORING ORGANIZATION REPORT NUMBER(S) AFAL-TR-87-029			
6a. NAME OF PERFORMING ORGANIZATION Naval Postgraduate School		6b. OFFICE SYMBOL (If applicable)	7a. NAME OF MONITORING ORGANIZATION Air Force Astronautics Laboratory			
6c. ADDRESS (City, State, and ZIP Code) Monterey, CA 93943			7b. ADDRESS (City, State, and ZIP Code) DYCC Edwards AFB CA 93523-5000			
8a. NAME OF FUNDING/SPONSORING ORGANIZATION		8b. OFFICE SYMBOL (If applicable)	9. PROCUREMENT INSTRUMENT IDENTIFICATION NUMBER F04611-83-X-0010			
8c. ADDRESS (City, State, and ZIP Code)			10. SOURCE OF FUNDING NUMBERS			
			PROGRAM ELEMENT NO. 62302F	PROJECT NO. 5730N	TASK NO. 00	WORK UNIT ACCESSION NO. DD
11. TITLE (Include Security Classification) MEASUREMENTS OF PARTICULATES IN SOLID PROPELLANT ROCKET MOTORS (U)						
12. PERSONAL AUTHOR(S) Edwards, T.D., Harris, R.K., Horton, K.G., Keith, M.G., Kertadidjaja, A., Lee, Y.S., Redman, D.N., Rosa, J.S., Rubin, J.B., Yoon, S.C., Powers, J.P., and Netzer, D.W.						
13a. TYPE OF REPORT Final		13b. TIME COVERED FROM 82/10 TO 86/12		14. DATE OF REPORT (Year, Month, Day) 87/10		
15. PAGE COUNT 96						
16. SUPPLEMENTARY NOTATION Other procurement instrument identification numbers used include: F04611-85-X-0001 and F04611-86-X-0008.						
17. COSATI CODES			18. SUBJECT TERMS (Continue on reverse if necessary and identify by block number)			
FIELD	GROUP	SUB-GROUP	Solid Propellants, Particle Sizing, Holograms, Particulates, Optical Methods, Speckel Reduction			
21	08	2				
19. ABSTRACT (Continue on reverse if necessary and identify by block number) An investigation has been conducted to develop techniques for obtaining quantitative data that can be used to relate solid rocket propellant composition and operating environment to the behavior of solid particulates within the grain port and exhaust nozzle. The techniques employed are high speed motion pictures of propellant strand burners and slab burners in a cross-flow environment, SEM analysis of post-fire residue (strand, slab, and motor), determination of D_{32} across the exhaust nozzle using measurements of scattered laser light, and holograms of burning propellant strands, slabs, and motors. In addition, techniques are being developed for automatic retrieval of particle size distributions from holograms taken of the combustion of solid propellants. Results are presented on (1) the measurement of particle size changes across an exhaust nozzle, (2) holograms obtained at the nozzle entrance, and (3) automatic data retrieval from holograms.						
20. DISTRIBUTION/AVAILABILITY OF ABSTRACT <input type="checkbox"/> UNCLASSIFIED/UNLIMITED <input checked="" type="checkbox"/> SAME AS RPT. <input type="checkbox"/> DTIC USERS			21. ABSTRACT SECURITY CLASSIFICATION UNCLASSIFIED			
22a. NAME OF RESPONSIBLE INDIVIDUAL Marlow D. Moser, 1Lt, USAF			22b. TELEPHONE (Include Area Code) (805) 275-5442		22c. OFFICE SYMBOL DYCC	

TABLE OF CONTENTS

	<u>Page</u>
INTRODUCTION	1
DETERMINATION OF PARTICLE SIZE USING/MEASUREMENTS OF SCATTERED	2
LIGHT	
Experimental Apparatus and Procedures	4
Motor Components	4
Light Scattering Measurement Apparatus	7
System Calibrations	12
Results from Motor Firings	28
Nozzle Exhaust Measurements	28
Nozzle Entrance Measurements	36
Conclusions from Initial Tests	36
Results from Motor Firings - Particle Injection	36
Glass Beads Injection	39
Aluminum Oxide Injection	39
System Problems	43
Conclusions from Particle Injection Tests	44
HOLOGRAPHIC INVESTIGATION	44
Description of Apparatus	45
Holographic Apparatus	45
Motor	47
System Calibration	47
Results from Motor Firings	51
Conclusion from Holographic Investigation	53
AUTOMATIC DATA RETRIEVAL FROM HOLOGRAMS	53
Holographic Reconstruction	54
Image Digitization and Processing	54
Thresholding	57

Test Objects	57
Sizing Investigation	59
Measurement Results	61
Speckle	61
Speckle Reduction Filters	68
The Sigma Filter	68
The Local Statistics Filter	70
The Geometric Filter	75
Comparison of the Filters	76
Speckle Index Comparison	76
Resolution Comparison	79
Time Comparison	79
Visual Comparison	79
Histogram Comparison	80
CONCLUSIONS, RECOMMENDATIONS AND CURRENT EFFORTS	80
REFERENCES	84

LIST OF FIGURES

<u>Figure</u>	<u>Caption</u>	<u>Page</u>
1	Dimensions of Small Solid Propellant Rocket Motor	5
2	Long Motor on Test Stand	5
3	Motor Components	6
4	Experimental Apparatus, Vertical Motor Mounting	6
5	Particle Feed Apparatus	8
6	Schematic of Small Motor	8
7	Schematic of Particle Feed Apparatus	9
8	Schematic of Scattered Light Measurement Apparatus	10
9	Experimental Apparatus, Horizontal Motor Mounting	11
10	Calibration Profile, 85% Transmitted Light	13
11	Calibration Profile, 30% Transmitted Light	14
12	Calibration Profiles, Slope Sensitivity to Particle Size	16
13	Fraction of Total Scattered Light Collected as Function of θ and $\Delta\theta$	19
14	Effect of Exhaust on Transmitted Light, Nonmetallized GAP/AP Propellant	20
15	Effect of Exhaust on Transmitted Light, Nonmetallized HTPB/AP Propellant	22
16	Effect of Exhaust on Transmitted Light, 2% Aluminized Propellant	23
17	Scattered Light Profile from Exhaust Jet, Nonmetallized Propellant	24
18	Effect of Combustion Products on Motor Path Transmittance, Preburn	26
19	Effect of Combustion Products on Motor Path Transmittance, During Burn	27
20	SEM Photographs of Collected Exhaust Products, 4.8% Aluminum	29

LIST OF FIGURES (CONTINUED)

<u>Figure</u>	<u>Caption</u>	<u>Page</u>
21	Scattered Light Profile from Exhaust Jet, 4.8% Aluminum, $P_c = 328$ psig	31
22	Scattered Light Profile from Exhaust Jet, 4.8% Aluminum, $P_c = 450$ psig	32
23	Scattered Light Profile from Exhaust Jet, 2% Aluminum, $P_c = 296$ psig	33
24	Scattered Light Profile from Exhaust Jet, 2% Aluminum, $P_c = 566$ psig	34
25	SEM Photographs of Collected Combustion Products, 2% Aluminum Propellant	35
26	SEM Photographs of Collected Motor Cavity Products, 4.8% Aluminum Propellant	37
27	SEM Photograph of Collected Motor Cavity Products, 2% Aluminum Propellant	38
28	Scattered Light Profile Through Motor, Glass Bead Injection, $P_c = 320$ psig	40
29	Scattered Light Profile Through Exhaust Jet, Glass Bead Injection, $P_c = 320$ psig	41
30	Q-Switched, Pulsed Ruby Laser	46
31	Holocamera Surrounding Vertically Mounted Motor	46
32	Schematic of Image Recording Apparatus	48
33	Hologram Reconstruction Apparatus	49
34	Schematic of Motor Used in Holographic Investigation	50
35	Photograph of Reconstructed Hologram of USAF Resolution Target Located Within Motor Cavity, Collimated Light Illumination	52
36	Photograph of Reconstructed Hologram of Propellant Burned at 280 psi	52
37	Hologram Reconstruction (Ref 19)	55
38	Ideal Histogram	55

LIST OF FIGURES (CONTINUED)

<u>Figure</u>	<u>Caption</u>	<u>Page</u>
39	Histogram Shown on Overlap of Gray Levels	58
40	Calibration Array Circle Sizes (in μm) and Relative Positions	58
41	Effects of Filtering on Processed Images:	
	(a) Averaged and Threshold Applied (no speckle reduction filter),	60
	(b) Averaged, Speckle-Reduction Filtered, and Threshold Applied	60
42	Histograms of (a) Manufacturer's Data, and (b) Manufacturer's Data with Resolution Threshold Shown . . .	62
43	Histograms of (a) Truncated Manufacturer's Data, and (b) Measured Data Truncated by Resolution Threshold . . .	63
44	Histograms of (a) Manufacturer's Data with a 20 μm Size Threshold, and (b) Experimental Data from a Hologram Reconstruction	64
45	(a) Sample Image without Speckle	66
	(b) Same Image with Speckle Noise	66
46	Speckle Index as a Function of Sample Size	67
47	(a) Unfiltered Image of the Air Force Resolution Bar Target (S.I. = 0.30549)	70
	(b) Same Image with the Sigma Filter (2 Iterations, S.I. 0.10278)	70
48	(a) Histogram of the Unfiltered Image	71
	(b) Histogram of the Sigma Filtered Image	71
49	(a) Unfiltered Image Threshold at 140	72
	(b) Sigma Filtered Image Threshold at 140	72
50	(a) Image Filtered with the Local Statistics Filter (2 Iterations, S.I. = 0.11484)	74
	(b) The Local Statistics Filtered Image Thresholded at 140	74

LIST OF FIGURES (CONCLUDED)

<u>Figure</u>	<u>Caption</u>	<u>Page</u>
51	(a) Image Filtered with the Geometric Filter (3 Iterations, S.I. = 0.12918)	77
	(b) Geometric Filtered Image Thresholded at 140	77
52	Speckle Reduction Comparison	78
53	Resolution Degradation of Images	78
54	(a) Histogram of Local Statistics Filtered Image	81
	(b) Histogram of Geometric Filtered Image	81

LIST OF TABLES

<u>TABLES</u>	<u>TITLE</u>	<u>PAGE</u>
1	Calibration Results for Light Scattering Apparatus	12
2	Effect of Transmittance on Measured Particle Size	15
3	Test Conditions for First Test Series	28
4	Conditions for Second Test Series	30
5	Summary of Experimental Results for Second Test Series	30
6	Summary of 25 Micron Glass Beads Firings	39
7	Summary of Light Scattering Data for Aluminum Oxide Firings	42
8	Summary of SEM Data for Aluminum Oxide Firings	42
9	Calculated Residence Times for Particles Injected Into Motor	44
10	Time Per Iteration (512 x 512 Image, PC/AT)	51

INTRODUCTION

Aluminum is added to solid propellants to increase performance and to suppress high frequency combustion instabilities. A small amount of a variety of additives in addition to aluminum (aluminum oxide, zirconium, etc.) are also used in reduced-smoke propellants for acoustic stabilization. In addition, there is renewed interest in dense additives (Bi_2O_3 , etc.) in order to provide higher performance with low hazards propellants. Although the delivered specific impulse of metallized propellants is higher than that of the base propellants, the specific impulse efficiency is generally lower. This results from the presence of condensed metal oxides in the nozzle flow and from unburned metal within the motor port. Some particles, upon reaching the burning surface, depart immediately while others agglomerate on the surface before passing into the gas flow. Most of the metal combustion is thought to occur in the gas phase, resulting in small (typically less than two microns) metallic oxide particles. These particles are of major significance in determining the exhaust signature. In addition, particle burnout can also result in the break-up of a metallic oxide cap or layer. This can result in larger (greater than five microns) particles. The larger particles are more important in the determination of two-phase flow losses in the exhaust nozzle flow since they can lag the gas flow and, in principle, could be affected through propellant changes. There are several rather complex computer codes [Ref. 1] which attempt to model the important processes of momentum and thermal energy exchange between the solid, liquid, and gaseous phases as well as particle collisions, break-up, and wall collisions. However, these models remain semi-empirical and are generally based upon particle size distributions which were obtained from collected nozzle exhaust flows [Ref. 2]. Particle histories from the surface of the propellant to the nozzle exit remain largely unknown, due to the difficulty of making direct measurements within the motor and nozzle. Prediction of performance losses due to the presence of the original metal and the metal oxides are very sensitive to the assumed particle size distribution, and essentially no data are available that give this distribution as a function of position throughout the motor and nozzle.

Collecting exhaust products has been feasible only for small rocket motors. Even then, the techniques employed result in considerable variation in the measured sizes [Ref. 2]. Dobbins [Ref. 3] and Dobbins and Strand [Ref. 4] attempted to use an optical technique for measuring exhaust particle size and to compare the measurements with tank collected exhaust results. The optical technique used was a three-wavelength transmission measurement. This technique requires knowledge of particle index of refraction and the standard deviation of the particle size distribution. The optical measurements generally yielded sizes which were too small and the results were inconsistent with the collected exhaust data. It was speculated that this discrepancy resulted from a bi-modal exhaust particle distribution.

Light transmission measurements have the advantage of being applicable to dense concentrations where multiple scattering occurs [Ref. 5]. However, the method works best for small particles (on the order of the wavelength of the illumination source) and requires a-priori knowledge of the particle characteristics.

Light scattering measurements can also be used to determine particle size [Refs. 6-15]. If the scattering angles used are specifically selected, the

technique can be used to look almost entirely at one lobe of a bi-modal size distribution. Ratioing intensities obtained at two forward scattering angles can be used to further reduce the complexity of the method. However, scattering techniques are generally thought to be applicable only to systems where the transmittance is greater than approximately 90% in order to satisfy single scattering requirements.

A combination of light transmission and light scattering measurements [Ref. 13] appears to be well-suited for many solid propellant rocket motor exhaust flows. However, experimental efforts are first needed to determine under what conditions (metal loadings, operating pressures, propellant ingredients, etc.) light scattering measurements can be made in this difficult environment.

The goal of the investigation to date has been to develop and compare experimental techniques that can be used for obtaining quantitative data on the effects of propellant properties, operating pressure, and nozzle geometry on the behaviour of metallized particulates within the grain port and nozzle of solid propellant rocket motors. These data are needed in order to (1) improve solid propellant performance predictive capabilities, (2) provide needed input to current steady-state combustion models which include oxidizer-metal interactions, (3) provide data on the effects of motor and propellant conditions on exhaust signature and (4) provide in-motor particle size distributions which will allow more accurate predictions of damping in stability analyses. The techniques employed have been high speed motion pictures of strand burners and slab burners in a cross-flow environment, SEM analysis of post-fire residue (strand, slab, and motor), determination of changes in D_{32} across the exhaust nozzle using measurements of scattered laser light, and holograms of burning propellant in strands, slabs, and motors. In addition, considerable effort has been directed toward development of automatic data retrieval methods for obtaining particle size distributions from holograms taken of the combustion of solid propellants. The holographic effort is a two-part problem. Techniques must be developed for obtaining good quality holograms in a realistic solid propellant combustion environment. However, these holograms are of limited value unless the particle size data can be obtained from them in a reasonable time period. This requires development of computer-aided image analysis techniques.

In previous efforts [Ref. 16 & 17] the motion picture and holographic techniques were successfully demonstrated using propellant strands with up to 15% aluminum. Fourteen micron resolution was obtained in the high speed motion pictures with a 1.12X (and very small depth of field). In addition, initial determinations of D_{32} were made using measurements of scattered laser light at the exhaust of a small rocket motor. Apparatus modifications were then made to expand and improve the obtainable data. Some of the results presented herein have been previously reported [Ref. 18, 19].

DETERMINATION OF PARTICULATE SIZE USING MEASUREMENTS OF SCATTERED LIGHT

The method used in the present effort is the diffractively scattered light technique. The diffraction patterns of light scattered by particles are analyzed to determine the volume-to-surface mean diameter (D_{32}). This method

has the disadvantages that size distributions cannot be easily determined and particles larger than some threshold size will not be detected due to the exceedingly small angles at which they scatter light. However, it has the advantage that it is non-intrusive and, in theory, can be used in the internal motor environment. Propellant composition can limit the application of the technique by producing large particulates and/or very dense particle clouds.

The completely general theory of scattering was developed by Mie and is presented by Van de Hulst [Ref.15]. The light scattering characteristics for spherical particles of any size are fully described and the phenomena of reflection, refraction, diffraction and absorption are considered. For particle sizes much smaller than the wavelength of the illuminating light source, the Mie equations simplify to what is called Rayleigh scattering.

The size of the particles of interest in solid propellant rocket motor combustion depends upon the application. Most applications are concerned with particles having diameters much greater than the wavelength of visible light. Scattering by these larger particles is described by Fraunhofer diffraction. Measuring the particle size for a monodispersion can be accomplished by measuring the angular position of a dark or bright ring in the diffraction pattern. This method is not used for polydispersions since the discrete rings are not observed. However, Dobbins, et al [Ref.7] found that the volume-to-surface mean diameter of a polydispersion (D_{32}) defined by

$$D_{32} = \frac{\int_0^{D_{\max}} N_r(D) D^3 dD}{\int_0^{D_{\max}} N_r(D) D^2 dD} \quad (1)$$

(where $N_r(D)$ is a distribution function describing the proportion of particles with diameter D in the sample), could be accurately measured. The value of D_{32} was shown to be quite insensitive to the form of $N_r(D)$. In addition, since the ratio of forward scattered light at two angles is dominated by Fraunhofer diffraction, it is insensitive to the particle refractive index and the particle concentration [Ref.13]. To evaluate the integrated intensity over particle sizes requires specification of $N_r(D)$. Dobbins, et. al. [Ref.7] used the Upper-Limit-Distribution-Function developed by Mugele and Evans [Ref.9] and this approach was followed in the present investigation.

For $\pi D_{32} \theta / \lambda$ (where θ is the scattering angle and λ is the wavelength) less than 3.0, a Gaussian curve [Ref.14] can be used, which closely matches the theoretical intensity profile obtained by integrating the Fraunhofer diffraction expression together with the Upper-Limit-Distribution-Function [Ref.7]. This Gaussian expression has been presented by Buchele [Ref.14] and is given by

$$I_{\theta}/I_{\theta=0} = \exp - (0.57 \pi D_{32} \theta / \lambda)^2 \quad (2)$$

Equation (2) can be used to obtain the intensity ratio between two (within the apparatus limits) forward scattering angles:

$$I_2/I_1 = \exp - D_{32}^2 [(\theta_2^2 - \theta_1^2) (0.57\pi/\lambda)^2] \quad (3)$$

EXPERIMENTAL APPARATUS AND PROCEDURES

Motor Components

Figure 1 is a schematic of the small motor which was used. Figure 2 shows the motor mounted on the test stand and Figure 3 shows the motor components. Initial measurements were made in the same motor, but with only one inch between the propellant grain and the nozzle entrance (vs. nine inches in the present design). In solid propellant motors agglomerate size may depend on many factors, such as the propellant type, original particle size, chamber pressure, burning rate, aluminum concentration and motor geometry. Short residence times can lead to poor combustion efficiency. The short motor residence time was less than 3 milliseconds. For good combustion efficiency (the conversion of all aluminium to aluminium oxide), typical minimum residence times are between 10 and 15 milliseconds. It was apparent from examination of the exhaust nozzle after a firing that large agglomerates of aluminium/aluminium oxide were impinging on the converging surface of the exhaust nozzle. This also resulted in large particles exhausting through the nozzle exit. D_{32} from the exhaust measurements was approximately 50 microns. SEM photographs of collected exhaust also indicated particles ranging from one micron up to 60 microns. It was therefore decided to lengthen the motor to increase the residence time to between 10 and 15 milliseconds without adding additional propellant. This required an eight inch extension onto the initial two-inch length. Most tests were conducted with this configuration.

After the initial test series it was decided to modify the motor to permit measurements of particle sizes from "known" initial particle sizes in the gas phase. This was accomplished by mounting the motor vertically and introducing particles at the head-end of a non-metallized propellant port.

In order to properly test the proposed method of introducing particles into an ignited motor, a scaled-down Plexiglas model of the rocket motor was manufactured. Nitrogen was used to pressurize the model and was passed through a small (one-half inch inside diameter) gasoline filter in an attempt to simulate hot gases rising from a burning propellant surface. Once the model chamber pressure had been set, a single ported spoon could be aligned to allow aluminum oxide particles from a hopper to fall (via gravity) through the feeding tube and into the rocket body. High speed movies taken just aft of the gasoline filter verified that the injection method resulted in a uniform distribution of falling particles. Holograms of the particles in cold flow in the motor also showed a uniform distribution. Spherical particles were required in order to have them pass freely and individually into the motor cavity. It was also found that the particles would often agglomerate at the exit of the

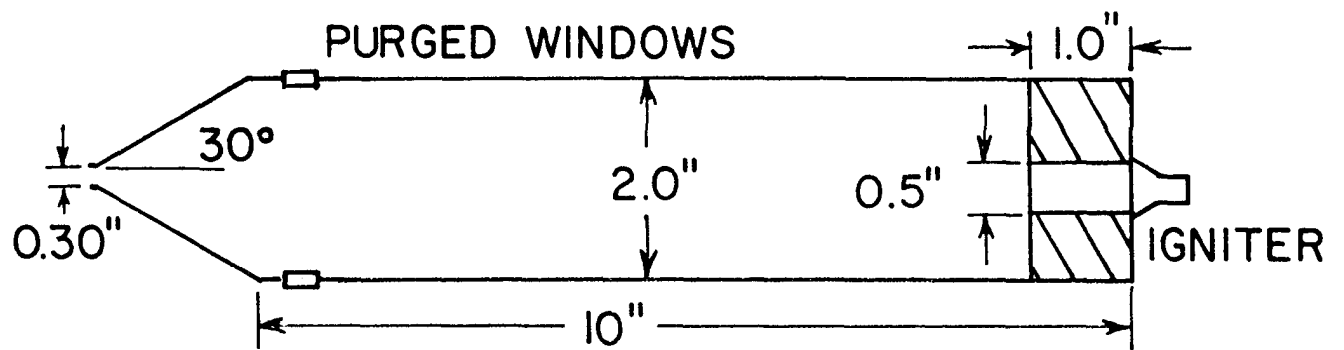


Figure 1. Dimensions of Small Solid Propellant Rocket Motor

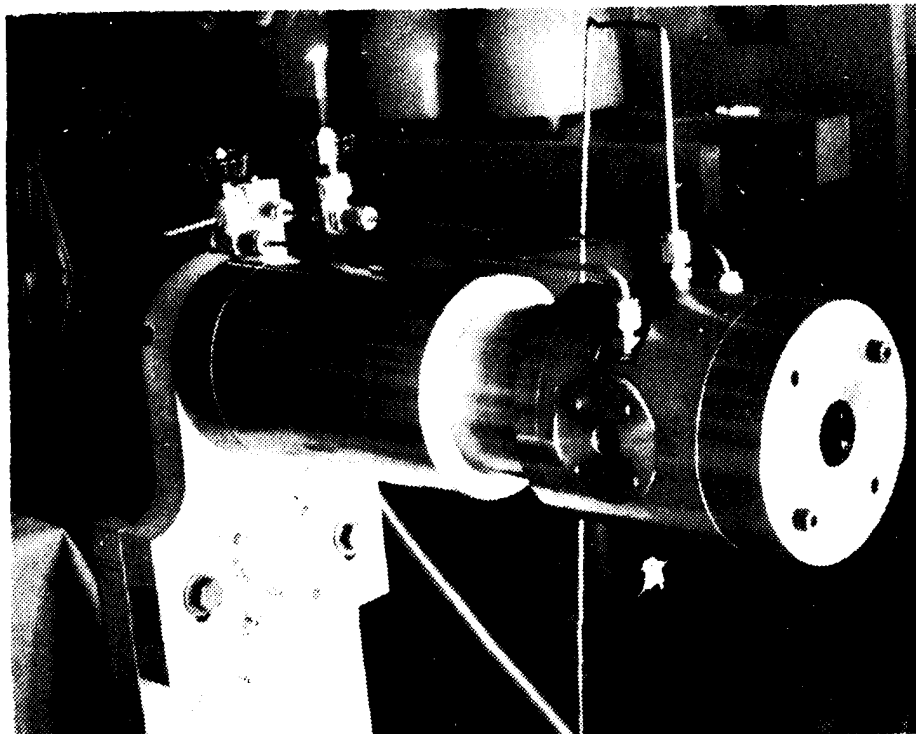


Figure 2. Long Motor on Test Stand

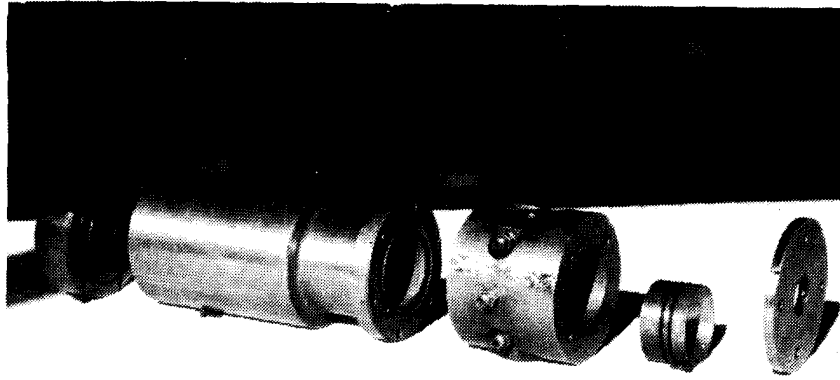


Figure 3. Motor Components

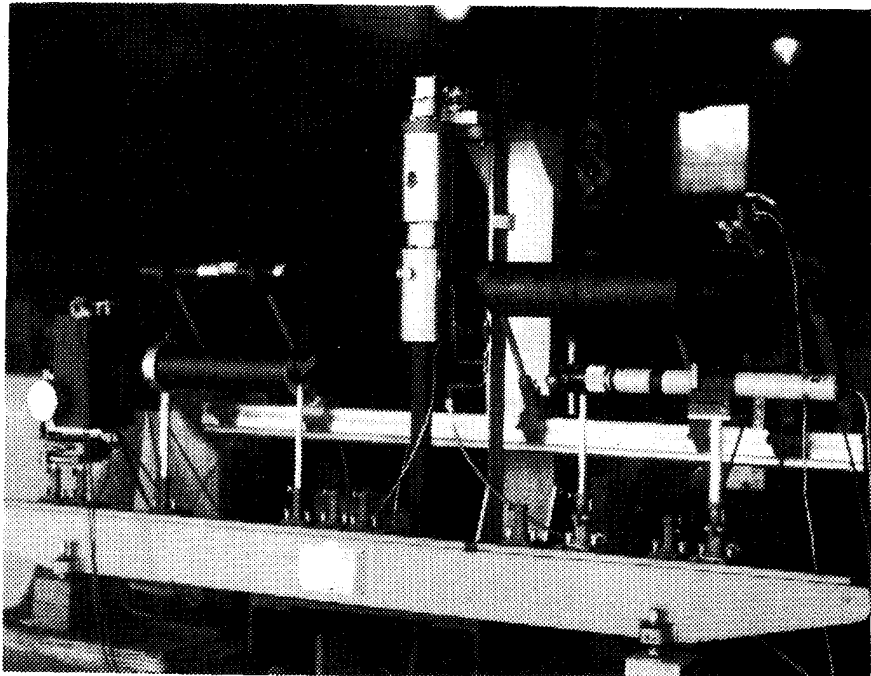


Figure 4. Experimental Apparatus, Vertical Motor Mounting

injection tube due to moisture (apparently from condensing combustion products). This problem was eliminated through the use of a very small mass flow of dry nitrogen into the particle feeder. The motor is shown mounted vertically in Figure 4. A photograph of the particle injector is shown in Figure 5. Schematics of the modified motor and the particle feeder are shown in Figures 6 and 7, respectively.

Light Scattering Measurement Apparatus

Figure 8 is a schematic of the light scattering measurement apparatus.

The light scattering equipment was mounted on two optical benches: one for measurements in the nozzle exhaust and one for measurements within the motor cavity. The light sources employed were eight milliwatt helium neon lasers. Figures 9 and 4 show the apparatus mounted with the motor in the horizontal and vertical positions, respectively.

Each beam passed through the appropriate test volume and was then intercepted by a physical stop located in front of the receiving optics. The further the stop was placed from the test section, the smaller was the angle at which scattered light could be measured. The upper limit of the scattering angle is determined by the diameter and focal length of the focusing lens, the distance between the focusing lens and the particles, the diameter of the motor window, and the height/position of the diode array. In the present apparatus scattered light could be measured within an angle increment of approximately 0.05 radians. The minimum possible scattering angle was approximately 0.008 radians and the maximum approximately 0.07. These angles can be changed by changing one of the above limits. The presently employed angle limits introduce some bias in the collected data.

The scattered light passed through a wide-pass laser line filter and a 50 cm focal length lens which focused the light onto the linear diode array. The arrays each contained 1024 silicon photodiodes on a single chip with 25 micron spacing. The accompanying circuits provided a "sampled and held" output which was essentially analog except for switching transients. The actual sampling time of the array was about 34 msec with a delay between scans of about 6 msec. Currently the system is being improved to permit sampling in approximately 4 msec.

Raw data was plotted on the CRT where any obviously erroneous scans could be excluded from further data reduction. The valid scans were averaged to obtain a mean scattering profile. The mean intensity profile taken before particles were introduced was then subtracted from that taken with particles present. This corrected for the characteristics of individual photodiodes and extraneous light which was independent of the particles.

A symmetric moving-average-type of digital filter was then applied to the profile to achieve smoothing. This type of digital filter was chosen for simplicity and because it does not have the phase lag of analog filters. Smoothing of the data was found to be necessary if good results were to be obtained using the two-angle methods when only a few scans of the array are possible (as in time-dependent combustion).

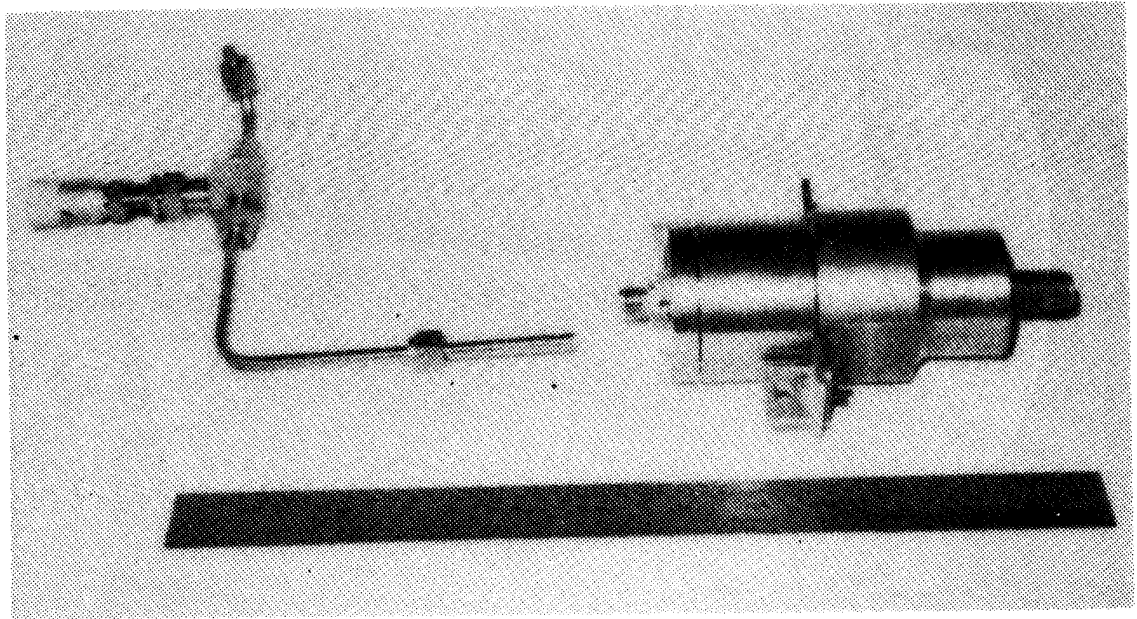


Figure 5. Particle Feed Apparatus

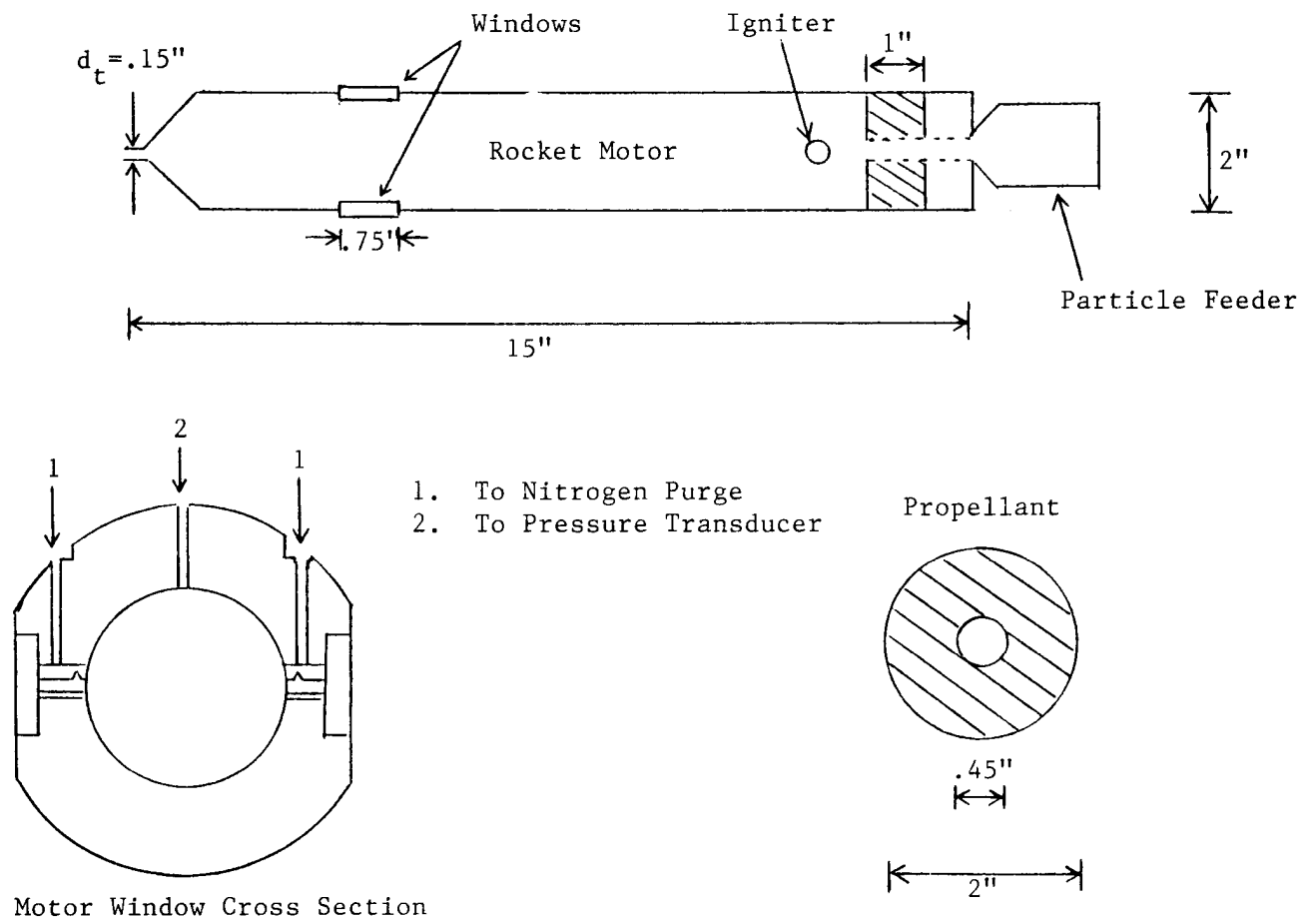


Figure 6. Schematic of Small Motor

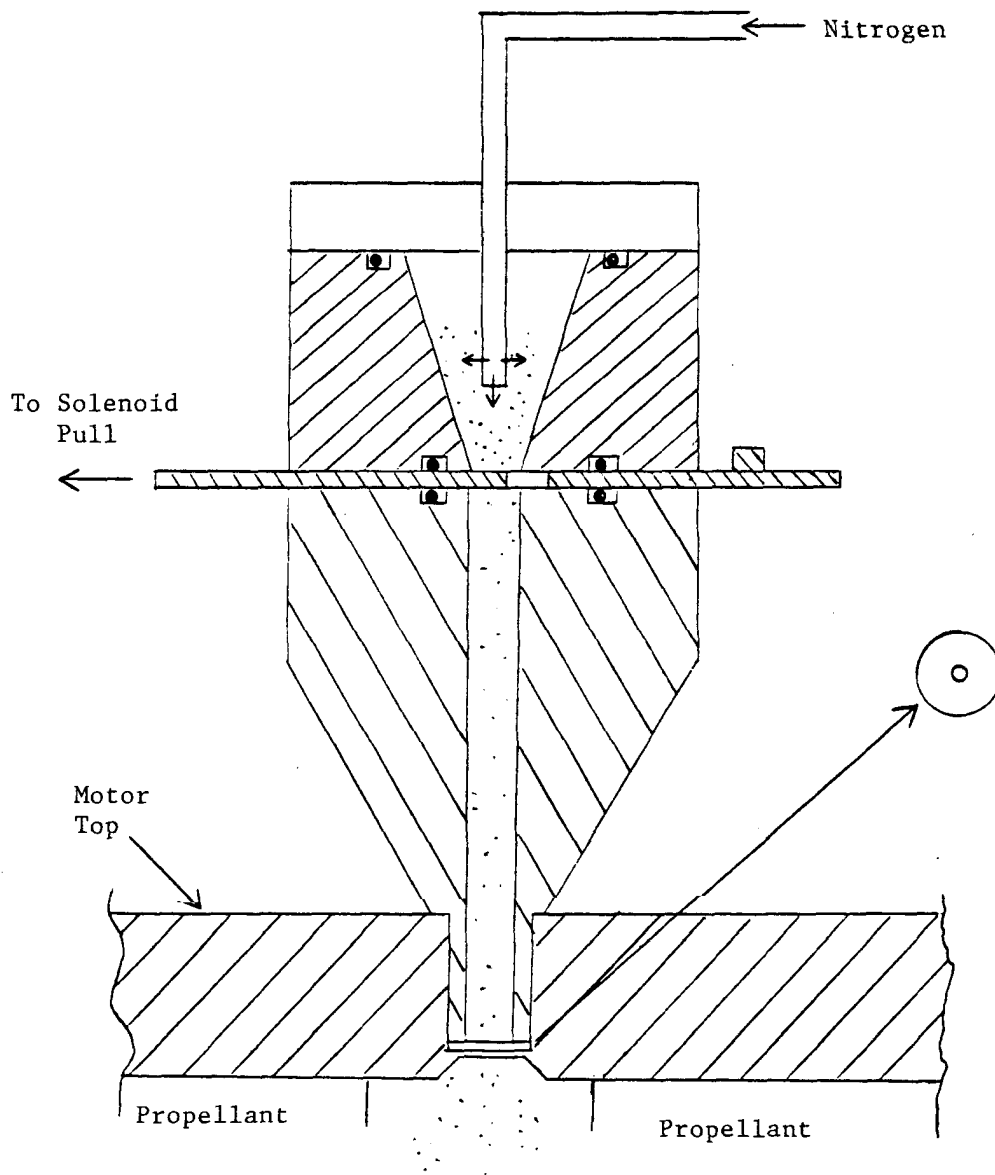


Figure 7. Schematic of Particle Feed Apparatus

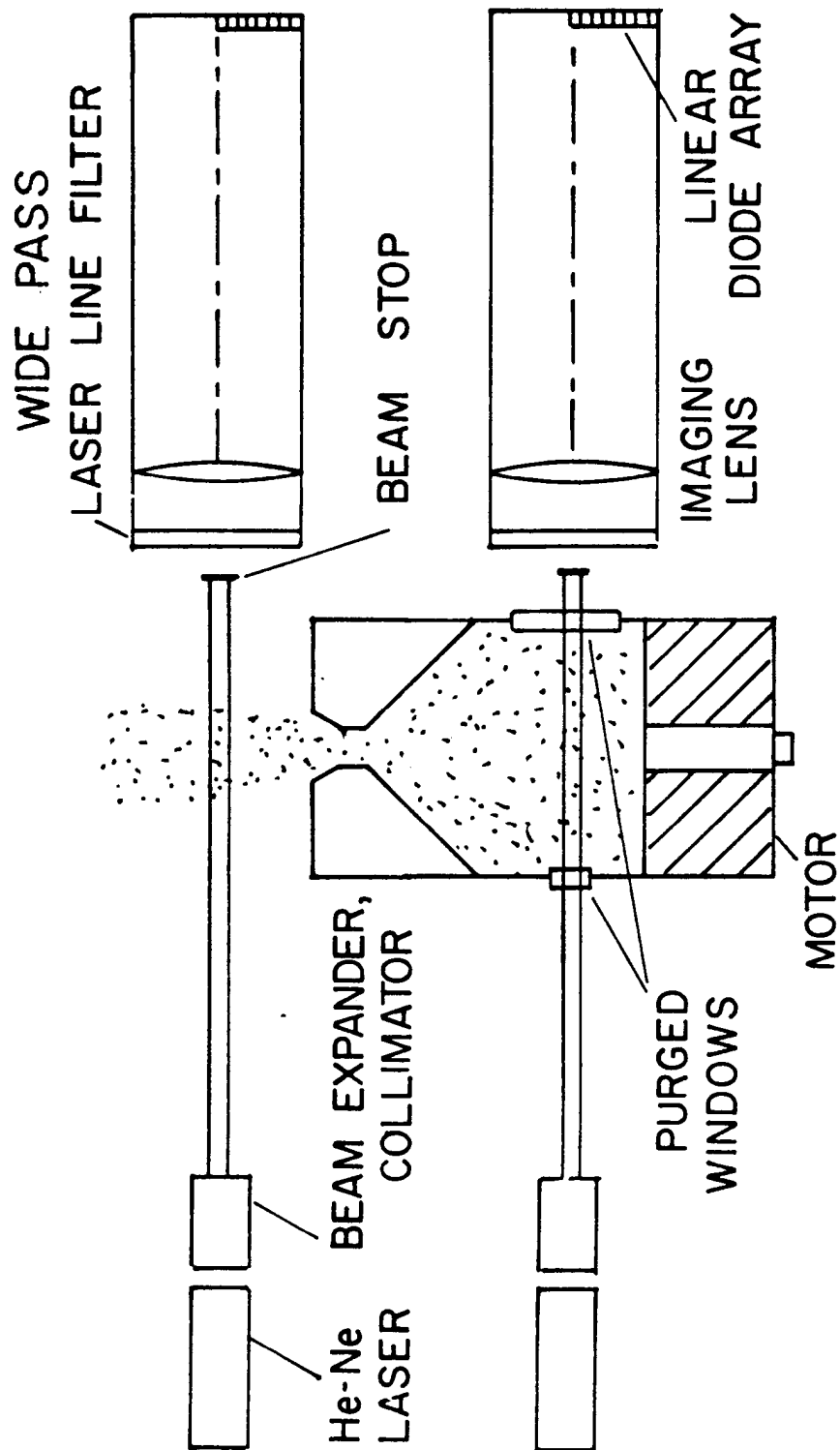


Figure 8. Schematic of Scattered Light Measurement Apparatus

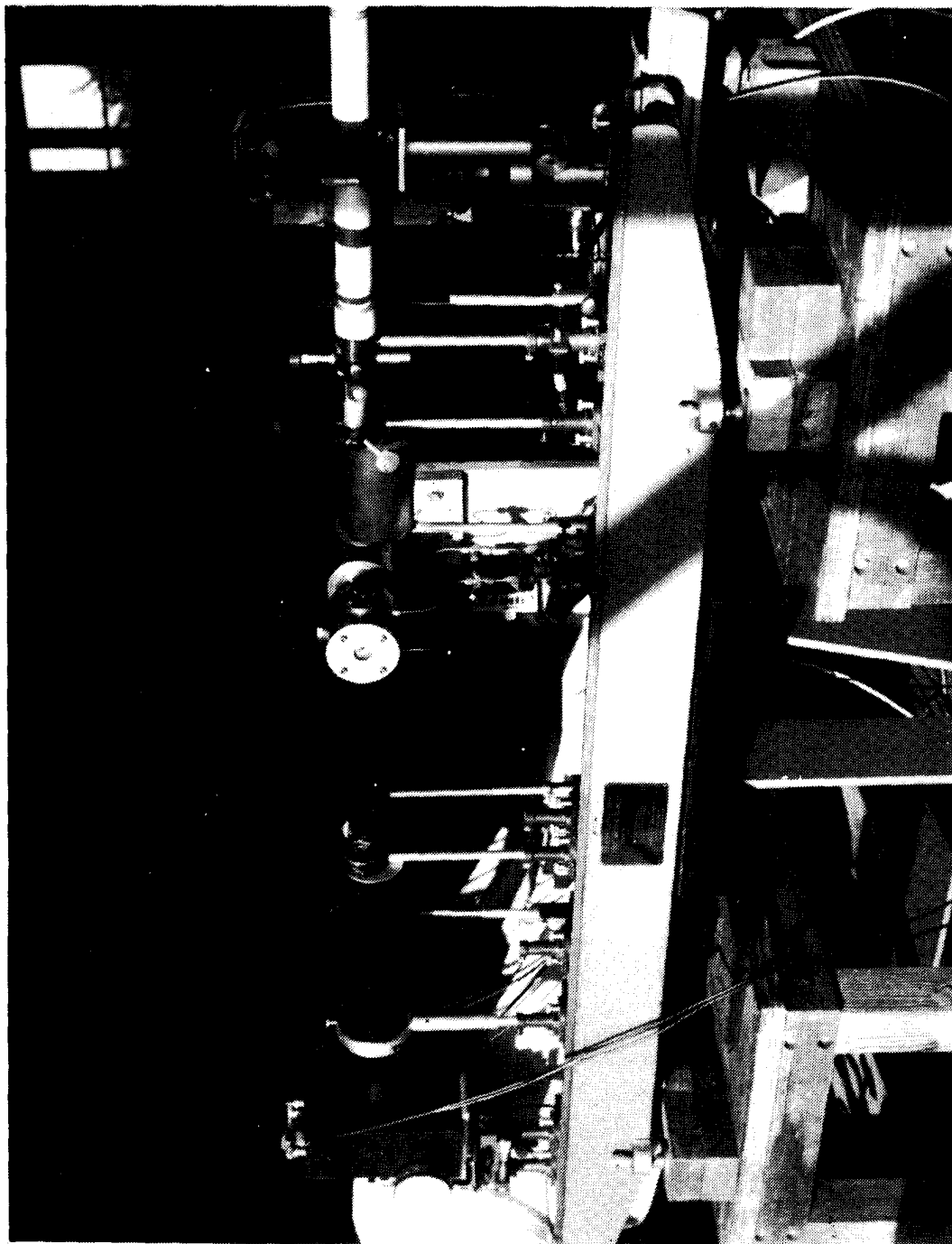


Figure 9. Experimental Apparatus, Horizontal Motor Mounting

Several data reduction techniques were investigated for obtaining D_{32} from the measured intensity profiles. The initial method required the comparison of the experimentally obtained intensity profile with that produced using equation (2). This required the profile to be normalized using the "unknown" (since the transmitted light dominates at small angles) forward scattered intensity at $\theta = 0$. This quantity and D_{32} for the theoretical profile were adjusted using interactive graphics until the theoretical and experimental profiles provided the best match. This technique provided reasonably good results, but required considerable user interpretation of the "best fit" and the scattered light intensity at $\theta = 0$.

The method currently being used minimizes both data reduction time and "user interpretation." A minimum value of θ is chosen from the filtered profile (where beam stop effects or diode position begin to influence the data). This yields I_1 and θ_1 for use in equation (3). D_{32} is then varied, each value resulting in a curve for I_2 vs. θ_2 . The "best fit" to the experimental profile is then found, without the need to estimate the $\theta = 0$ scattering intensity.

SYSTEM CALIBRATIONS

Calibration of the apparatus was accomplished by measuring D_{32} of various particles of known size distribution. Polydispersions of glass or polystyrene spheres and aluminum oxide powder were suspended in water within a Plexiglas or glass container. A scanning electron microscope (SEM) was also used to photograph each particle sample.

Figures 10 and 11 show typical results obtained in the calibration tests. Table 1 presents some of the calibration results.

TABLE 1. CALIBRATION RESULTS FOR LIGHT SCATTERING APPARATUS			
Particle Material	Sample Particle Size Range (microns)	Calculated D_{32} (microns)	Measured D_{32} (microns)
Polystyrene	3-6	4.7**	4.5
Polystyrene	6-16	10.2**	10.0
Polystyrene	15-30	21.6**	21.0
Glass	37-44	38.0*	40.0
Glass	53-63	54.0*	54-58
Glass	1-37	25.0*	28-30
*From SEM Photographs		**From Manufacturers' Data	

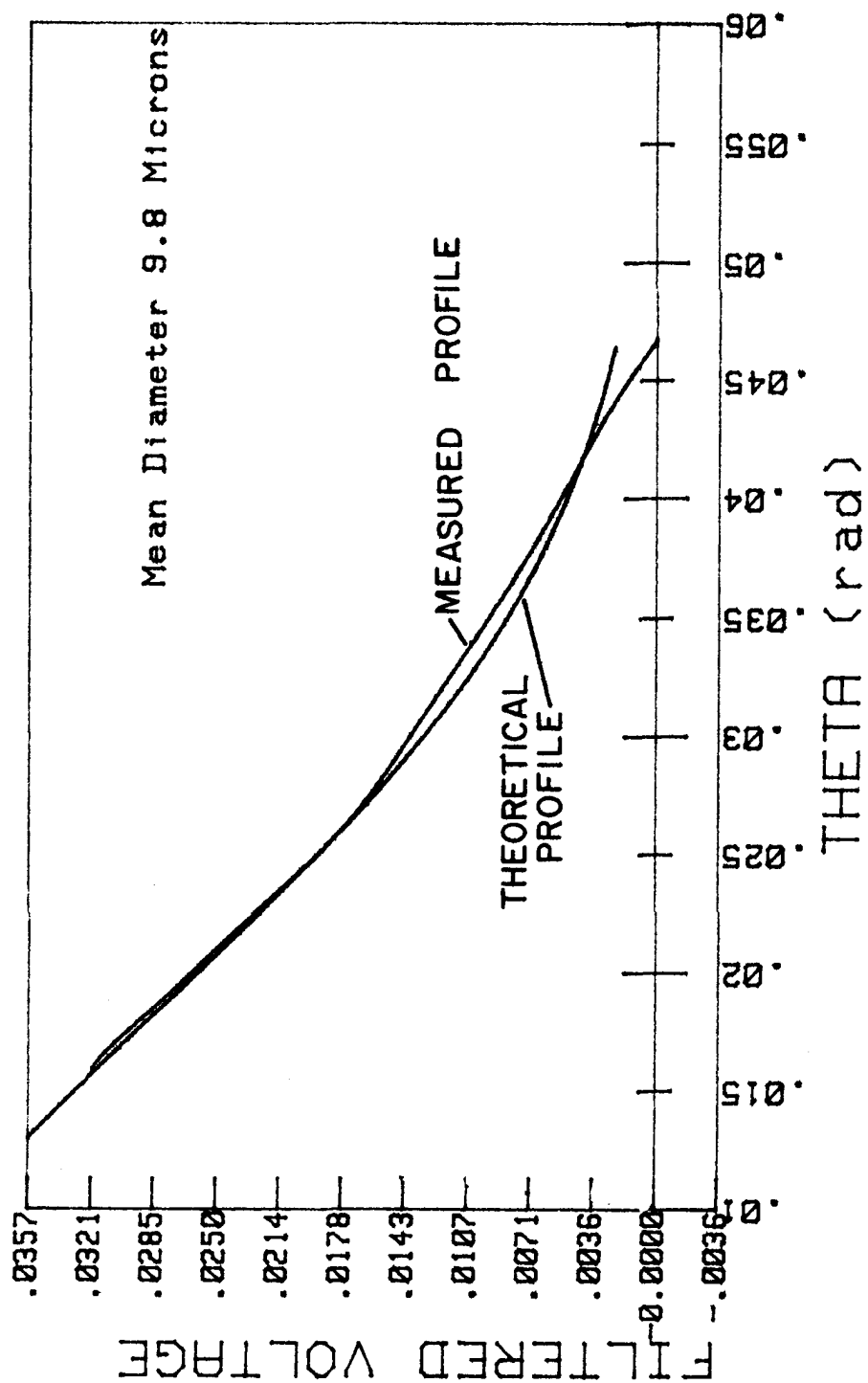


Figure 10. Calibration Profile, 85% Transmitted Light

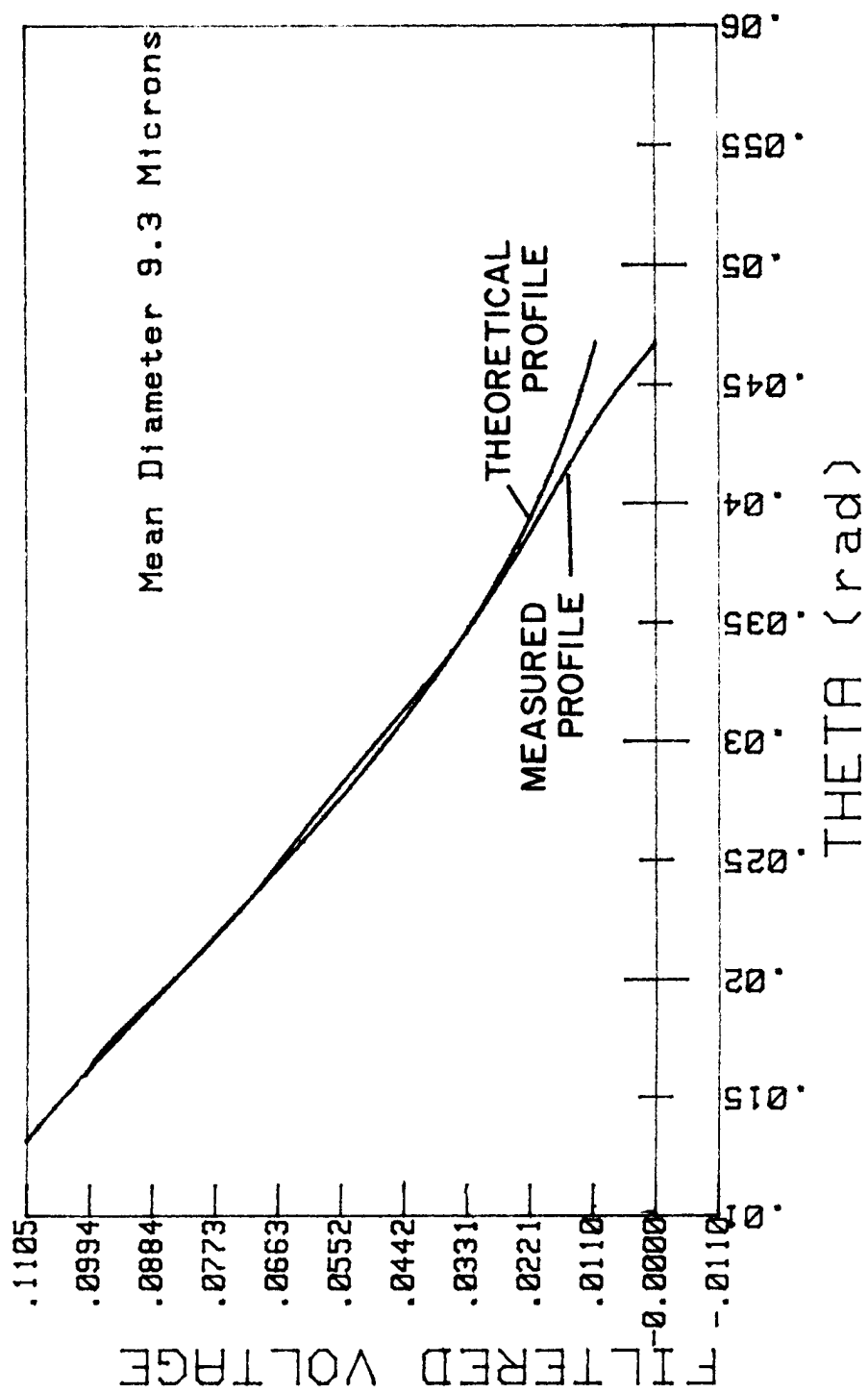


Figure 11. Calibration Profile, 30% Transmitted Light

An initial point of concern was the narrow range of measuring angles which was employed in the present apparatus. Since large particles diffract most of the incident light at small angles and very small particles diffract most of the incident light at large angles, the range and minimum angle employed could have resulted in insufficient sensitivity to particle size for the expected range of particle sizes. Figure 12 shows three theoretical profiles for D_{32} values of 8.3, 9.3, and 10 microns. It was apparent from the sensitivity of the slope change with D_{32} that the mean particle size could be determined with an uncertainty less than ± 0.5 microns.

Transmittance effects were also investigated in conjunction with the calibration. Transmittances above 90% are generally specified to meet single scattering requirements. Calibrations were conducted using polystyrene spheres with a D_{32} of 10.2 microns. Scattering data were recorded for transmittances of 85%, 70%, 60%, 50%, and 30%. The results are presented in Table 2. Even a transmittance of 30% did not severely affect the measurement. These results indicate that particle sizing methods based upon single scattering theory can be effectively used in a multiple scattering environment with transmittances significantly less than 90%.

<p style="text-align: center;">TABLE 2</p> <p style="text-align: center;">EFFECT OF TRANSMITTANCE ON MEASURED PARTICLE SIZE</p> <p style="text-align: center;">(D_{32} from Manufacturers' Data = 10.2 Microns)</p>	
Transmittance (%)	Measured D_{32} (microns)
85	9.8
70	9.6
60	9.5
50	9.4
30	9.3

Calibrations were also conducted within the motor cavity with the laser beam and scattered light passing through the motor windows. The results were essentially identical to the results obtained without the windows in the optical path.

If the larger sizes in a bi-modal distribution of actual motor products includes a wide range of particle sizes, then care must be taken in the selection of the forward scattering angles so as to not bias the measurements to the larger or smaller particle sizes. Another concern about the measurement technique was the effect of the index of refraction of the exhaust gases in which the particles are present. To examine this, the 6-16 micron polystyrene

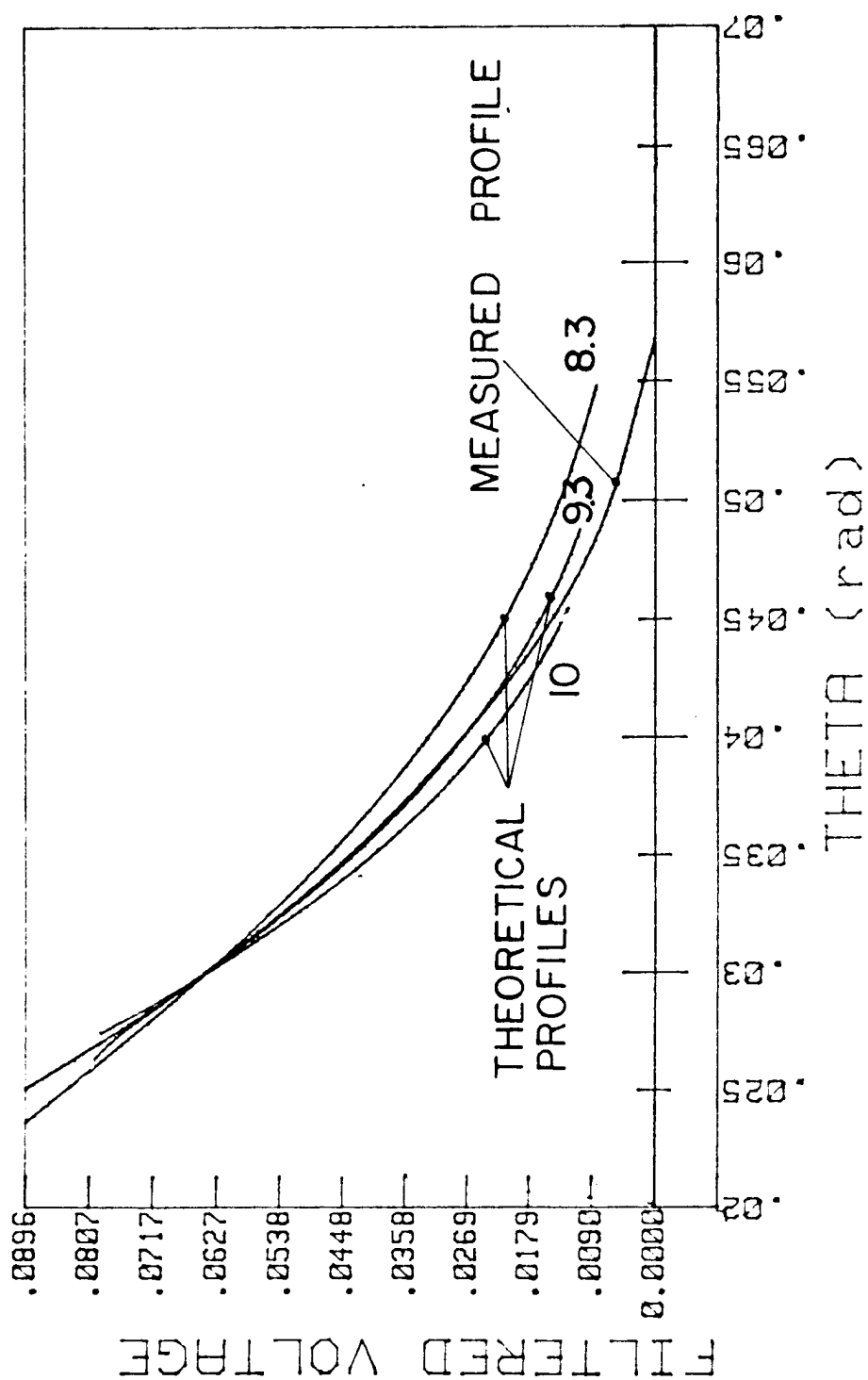


Figure 12. Calibration Profiles, Slope Sensitivity to Particle Size

sphere data was used to find D_{32} with varying assumed values for the index of refraction. The result was that a 10% increase in the index of refraction increases the "measured" D_{32} by approximately 10%. This could present difficulties if the present technique were attempted to be applied to a wide range of propellants/operating conditions where the unknown exhaust index of refraction could vary significantly from test-to-test. In the present effort similar propellant compositions are used with varying solids size and loading and with varying nozzle geometries. Variations in the index of refraction should be small in this case.

Another informative point in apparatus design is given by Hirleman [Ref. 20] in regards to placement of the focusing lens (or in sizing the motor windows). Hirleman notes that truncation of the larger scattering angles, which is a function of the placement of focusing lens, will cause a biasing against the small particles. Eighty-four percent of the diffracted energy from a particle of diameter d is contained in the center lobe, i.e., within the first minimum in the Airy diffraction pattern.

$$\theta_{\text{first minimum}} = \frac{3.83\lambda}{\pi d} \quad (4)$$

In the present apparatus, diffracted light at angle θ is refracted by the focusing lens to a point (ring) on its focal plane at a radial distance r from the optical centerline. The diode array is located at the lens focal plane. Thus

$$r = f\theta \quad (5)$$

where f is the focal length of the lens.

A focusing (i.e., transform) lens with diameter D (radius $D/2$) must be placed within distance Z from the particle to capture all light scattered at angle θ .

$$\theta = \frac{D/2}{Z} \quad (6)$$

If 84% ($\theta_{\text{first minimum}}$) of the diffracted light is selected as the maximum allowable truncation, then (4) into (6) yields

$$Z = \frac{\pi d D}{7.66\lambda} \quad (7)$$

In the present apparatus Z was 30.5 cm; in the exhaust beam, D was 5.08 cm. and λ was .6328 microns. This yields a d of approximately 9 microns. Particles smaller than 9 microns can be expected to have more than 16% of the diffracted energy lost to the measurement system. Of course, in any measurement apparatus the large amount of light scattered at very small forward angles cannot be detected due to superposition with the transmitted light. In addition, the present apparatus uses a linear diode array with a maximum length

of one inch. With the present transform lens, light could be detected only with a $\Delta\theta$ of approximately .05 radians (2.9°). As indicated above, this introduces some bias into the data as illustrated in Figure 13.

The curve fitting method discussed above was found to provide quite accurate results for particles as small as three microns. However, these calibrations were made using samples which have no particles significantly smaller than three microns. In the exhaust of solid propellant rocket motors it is known that many particles exist with sizes less than one micron. These small particles were not of interest in the present investigation, but it was necessary to determine if their presence would effect the measured value for D_{32} . Therefore, a bi-modal calibration test was conducted.

Two particle sizes, 5.1 microns and 0.8 microns, were used in the calibration. The scattering apparatus was set with the photodiode arrays lowered one centimeter below the optical centerline. This measured the scattering angles between approximately 1 and 4 degrees. The 5.0 micron particles were suspended in a solution of distilled water and the light scattering profiles in both beam paths were recorded. The D_{32} was measured to be 5.1 microns through the motor and 5.4 microns for the exhaust beam, in excellent agreement with the particle manufacturer's data. Following this, a solution of 0.8 micron particles was measured using the same procedures. The results showed no correlation and demonstrated the problem of trying to measure particles less than approximately 3 microns using the present optical components and positions. The 5.1 micron particles diffracted light such that approximately 46% of the scattered light in the forward lobe was measured by the system. The 0.8 micron particles diffracted light at larger angles, such that only approximately 9% of the light scattered in the forward lobe was measured by the system. This meant that the concentration of small particles had to be very high in order to develop enough scattered light to be measured.

The 5 micron particles were then mixed with the 0.8 micron particles in a ratio of roughly 1:25. In both beams, D_{32} came out to be essentially the D_{32} of the larger particles. The larger particles scattered much more measureable light and dominated the scattering profile, even though there were far fewer large particles in the mixture. Of course, D_{32} is also dominated by the larger particles in a distribution.

Another area of concern in the application of light scattering measurements to the rocket motor environment was the effect of soot, thermal gradients and shock waves on the transmitted (and scattered) light. It was expected that the light intensity would be decreased and some beam broadening would occur as the light beam traversed a hot gas flow without particles present. Several tests were conducted to examine this effect. Non-metallized propellants were burned and the laser beam was positioned on the diode array.

The first test was conducted in the exhaust jet and used a GAP/AP propellant. Although some diode saturation occurred before the motor firing (Figure 14), there was an approximately 55% attenuation of intensity and a small amount of beam broadening.

Attempts to conduct the same test through the motor cavity revealed another problem area. The laser beam was deflected off of the narrow width (25

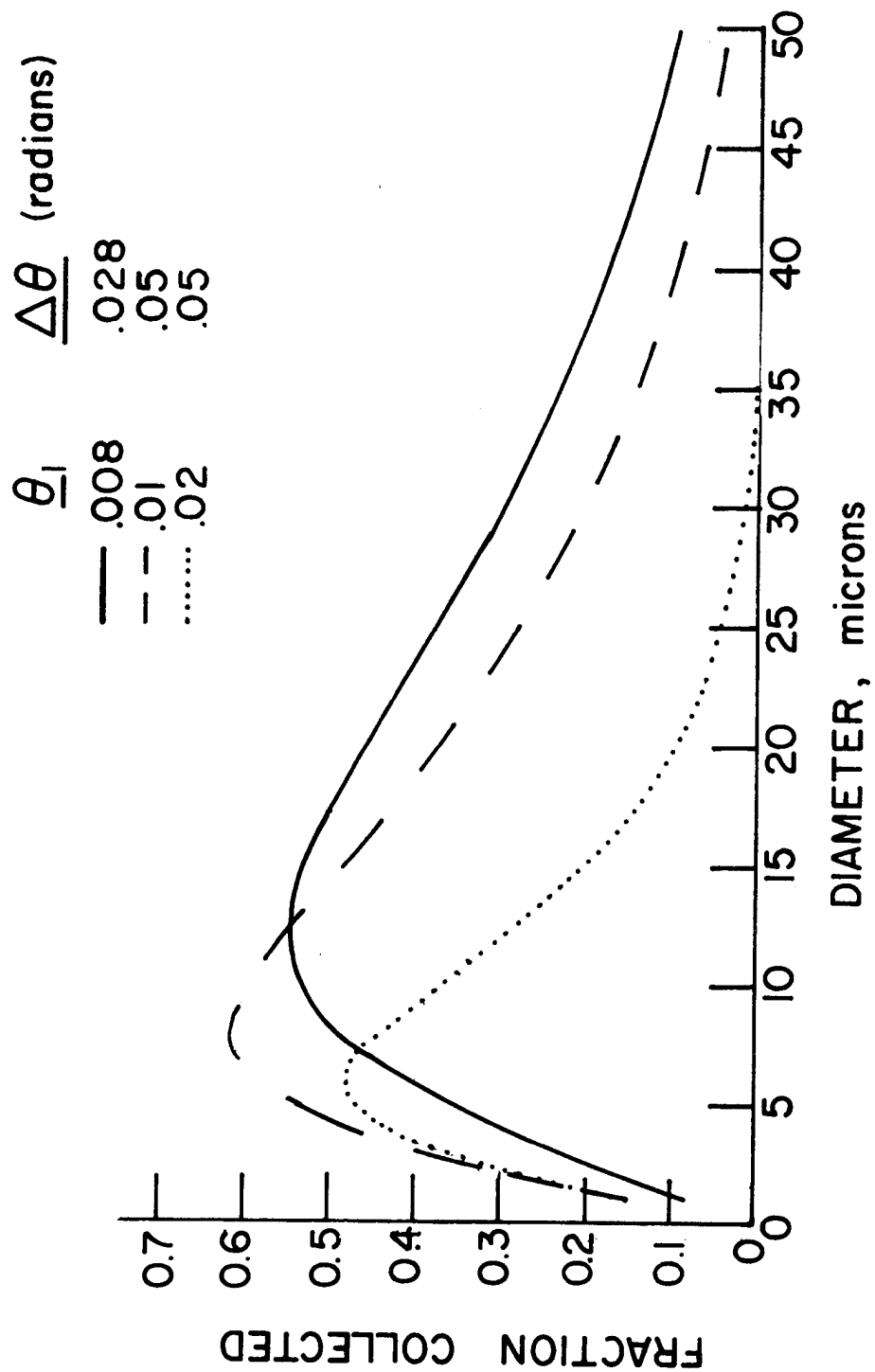


Figure 13. Fraction of Total Scattered Light Collected as Function of θ and θ .

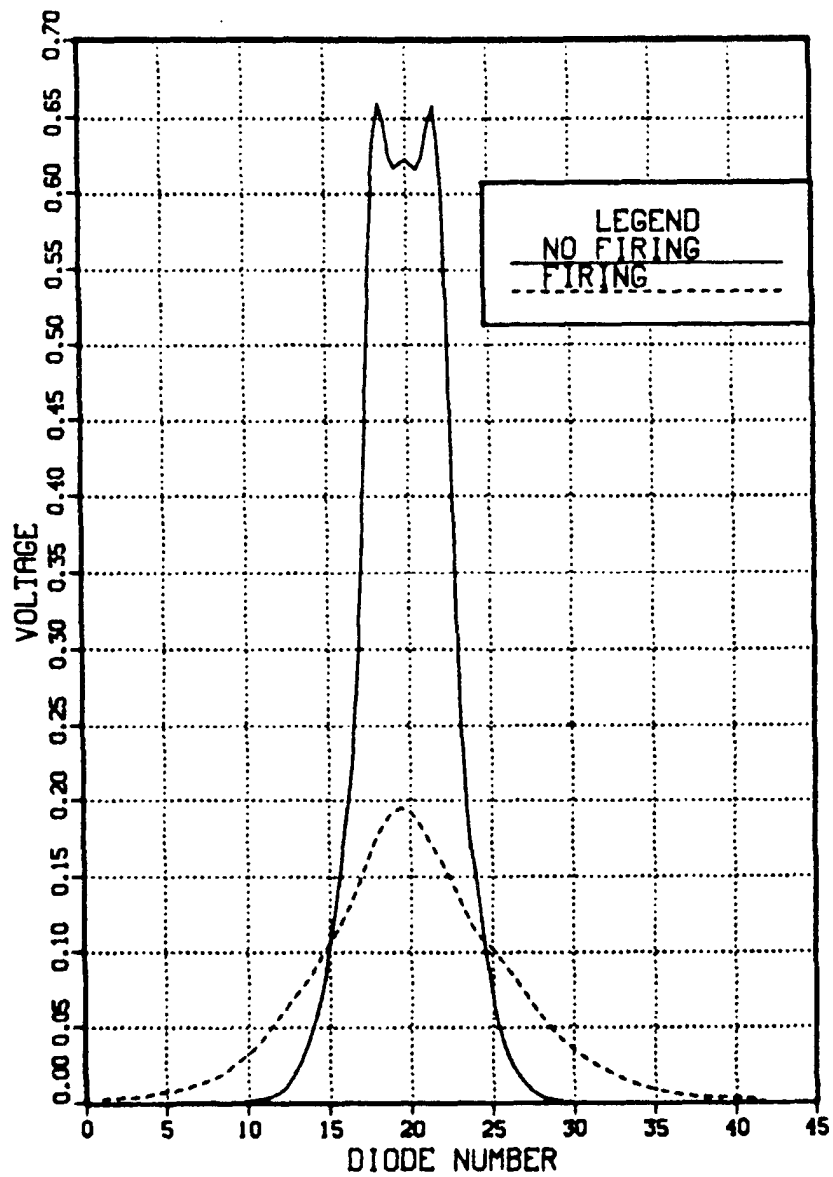


Figure 14. Effect of Exhaust on Transmitted
Light, Nonmetallized GAP/AP
Propellant

micron) diode array. This was verified by replacing the diode array with a large active area, single photodiode. Approximately 60% transmittance was observed in the latter test. A second test was conducted using a non-metallized HTPB/AP propellant. Figure 15 shows that some attenuation and beam spreading occurred. The motor beam deflection problem was again observed.

A third transmittance test was conducted in the exhaust jet using a GAP/AP propellant with 2% (20 microns) aluminum. Although some diode saturation occurred again, Figure 16 showed that the transmittance was high and beam spreading was again very slight.

It was also necessary to ensure that a non-metallized propellant did not produce "scattered" light to the diode array when it was located in its normal position (.02 radians minimum scattering angle). Figure 17 shows that no scattered light was received by the diode array.

A test was also conducted in which the lasers were turned off. No light was received by the diode arrays, indicating that no combustion light was generated near the .6328 micron wavelength.

The laser beam which passed through the motor windows presented some problems as discussed above. Careful alignment was required to prevent multiple reflections from the windows.

The motor laser system was carefully aligned. After alignment, motor firings were conducted using the non-metallized AP/HTPB propellant. These firings typically reached a peak pressure of 300 psi, with no steady-state chamber pressure. The data from the multiple (eight) sweeps of the diode array showed some "no voltage" traces (as expected when no particles are present) and others with diode saturation and a steep intensity profile at small angles.

A check was made of the propellant to see if there might be particulate matter in the propellant which could result in this behaviour. Scanning electron microscope photographs were taken, but the results were inconclusive. A small number of 20 micron particles were found. Their composition was unknown, but it seemed unlikely that the small number of 20 micron particles found could be responsible for the observed data.

The vibration sensitivity of the measurement system was then suspected. The various components of the system were tapped and vibrated while watching the diode trace on an oscilloscope, but the trace remained relatively steady even under some heavy tapping.

Other possible sources for the motor laser beam problem were window movement under pressure, nitrogen purge (for the windows), and motor temperature gradient effects. Window movement was checked by capping the nozzle and pressurizing the motor to 250 psi. This had a negligible effect on the diode trace. The nitrogen purge for the windows had no effect on the trace when used without a motor firing. Density gradients created during a firing, however, could be a problem. Finally, a torch was placed in the motor to study temperature effects. The nitrogen purge was turned on and off to look at the effects of the interaction of the hot and cold gases. In all cases the temperature gradients caused only a minor fluctuation in the diode trace.

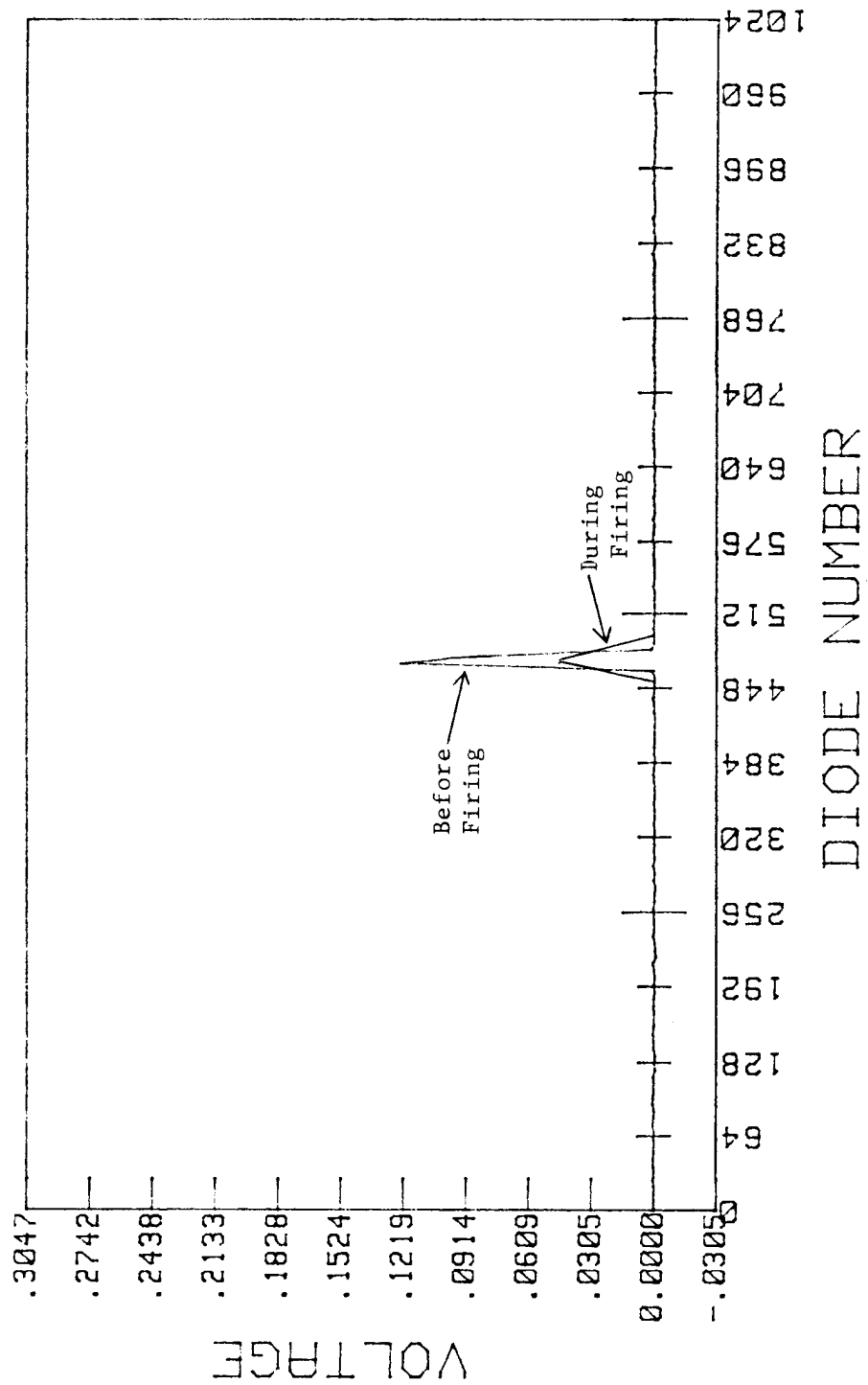


Figure 15. Effect of Exhaust on Transmitted Light, Nonmetallized HTPB/AP Propellant

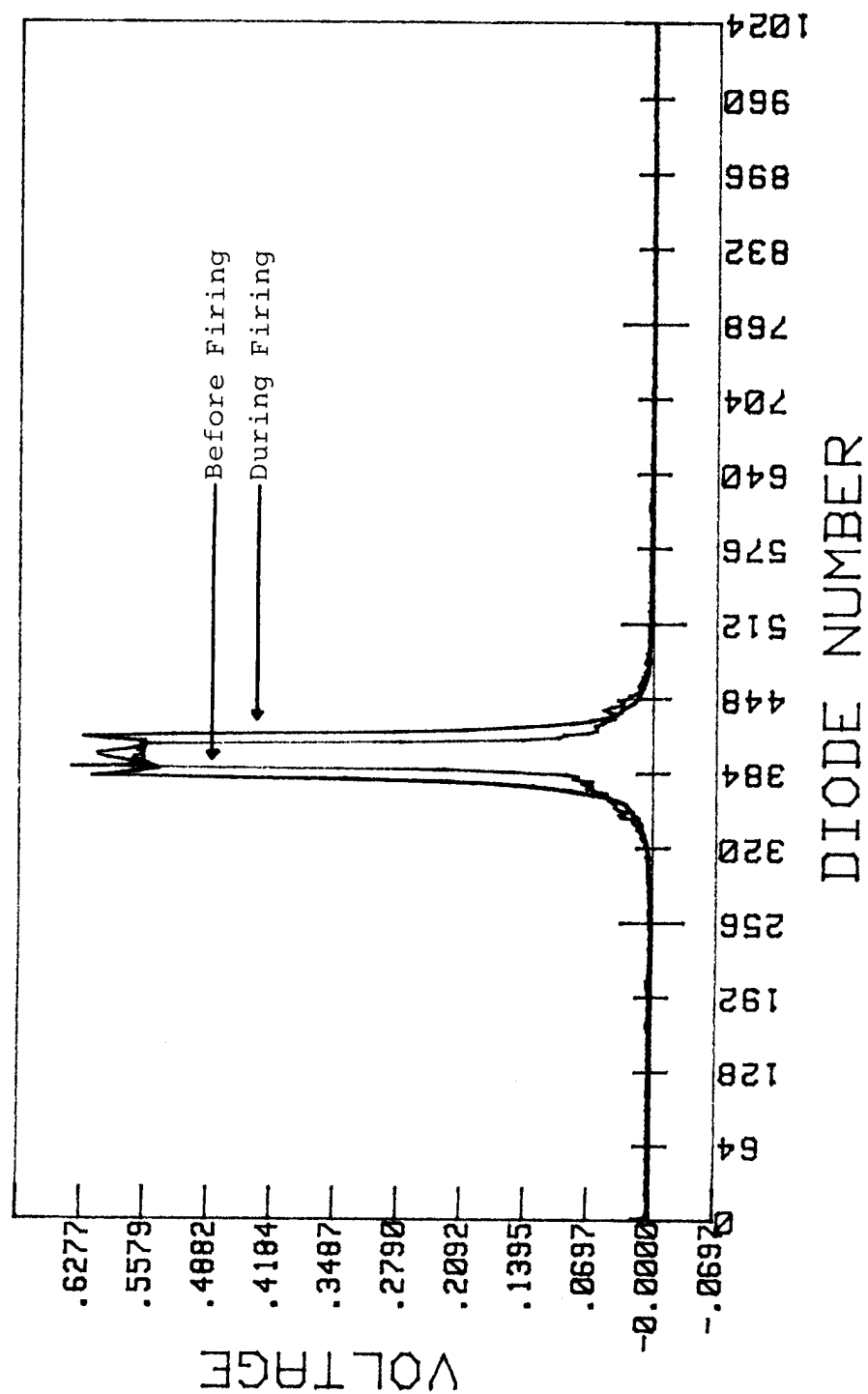


Figure 16. Effect of Exhaust on Transmitted Light, 2% Aluminized Propellant

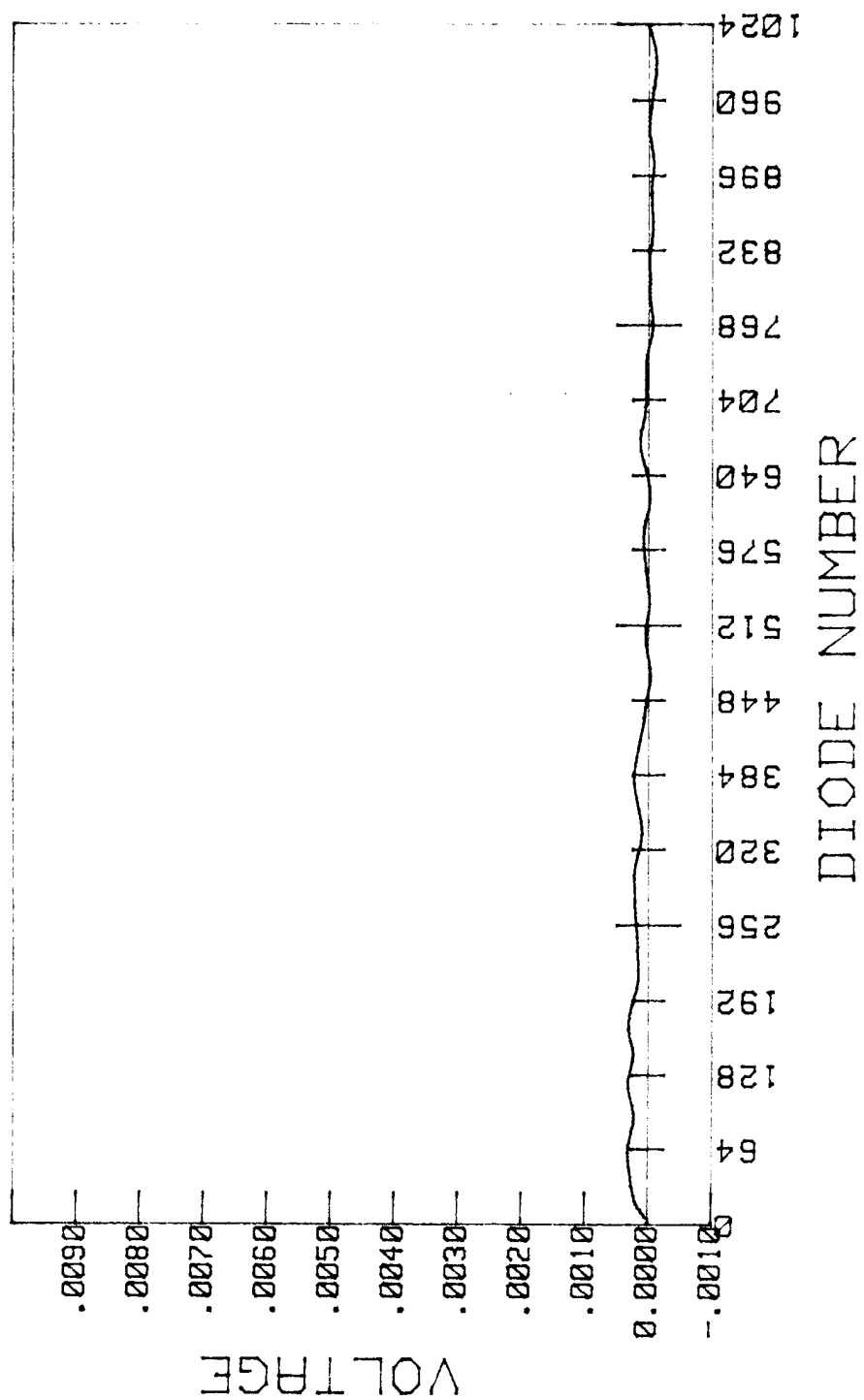


Figure 17. Scattered Light Profile from Exhaust Jet, Nonmetallized Propellant

A one-piece spatial filter and collimating lens was used to further stabilize the illumination beam.

The next test performed on the system was a cold-flow check. High pressure nitrogen was injected into the top of the motor and allowed to flow out the nozzle, simulating an actual firing. The pressure was brought rapidly up to 300 psi. During the test the diode trace on the oscilloscope disappeared while the pressure was building in the motor. While the pressure was a constant 300 psi the trace returned to normal. When the pressure returned rapidly to zero the trace disappeared again. Transient pressure gradients in the motor during pressure rise were causing the beam to bend downward. Transient pressure gradients in the motor during pressure fall-off were causing the beam to bend upward. This phenomenon explained both the beam disappearance from the diode array in the beam spread test and the random, high intensity signals recorded at larger scattering angles. The beam disappeared from the diode in the beam spread test because the motor data was taken during the pressure rise in the motor, and therefore, the beam was displaced down and off the diode array.

In a similar fashion, the scattered light measurement problem was caused by the beam being bent below the beam stop. The high intensity light then saturated the top of the diode. The measured intensity profile at small angles was just the tail-off of the laser Gaussian on the array. The unsteadiness of the traces was probably caused by small pressure fluctuations. The zero traces that occurred during some of the runs resulted when the beam had risen back above the edge of the beam stop.

The beam spread test was performed again to test the transient pressure gradient hypothesis. The decision was made to attempt a neutral burn, during which the chamber pressure would be constant. The throat diameter of the nozzle was increased to 0.25 inches to drop the pressure to approximately 50 psi, which would yield a 5-second neutral burn. The beam stop was moved to its lowest possible position. The motor traces from this test are presented in Figures 18 and 19. The position of the Gaussian did not shift, however, there was a significant attenuation (98%). This attenuation may have been caused by the presence of smoke in the combustion chamber. The possibility also existed that some of the attenuation could still be caused by the beam moving off the array due to pressure and/or thermal gradients. The use of ring diode arrays (such as in the Malvern device) should significantly reduce the problem associated with small amounts of beam deflection.

The present configuration of the apparatus appears to yield accurate values for D_{32} for particles larger than approximately three microns. In the exhaust jet, only minor problems were encountered. However, in the motor, where windows are present and density gradients can be large, it is much more difficult to obtain the desired data. The need for steady-state pressures and wider diode arrays (i.e., ring arrays, etc.) became apparent during the calibrations.

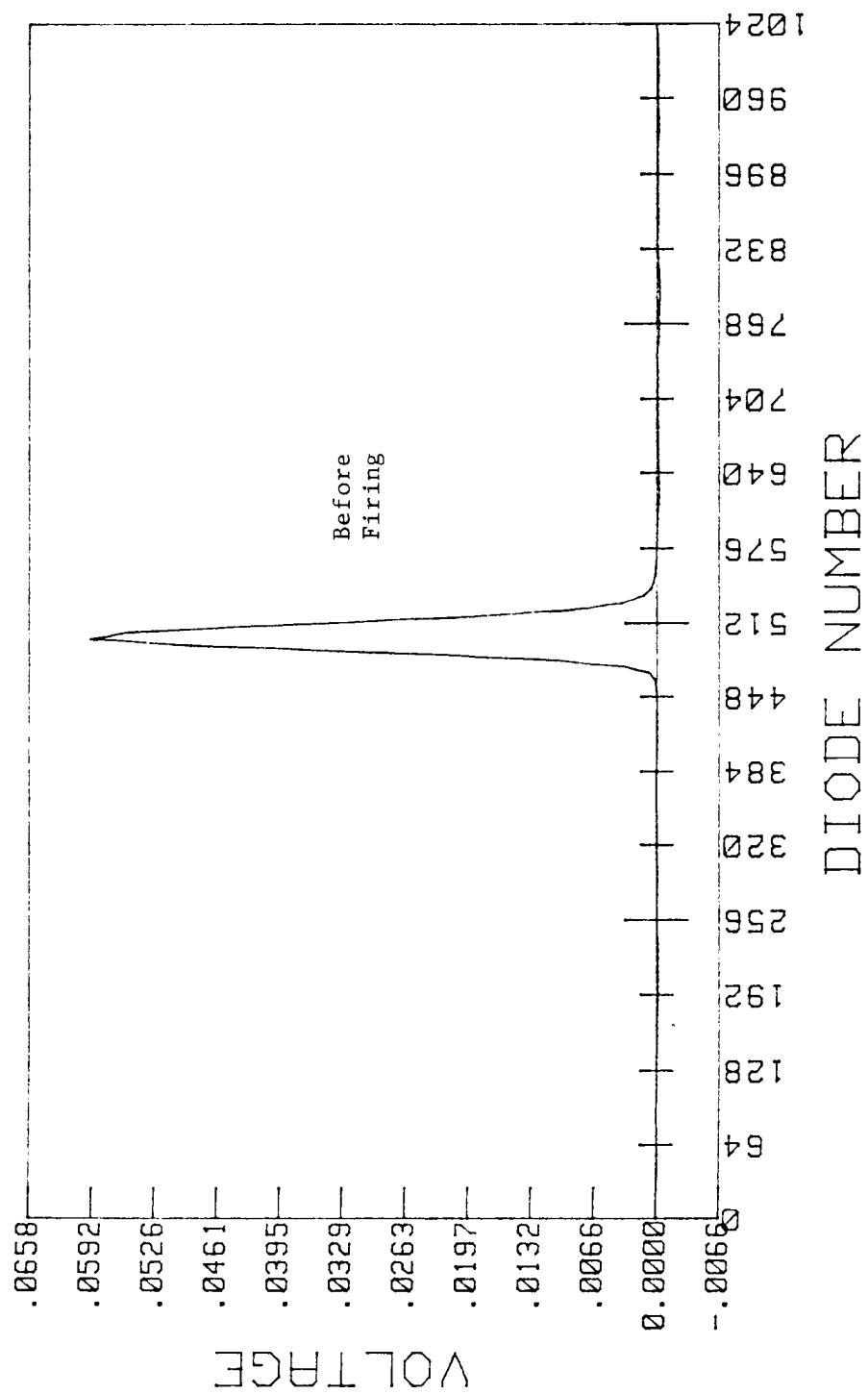


Figure 18. Effect of Combustion Products on Motor Path Transmittance, Preburn

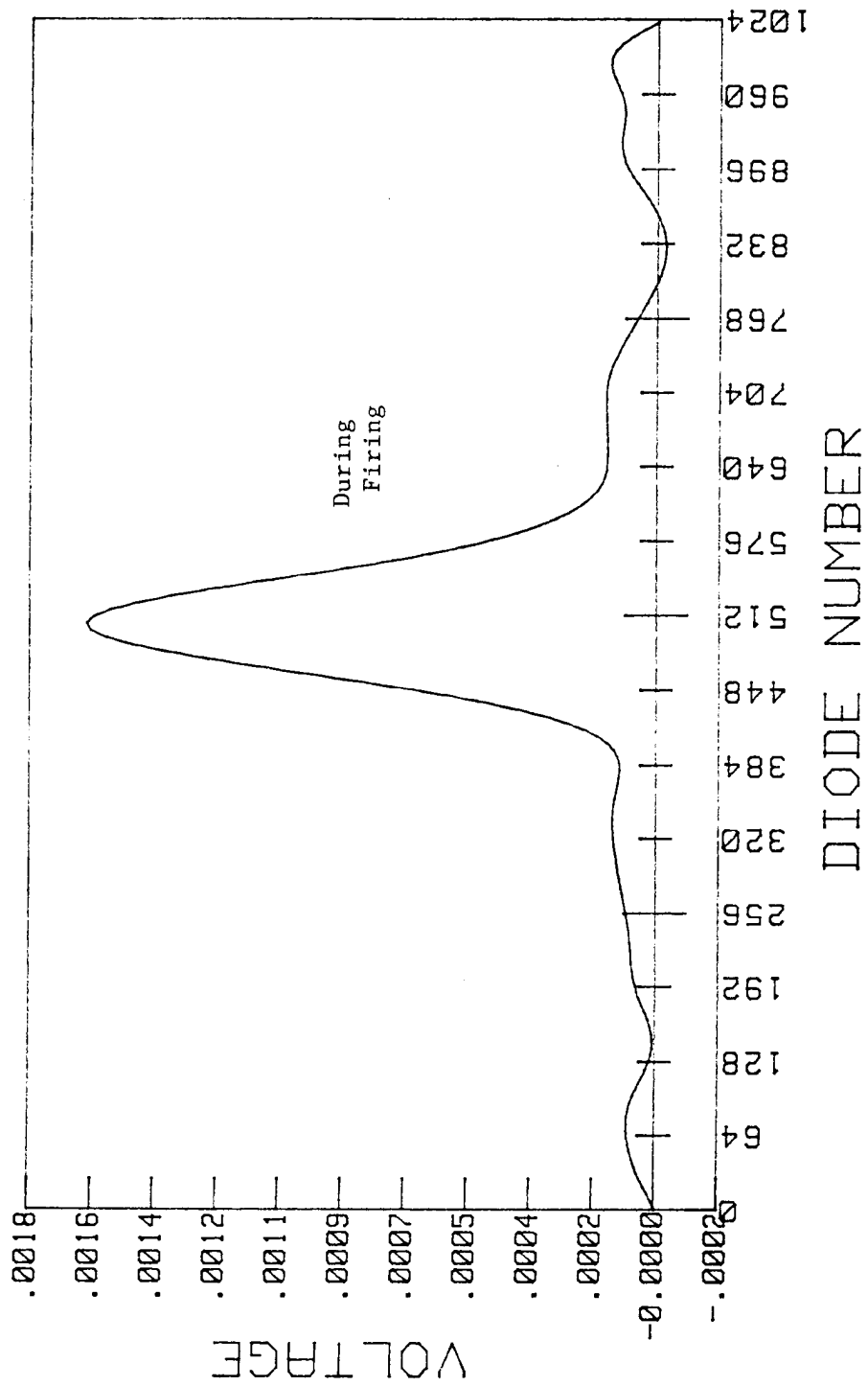


Figure 19. Effect of Combustion Products on Motor Path Transmittance, During burn

RESULTS FROM MOTOR FIRINGS

It was apparent during the calibration tests that the size of the beam stop (used for blocking the transmitted beam) was critical for obtaining good scattering data. If the stop was too small, small beam deflections caused by thermal/density gradients would move the beam to the edge of the stop. This resulted in diffraction around the edge, and in turn, light reaching the diode array which was not the result of particle scattering. The stop was made as large as possible without blocking the smallest desired scattering angle.

Nozzle Exhaust Measurements

Two tests were initially conducted using a GAP/AP propellant containing 4.8%, 20 micron aluminum. The results were repetitive and resulted in a D_{32} value between 6 and 7 microns.

Examination of the small collected exhaust sample using the SEM (Figure 20) showed a range in particle sizes. Most of the particles were within the range of 0.5 to 1.5 microns, some were 5 microns, and a few were 7.5 microns. These results were in reasonable agreement with the measured results since D_{32} has a strong bias toward the large particles.

Three tests were then conducted using an HTPB/AP propellant with 2%, 40 micron aluminum. D_{32} values between 6 and 9 microns were obtained and again were in reasonable agreement with the SEM photographs of collected exhaust particles. Table 3 shows the test conditions for these initial experiments.

A second series of tests was conducted using 4.8% and 2% aluminized GAP/AP propellants. The motor firing data and a summary of the particle size measurements are presented, respectively, in Tables 4 and 5.

TABLE 3				
Propellant	TEST CONDITIONS FOR FIRST TEST SERIES			
	Wt.% Aluminum	Aluminum Size (microns)	Pressure (psig)	Burn Time (Sec.)
GAP/AP/TEGIN/AL	4.8	20	298	2.7
GAP/AP/TEGIN/AL	4.8	20	247	2.5
HTPB/AP/AL	2.0	40	182	3.6
HTPB/AP/AL	2.0	40	142	3.6
HTPB/AP/AL	2.0	40	115	3.7

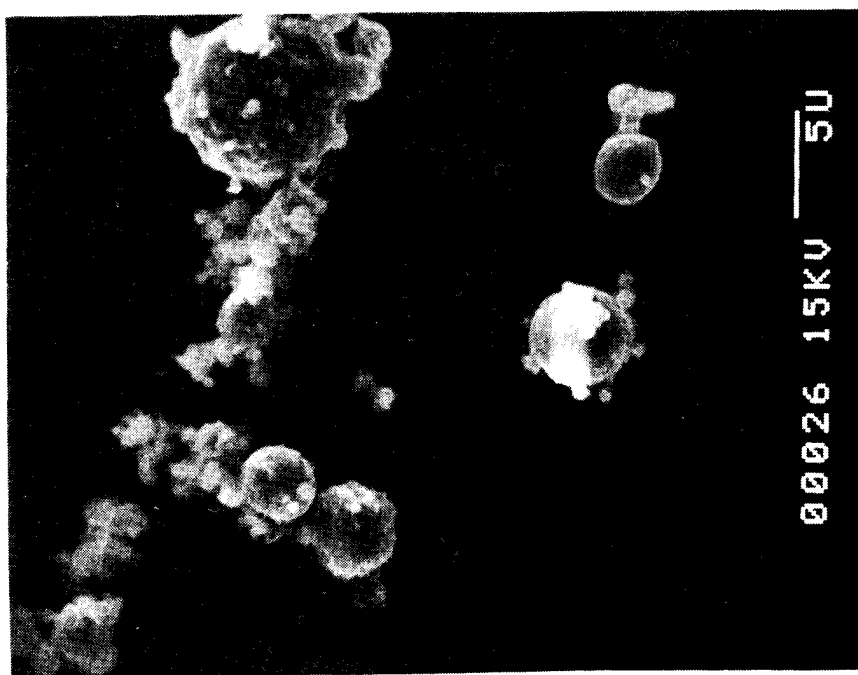
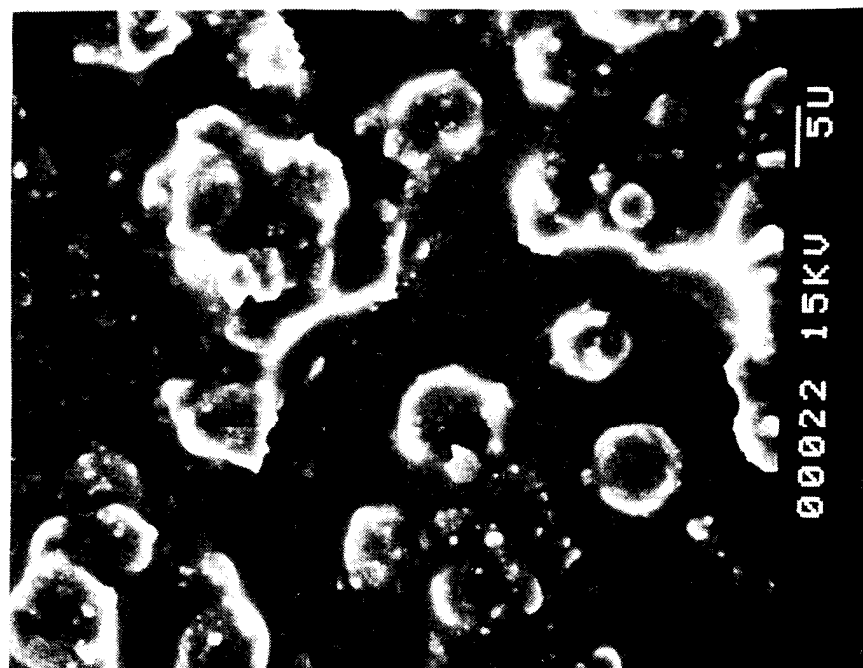


Figure 20. SEM Photographs of Collected Exhaust Products, 4.8% Aluminum

From light scattering measurements each propellant showed a similar results, one test with a D_{32} of approximately 5 microns and one with a larger value of D_{32} (12-13 microns). This test-to-test variation probably resulted from the very short burn times and the corresponding lack of a well-defined steady-state condition. The light scattering plots are presented in Figures 21 through 24. Typical SEM photographs are shown in Figure 25. The light scattering results were quite consistent with those obtained from the SEM evaluation. Although the sample sizes on which the SEM evaluations were based were relatively small (approximately 125 particle count), it still provided a good indication as to the validity of the light scattering measurements. It should be noted that D_{32} , and to an even greater extent D_{43} , are strongly dominated by the larger particles. One or two large particles can significantly change D_{32} .

The SPP equation for D_{43} (which is primarily a function of throat diameter) predicted much smaller values of D_{43} than observed in this limited set of data. The SPP model, however, is based on particulate data from motors with nozzle throat diameters greater than 1 inch.

TABLE 4 CONDITIONS FOR SECOND TEST SERIES (GAP/AP/TEGIN/AL PROPELLANT)				
Wt. of Alum. (%)	Data P_C (psig)	Max P_C (psig)	Burn Time (sec)	D_t (in.)
4.8	328	359	2.8	.28
4.8	450	466	1.0	.25
2.0	296	296	2.8	.28
2.0	566	575	1.8	.25

TABLE 5 SUMMARY OF EXPERIMENTAL RESULTS FOR SECOND TEST SERIES					
Wt. of Alum.	Press P_C	D_{32} Light Sct. Exhaust	D_{32} SEM Exhaust/Motor	D_{43} SEM Exhaust/Motor	D_{43} Exhaust SPP Model
(%)	(psig)	(Microns)	(Microns)	(Microns)	(Microns)
4.8	328	5.6	5.6/18.2	7.3/24.7	2.3
4.8	450	12.0	13.6/18.9	19.7/23.9	2.5
2.0	296	7.0	12.1/14.4	18.6/19.6	2.3
2.0	566	4.6	4.9/10.8	6.0/13.2	2.5

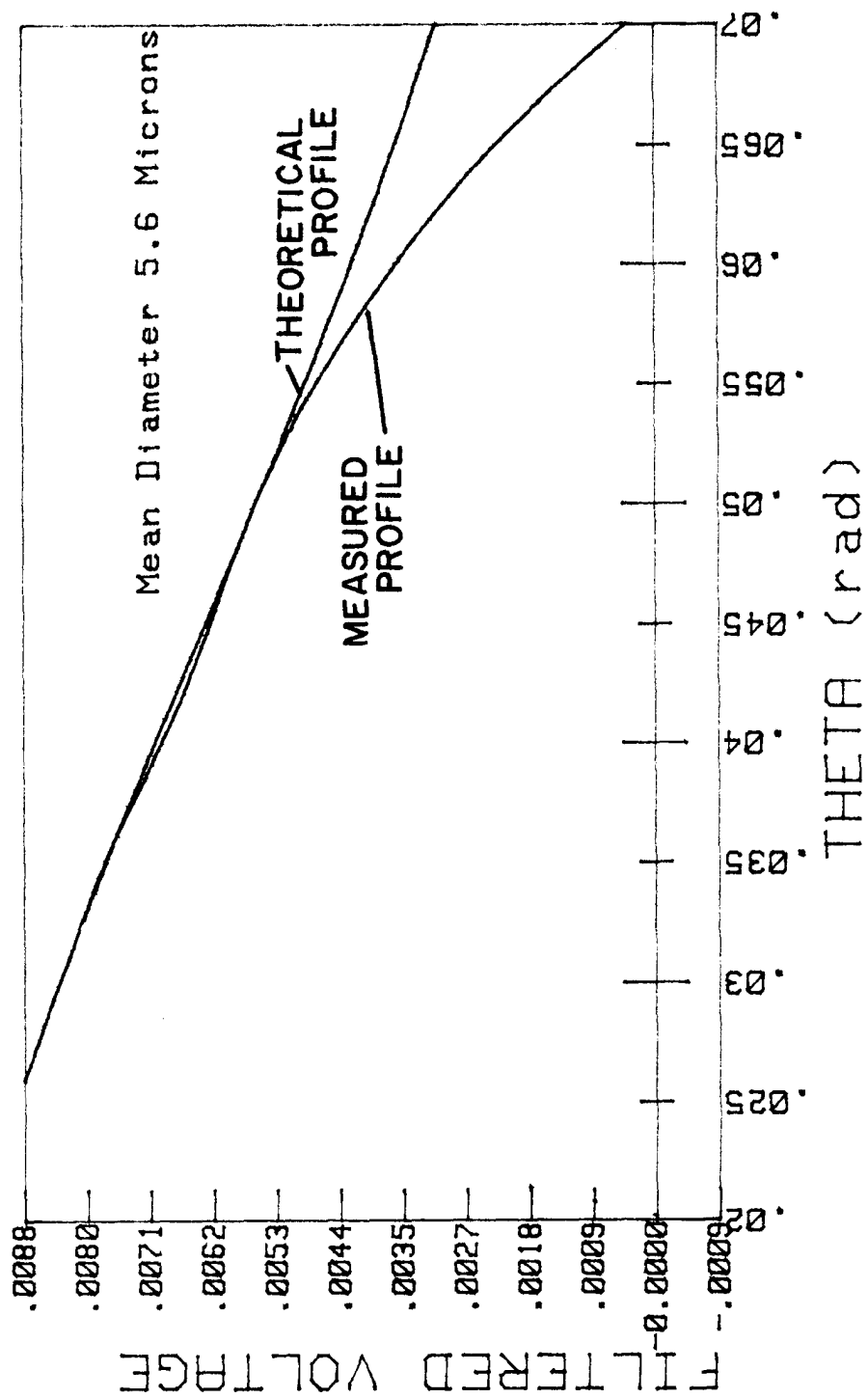


Figure 21. Scattered Light Profile From Exhaust Jet, 4.8% Aluminum, $P_c = 328$ psig

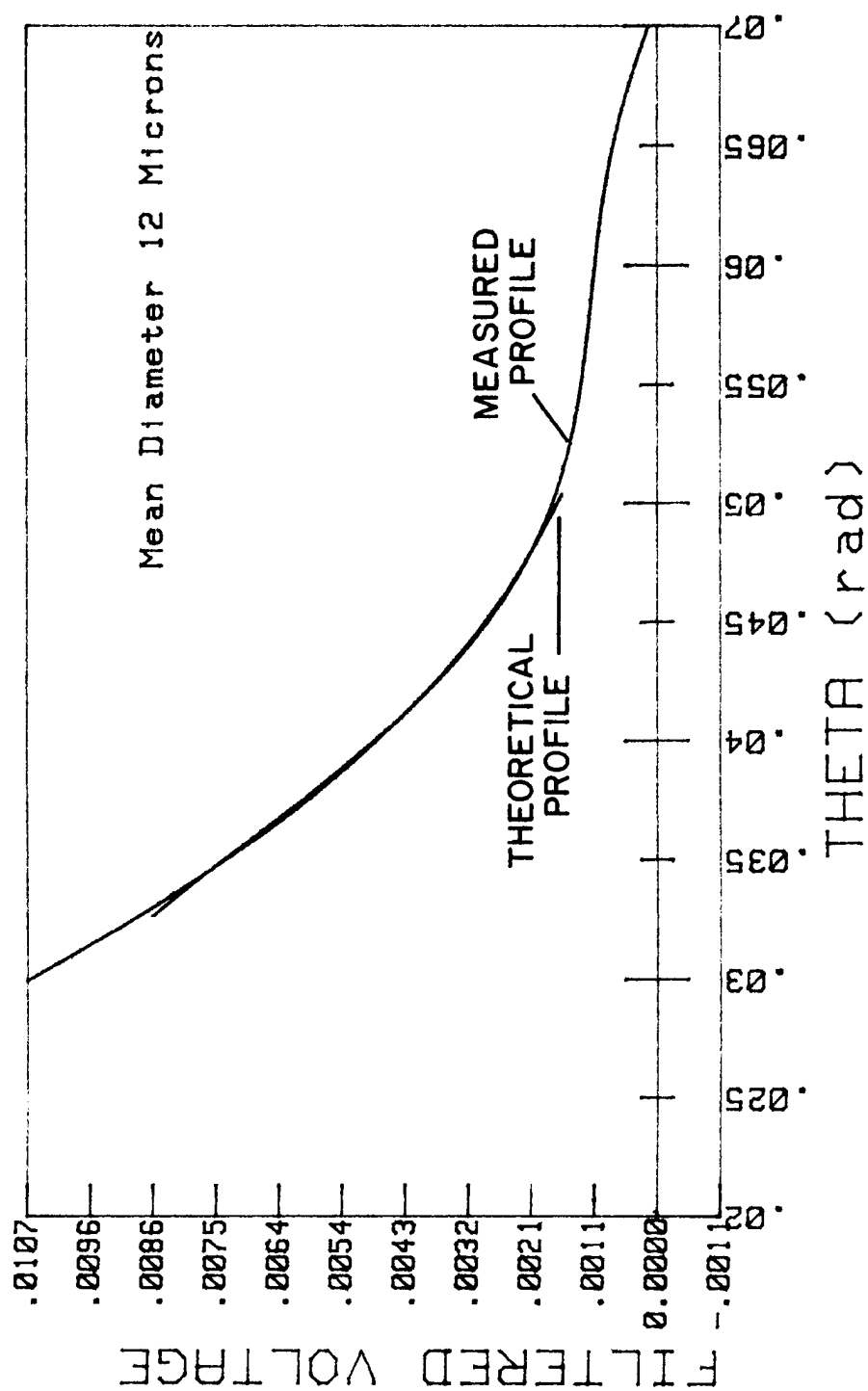


Figure 22. Scattered Light Profile From Exhaust Jet, 4.8% Aluminum, $P_c = 450$ psig

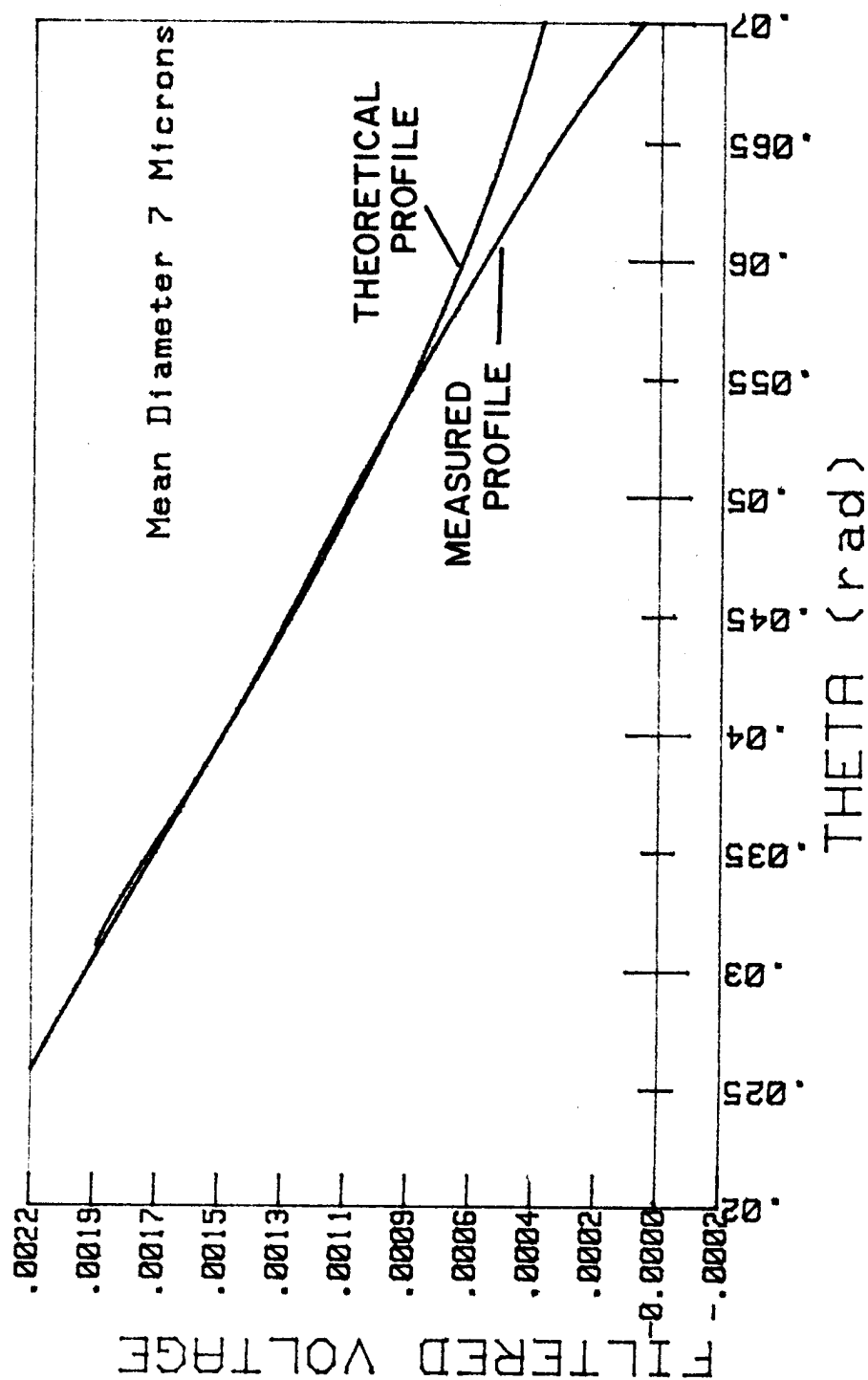


Figure 23. Scattered Light Profile From Exhaust Jet, 2% Aluminum, $P_c = 296$ psig

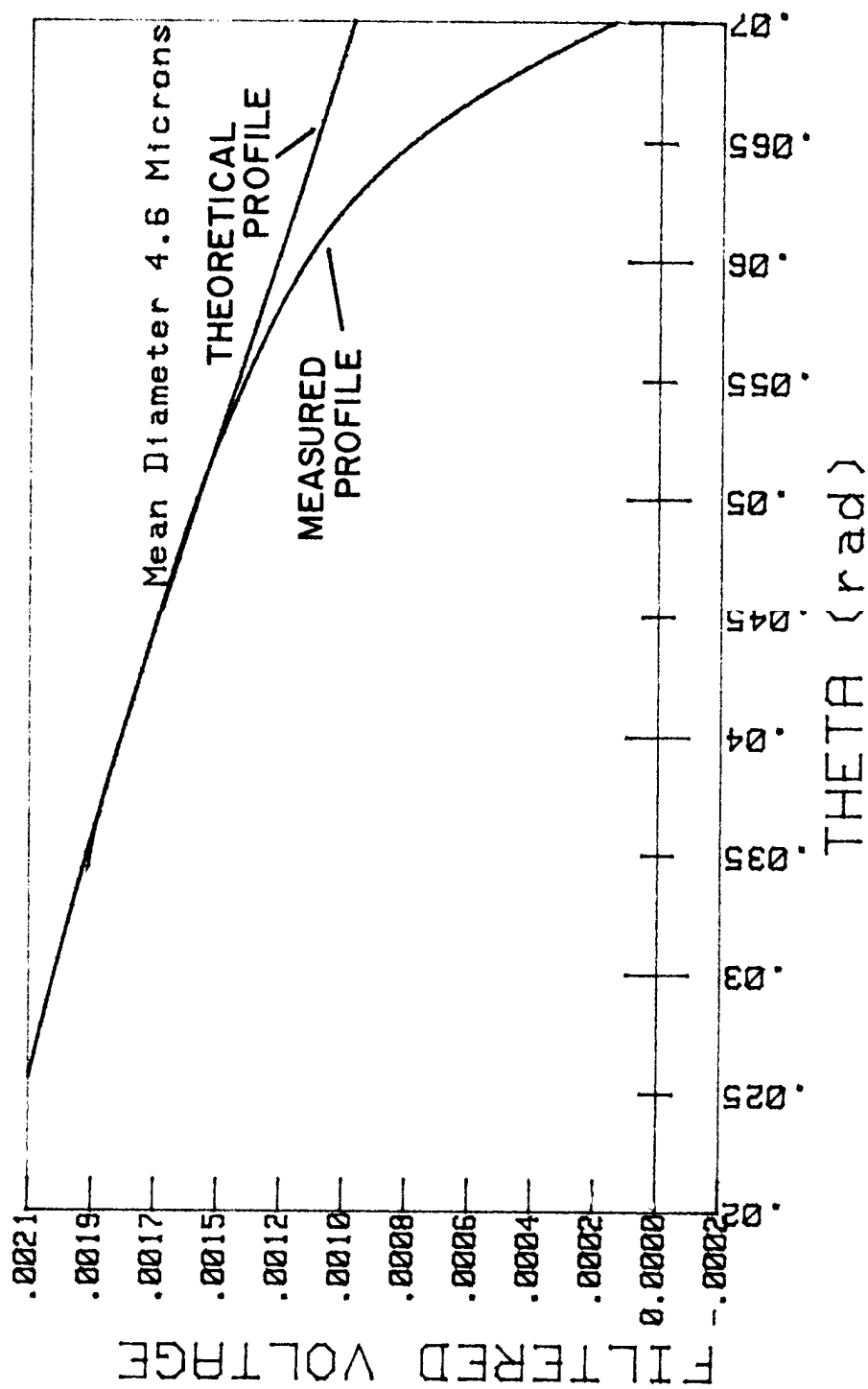
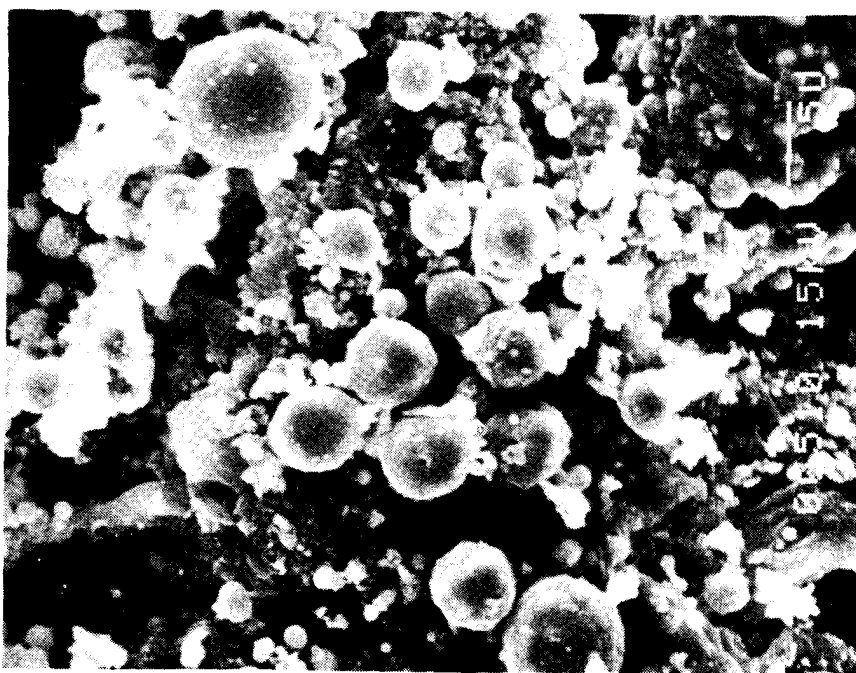
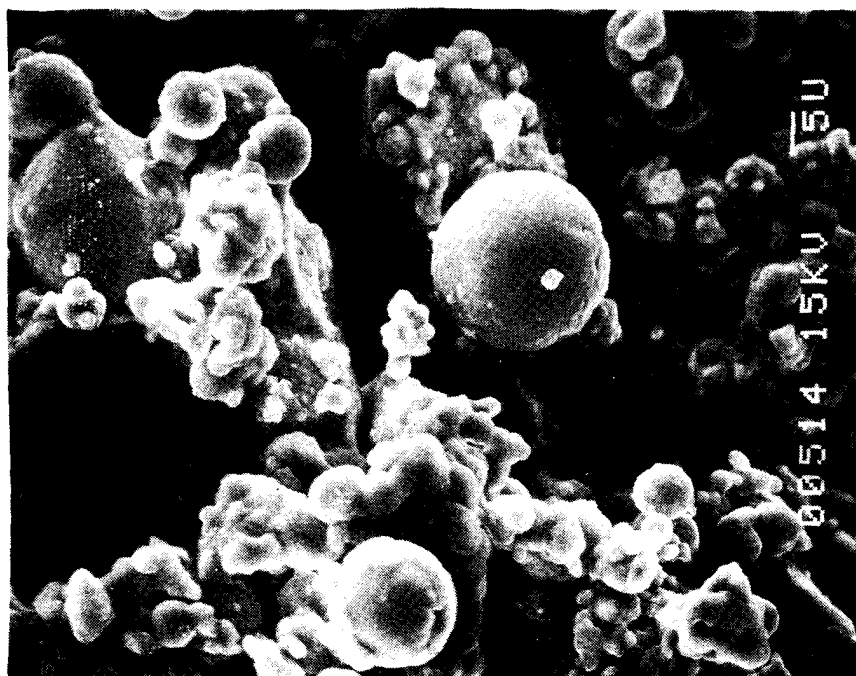


Figure 24. Scattered Light Profile From Exhaust Jet, 2% Aluminum, $P_c = 566$ psig



Exhaust



Motor

Figure 25. SEM Photographs of Collected Combustion Products, 2% Aluminum Propellant

Nozzle Entrance Measurements

In the initial test series no data were obtained through the motor windows when the GAP/AP/4.8%, 20 micron aluminum was used. Later, this was found to be due to a small shift in the laser beam (discussed above). Residue from the walls (near the window locations) were collected and examined using the SEM. Some particles in the 4 to 8 micron range were present with many between 0.5 and 1.0 microns (Figure 26). When the HTPB/AP/2%, 40 micron aluminum was used a D_{32} of 8 microns was obtained using the data at large scattering angles ($> .02$ radians). Collected samples from the walls showed particles in the 9-10 micron range, with many less than 3 microns (Figure 27).

In the second test series no motor light scattering data were obtained, apparently for the same reasons as discussed above. Table 5 shows that the particles had an approximate D_{32} between 11 and 19 microns. Thus, a significant reduction in particle size occurred across the exhaust nozzle.

Conclusions from Initial Tests

The results from the two initial test series showed that particle sizes can be readily measured in the exhaust jet, although the present optical arrangement limits the minimum particle size for accurate measurement to approximately three microns. Motor data were obtained for only one test. Major difficulties occurred due to (found later) the laser beam being slightly deflected, resulting in (1) transmitted light passing by the beam stop and (2) a movement off of the diode array (which was only 25 microns wide). The SPP model underestimated D_{43} for the small motor (with a throat diameter less than one inch).

RESULTS FROM MOTOR FIRINGS - PARTICLE INJECTION

The particle size distribution which leaves the propellant surface, and subsequently changes due to combustion, is a complicated function of the propellant composition and the motor operating conditions. In an attempt to help separate the effects of the gas phase processes from the propellant surface processes the apparatus was modified. The motor was mounted vertically with a particle injection device attached at the head-end. Particles of known composition and size distribution could then be introduced into the motor. In these tests a non-metallized propellant (15% HTPB, 86% AP) was used to provide the hot gas environment and the particle mean sizes were again measured at the entrance and exit of the exhaust nozzle.

High speed motion pictures and holograms of the particles as they dropped through the motor in non-burning tests indicated that they were uniformly distributed within the motor, aft of the propellant grain.

When burned at 200 psi the propellant would produce a theoretical combustion temperature of 2860 K. Therefore, two different available spherical particle compositions were used: glass beads (melting temperature of approximately 1700 K) and aluminum oxide (melting temperature of 2320 K).

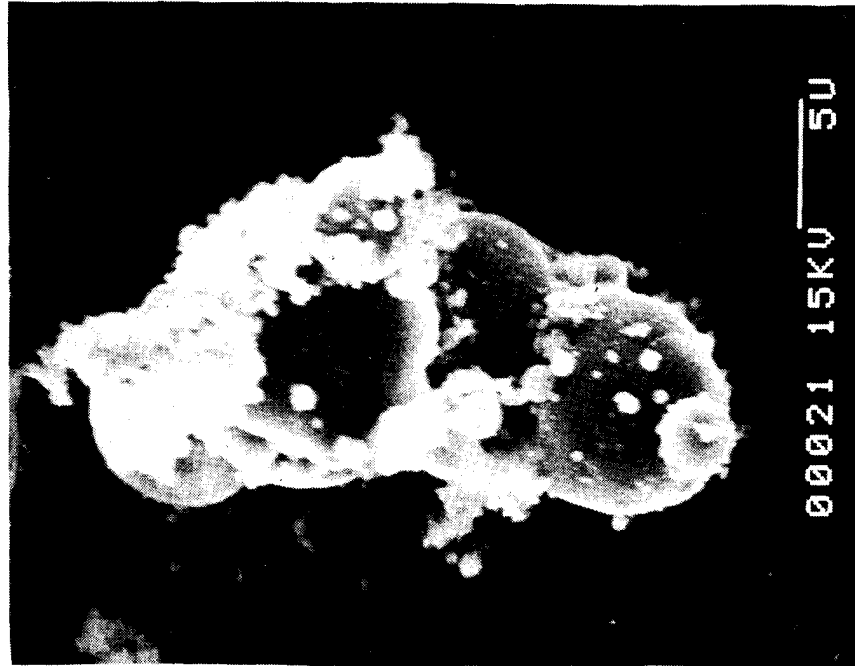
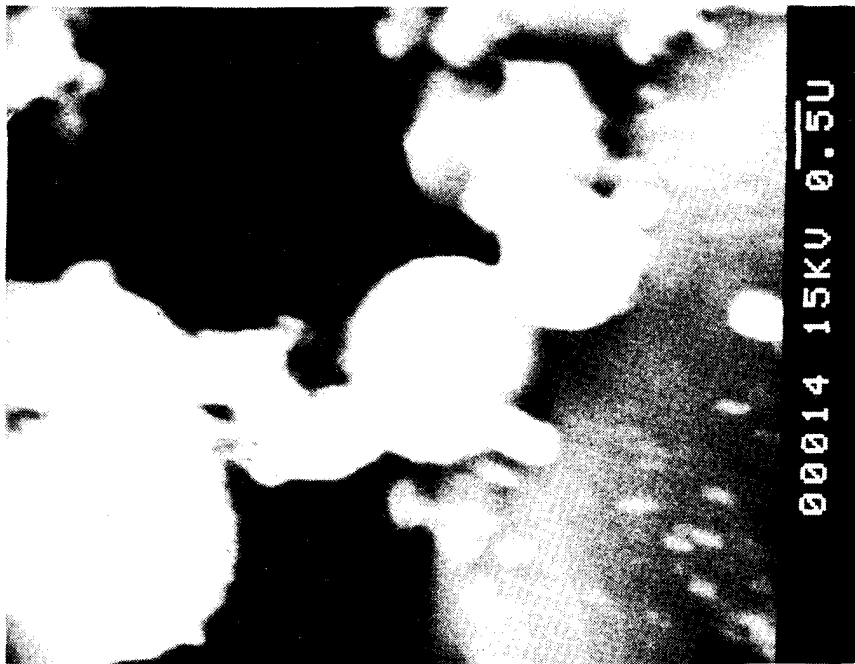


Figure 26. SEM Photographs of Collected Motor Cavity Products, 4.8% Aluminum Propellant

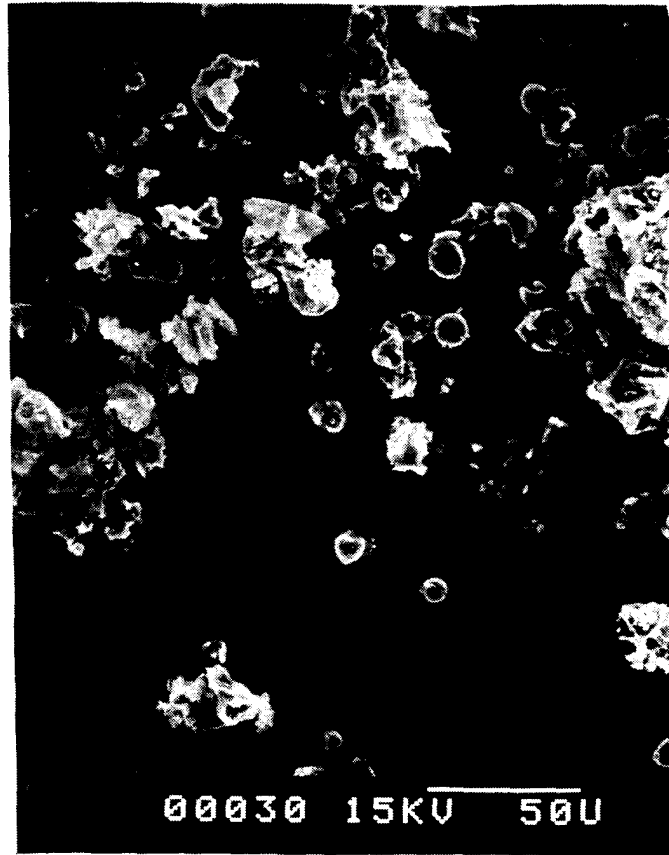


Figure 27. SEM Photograph of Collected
Motor Cavity Products, 2%
Aluminum Propellant

Glass Beads Injection

Three tests were conducted where glass beads (with a distribution of 1 to 37 microns and a calculated D_{32} of 25 microns) were fed into the ignited motor. The motor firing data and a summary of the particle size measurements across the nozzle are presented in Table 6. Typical measured intensity profiles are presented in Figures 28 and 29. The particle size did not change appreciably across the exhaust nozzle, indicating that most of the particles probably did not have sufficient time to melt. Additionally, it is interesting to note the wide variation in chamber pressures (310 to 600 psi) when glass bead particles were fed into the motor, especially when the chamber pressure of the base propellant without particles added never rose above a pressure of 230 psi.

TABLE 6 SUMMARY OF 25 MICRON GLASS BEADS FIRINGS			
P_c Data (psig)	P_c Max (psig)	Measured	
		Motor D_{32} (microns)	Exhaust D_{32} (microns)
320	350	21	13
275	310	22	18
600	600	24	22
Notes: Calculated D_{32} of powder from SEM = 25 microns. Measured D_{32} (light scattering) of powder = 24 microns.			

Aluminum Oxide Injection

Five tests were conducted where aluminum oxide, with a distribution of 1 to 44 microns and a calculated D_{32} of 30 microns, were fed into the ignited motor. The firing data and a summary of the particle size measurements are presented in Tables 7 and 8. The light scattering diameter measurements were fairly consistent within each test run, but were significantly smaller than the calculated diameters from SEM evaluations of collected particles.

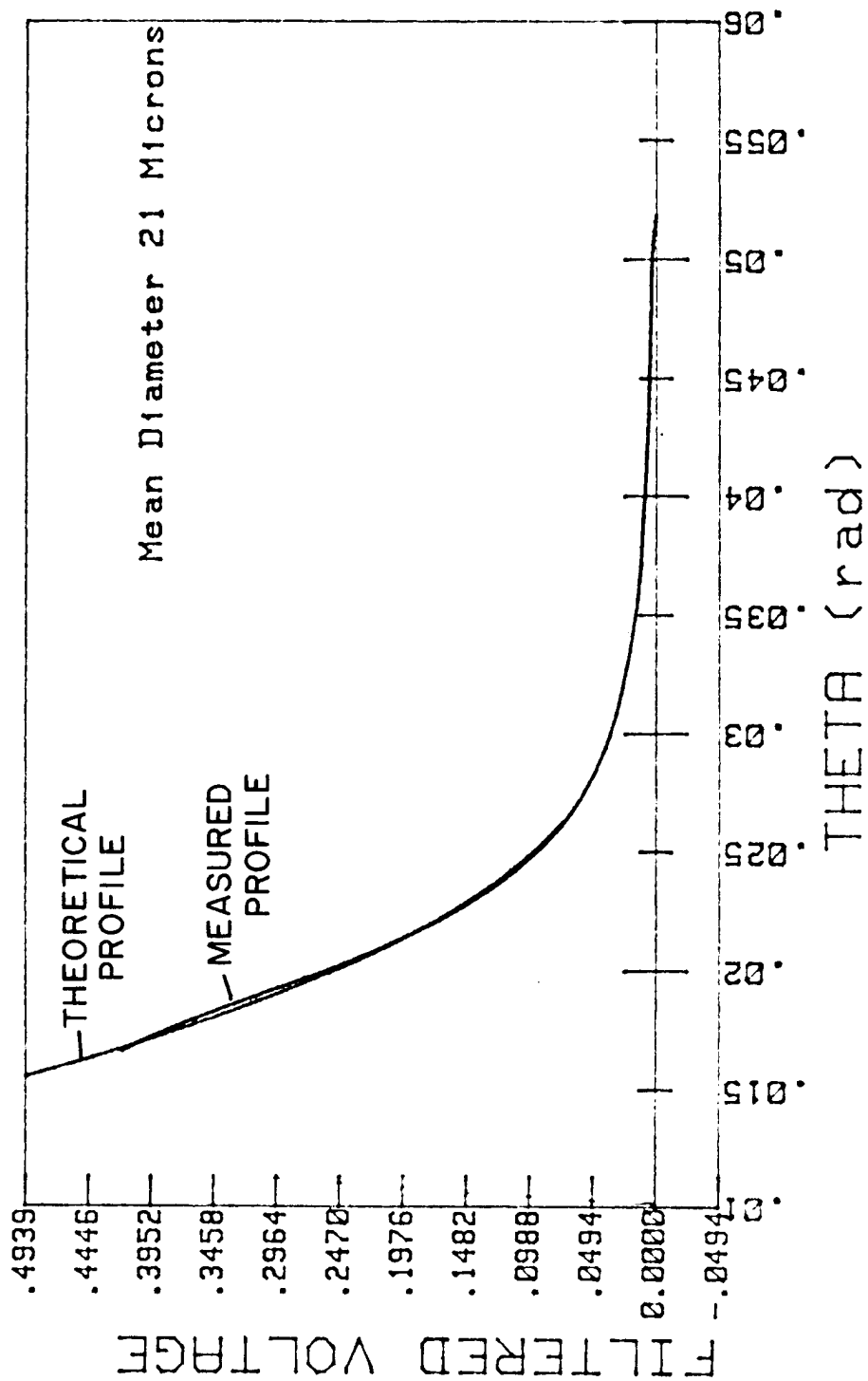


Figure 28. Scattered Light Profile Through Motor, Glass Bead Injection, $P_c = 320$ psig

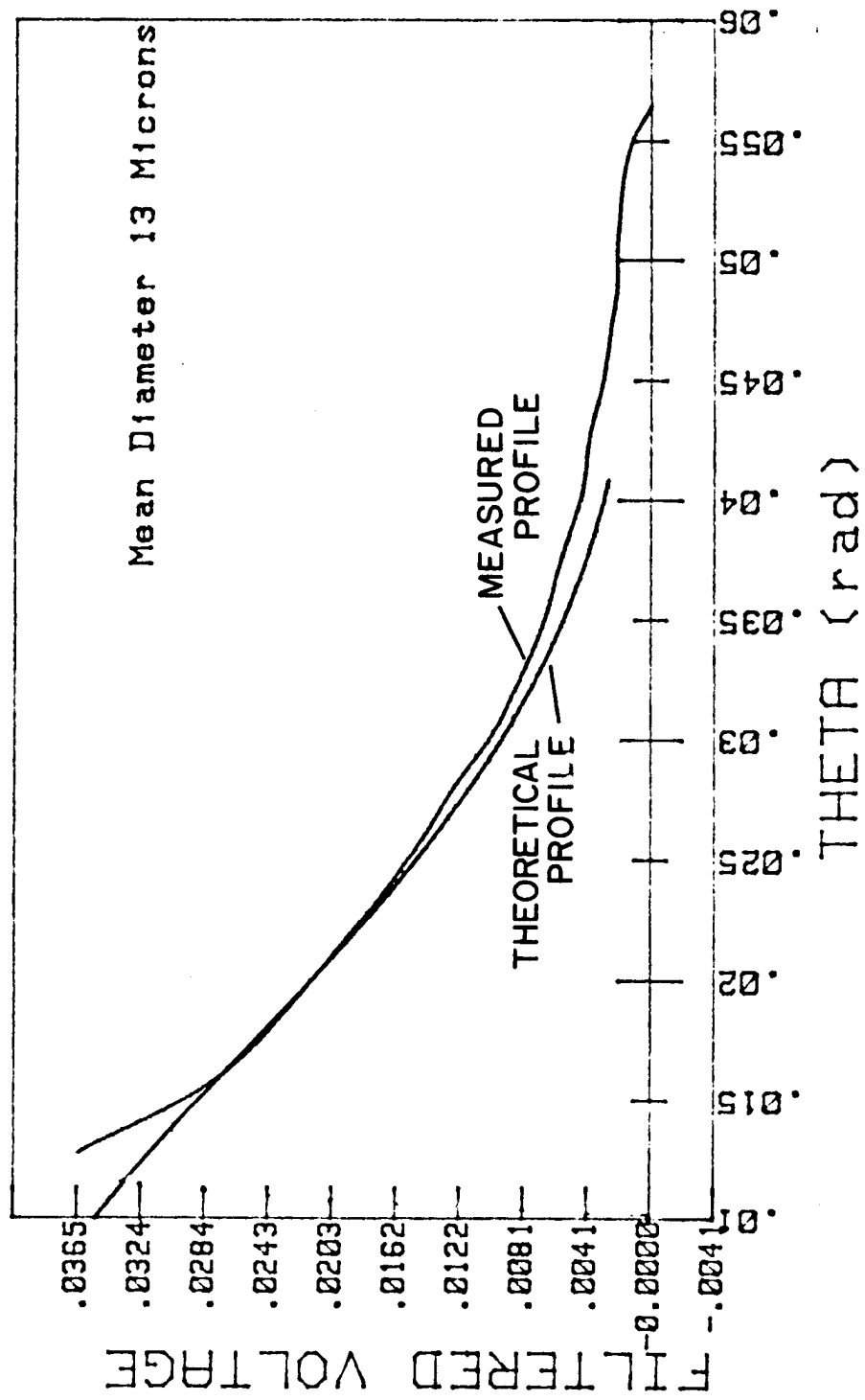


Figure 29. Scattered Light Profile Through Exhaust Jet, Glass Bead Injection, $P_c = 320$ psig

<p align="center"><u>TABLE 7</u> SUMMARY OF LIGHT SCATTERING DATA FOR ALUMINUM OXIDE FIRINGS</p>				
P _C Data (psig)	P _C Max (psig)	Measured		Calibration D ₃₂ (Microns)
		Motor D ₃₂ (Microns)	Exhaust D ₃₂ (Microns)	
(-)	(-)	29	33	(-)
220	430	(-)	30	(-)
290	315	23	18*	22
335	420	21	25	23
260	285	20	25	22
390	500	22	28	25
<p>Notes: (-) indicates sample not taken or data not obtained. *profile obtained in last scan of exhaust and is lower for this reason.</p>				

<p align="center"><u>TABLE 8</u> SUMMARY OF SEM DATA FOR ALUMINUM OXIDE FIRINGS</p>				
Sample D ₃₂ (Microns)	Nozzle* D ₃₂ (Microns)	Exhaust** D ₃₂ (Microns)	Calculated Mass Flows	
			Particles	Motor Gas
(-)	(-)	(-)	3.0	(-)
(-)	(-)	(-)	1.9	61
28	31.5	33.0	1.9	44
27	31.0	34.0	1.9	59
29	35.0	31.0	1.9	40
(-)	31.5	34.5	1.9	71
<p>Notes: Mass flow for aluminum oxide and propellant are in lb/sec 10⁻³. *Particles collected from inlet face of nozzle. **Particles collected from exhaust tube.</p>				

Some possible contributing factors for these variations are that: (1) particles could continue to run out of the particle feeder onto the nozzle (where they were collected for SEM analysis) after the propellant had completed burning, (2) the potential for large agglomerates to form had increased due to combustion moisture from the burning propellant, (3) the exhaust tube, primarily used to redirect the rocket exhaust away from the optical test bench, was positioned at such an acute angle so as to not obtain a truly representative sample (reflected in the relatively small sample number), and (4) a polydispersion of 1-44 microns was a very broad distribution.

The Al_2O_3 particle size appeared to increase slightly across the nozzle, in contrast to the glass beads. A wide variation in chamber pressures was again obtained when aluminum oxide particles were fed into the motor.

System Problems

In attempting to design a realistic system for feeding particles into a rocket motor, an obvious concern was the residence time of the particles in the small motor. In the burning of a metallized propellant, the metal will become molten as it reaches the burning surface and, whether it agglomerates or not, it will be molten as it enters the gas flow. In this investigation, although the aluminum oxide particles were not molten as they entered the gas flow, it was assumed that they could become molten, depending on their size, melting temperature and residence time, prior to completing their flow through the motor. The residence times for pressures of 250, 400, and 600 psi for the distances: (1) to the end of the propellant grain, (2) to the windows, and (3) to the nozzle throat, are presented in Table 9. The residence times of the particles within the grain were quite short. However, assuming that the gas temperature was not reduced significantly (by heat transfer to the uninsulated walls) within the motor, sufficient time (approximately 50 msec) existed for at least the smaller of the glass beads and aluminum oxide particles to become molten before entering the exhaust nozzle.

A very noticeable problem in the present system was the very wide fluctuations in the chamber pressures during test runs with essentially the same operating conditions. In addition to an increased pressure, the pressure traces indicated a reduction in overall burning time as expected for an increased burning rate for the propellant. These changes were believed to be the result of particles impinging on the burning propellant surface and conducting additional heat back into propellant. This situation of impingement was undoubtedly enhanced by the relatively small grain port diameter and by the fact that the port was often cut (unintentionally) at a small angle to the vertical. One solution to this problem would appear to be to merely increase the port diameter. However, this would result in a significant reduction in the burning time. Therefore, the problem would be best solved with an increase in the rocket motor's internal dimensions.

<p style="text-align: center;">TABLE 9 CALCULATED RESIDENCE TIMES FOR PARTICLES INJECTED INTO MOTOR</p>			
Press (psig)	Propellant	Windows	Nozzle Throat
250	.28	49	90
400	.27	49	90
600	.27	48	90
<p>Note: All times in millisec.</p>			

Conclusions From Particle Injection Tests

The results of this investigation have shown that the measurement of D_{32} across the exhaust nozzle when particles of a known mean diameter are fed into the motor is possible. However, further development and use of the present apparatus is restricted to the availability of small (1 to 20 microns) spherical metal particles.

Subsequent work should consider the employment of a larger rocket motor to minimize particle impingement on the propellant surface and to provide increased residence time for particle heating.

Although the light scattering data obtained through the motor windows appeared to be consistent, there may have been some bias introduced by the slight shifting of the laser beam during motor transients, as discussed above.

HOLOGRAPHIC INVESTIGATION

One of the diagnostic techniques available for studying particulate behavior in solid propellant rocket motors is holography. For the exposed scene a hologram provides both amplitude and phase information. The latter characteristic enables a 3-D image to be reconstructed so that particles within the entire depth of field of the scene may be recorded. Flame envelopes surrounding the burning particles are readily eliminated from the recorded scene through the use of narrow pass laser line filters. Single pulsed holography provides a means for effectively stopping the motion. However, it only provides information during a single instant of the combustion process.

Smoke generation (i.e., submicron Al_2O_3 and binder products, etc.) during the combustion process presents a major obstacle to obtaining good holograms, and consists of two distinct, but related, problems. The first is that a laser can only penetrate a finite amount of smoke, and the second involves the

required reference beam to scene beam illumination ratio. To obtain a high-resolution hologram, the illumination ratio reaching the holographic plate should be between 5:1 and 10:1 and the scene beam transmittance should be greater than 10%. Test-to-test variation in the amount of smoke in the beam path can significantly affect these values. To achieve an optimum combination of low levels of combustion chamber smoke and well-developed propellant burning requires experimental determination of the most suitable propellant composition and dimensions and the optimum time for taking of the hologram during the burn.

Initial efforts utilized strand burners within a nitrogen-purged combustion bomb [Ref. 17]. Subsequent to these initial strand burner tests it was desired to obtain holograms in flow environments which more nearly approached that in an actual motor. Small two-dimensional, windowed motors were used next [Ref. 17]. Investigations into changing the recording and reconstruction geometries have also been conducted.

Holographic recordings have been made successfully using propellant strands burned at pressures of 34 and 68 atm and with various concentrations of aluminum up to 15%. It was apparent that the flame envelopes and schlieren effects could be readily eliminated from the recorded picture.

Good quality holograms were obtained for the small, 2-D motors with all propellants containing less than 5% metal additive to pressures of approximately 59 atm (the maximum attempted). A good quality hologram was also obtained with 10% aluminum at approximately 33 atm. No holograms could be obtained with 10% aluminum at pressures of 53 atm or with 15% aluminum. The 2-D motor construction method can provide good results within the above limits. Impingement of the particulates on the glass walls and a high inhibitor-to-propellant mass ratio have provided the upper limits in metal content and propellant thickness in the tests.

The present effort utilized a small 3-D, windowed motor.

DESCRIPTION OF APPARATUS

Holographic Apparatus

The laser holographic system used a pulsed ruby laser [Ref. 21] together with a holocamera [Ref. 22]. The operating wavelength was .6943 microns with a beam diameter of approximately 3.2 cm. A one joule pulse with a 50 nsec pulsewidth was used for this investigation. The pulsed laser is shown in Figure 30 and the holocamera surrounding the small motor in Figure 31.

The required intensity ratio between the scene and reference beams could be met by placing a neutral density filter in the reference beam path inside the holocamera. A proper neutral density filter was selected by measuring the transmittance through the combustion chamber during an identical test conducted before the test in which the hologram was taken. In order to eliminate the severe "schlieren" effects caused by the burning particles, diffuse scene beam illumination was employed. This diffuse illumination introduces speckle into the reconstructed images. The primary problem in sizing the particles in the reconstructed image is interference from this speckle, which can have a maximum

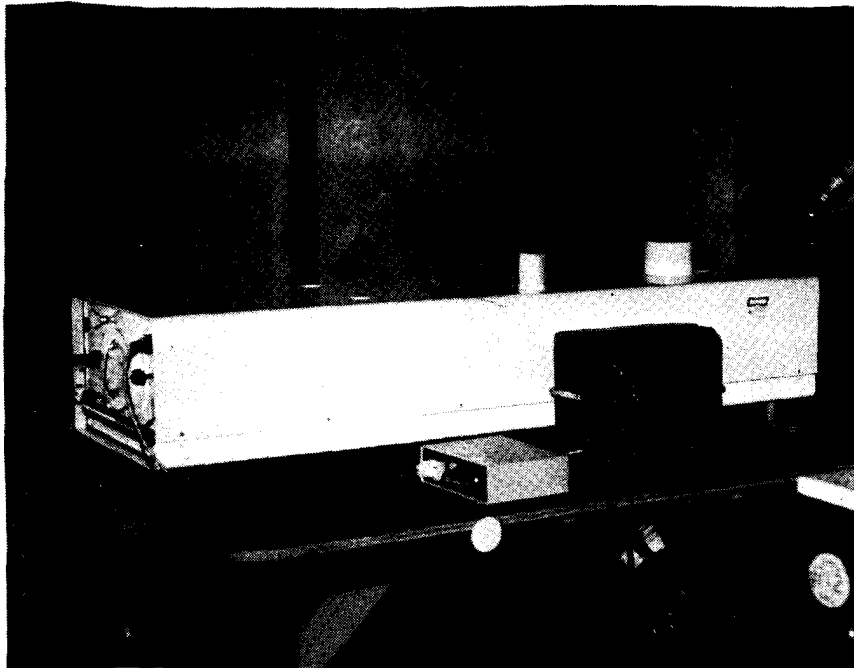


Figure 30. Q-Switched, Pulsed Ruby Laser

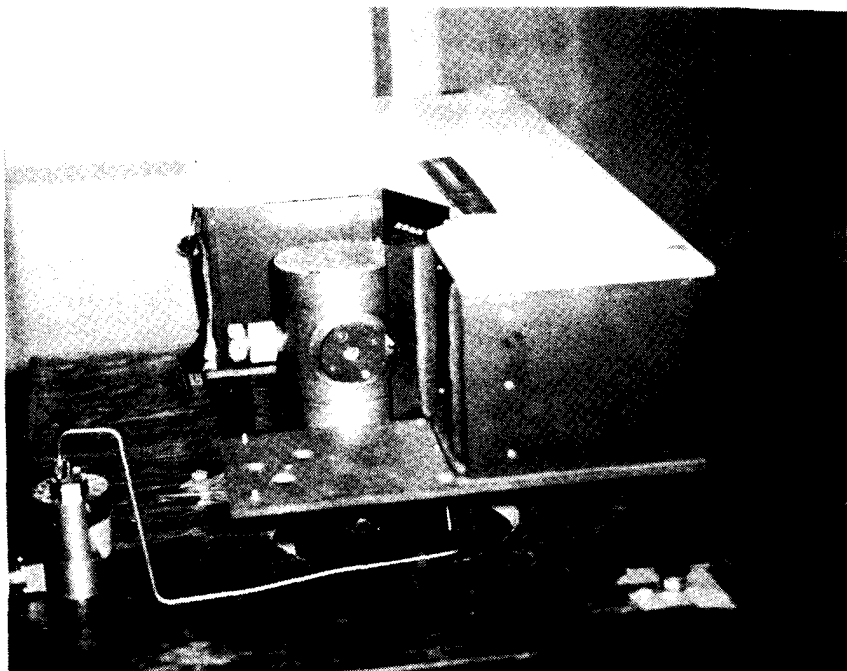


Figure 31. Holocamera Surrounding Vertically Mounted Motor

size that is comparable to the particles at the lower end of the expected particle size distribution.

During image reconstruction, the developed holographic plate was reattached to the plate holder and returned to the removable holocamera box. Rear illumination was provided by a Spectra Physics model 165-11 krypton-ion CW laser (Figures 32 and 33). This laser has an output of 0.5 watts at a wavelength of 0.6471 microns. A variable power microscope was used to directly view the hologram. In order to minimize speckle during observation and picture recording, a rotating mylar disc was used at the reconstructed object location. The mylar disc was located at the focal point of the observation microscope.

Photographs of the reconstructed scene were made using a 35mm or Polaroid camera mounted to the microscope. In addition, the reconstructed scene could be recorded by attaching a 0.5 lux, low-light-level camera and a video cassette recorder to the microscope. This was done for later image digitization and processing in order to provide automatic particle size data retrieval from the holograms.

Motor

The short 3-D motor was the same as used in the light scattering experiments discussed above. It was cylindrical, stainless steel with a copper or graphite nozzle. The chamber was two inches in diameter and two inches deep (Figure 34).

The propellant grain was cylindrically perforated and also allowed (in some tests) to burn on the aft end.

The propellant used for most tests was provided by United Technologies, Chemical Systems Division and had the following composition:

- 83.75% AP
- 14% HTPB
- 2% Al (40 micron)
- .25% Fe_2O_3

SYSTEM CALIBRATION

Two methods were used to determine the resolution limits of the holographic system: one utilizing the krypton laser and one utilizing the pulsed ruby laser for illumination. The krypton laser should provide the best resolution because of increased system coherence, and due to the matching of the wavelengths used for illumination and reconstruction. The pulsed laser system was used to determine the achievable resolution for the operating system. Two targets were used, a Laser Electro-Optics Ltd. calibration standard reticle (RR-50-3.0-0.08-102) and a 1951 USAF resolution bar target. In addition, a series of holograms was taken using the pulsed ruby laser with the targets set inside the rocket motor.

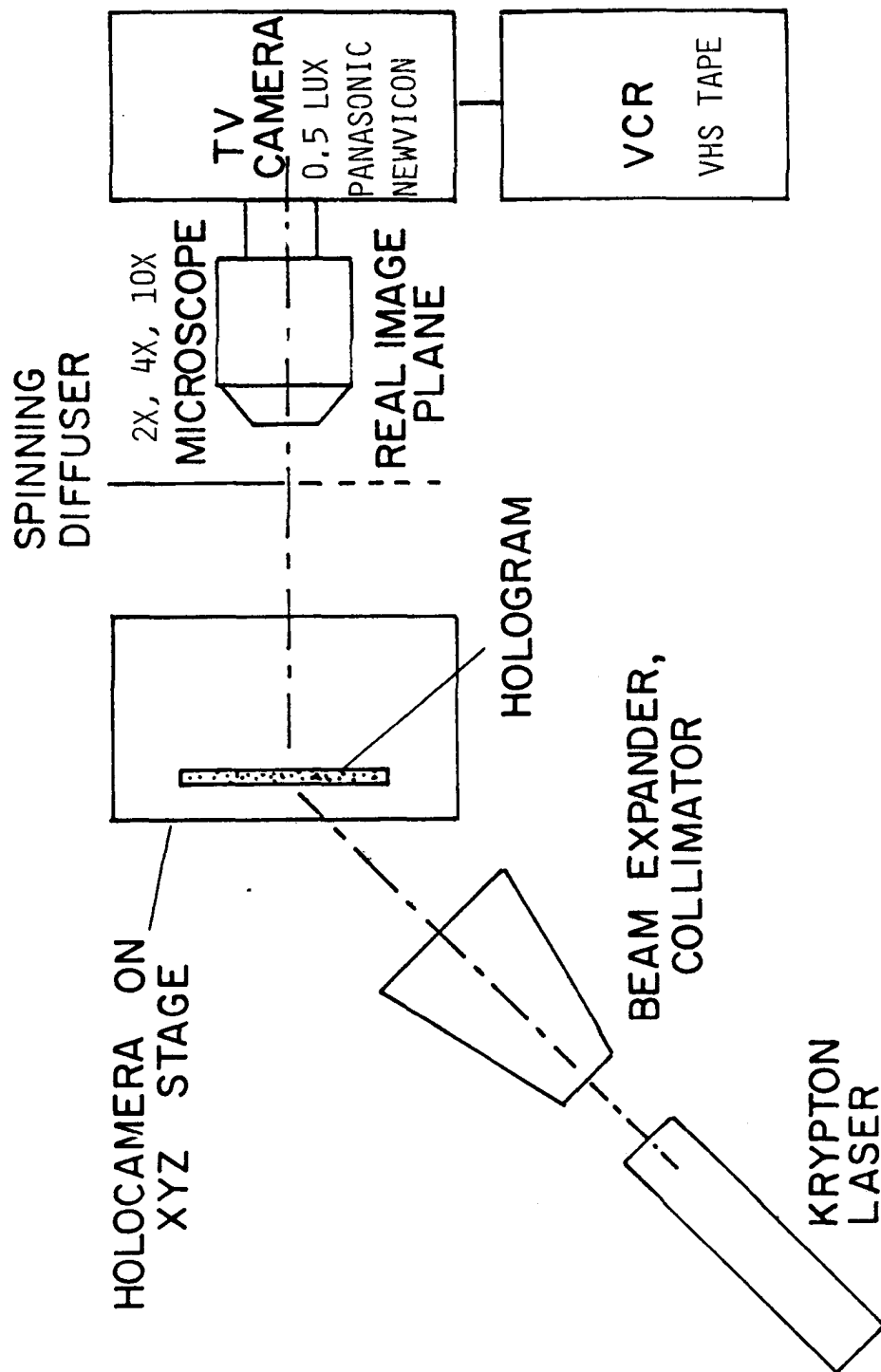


Figure 32. Schematic of Image Recording Apparatus

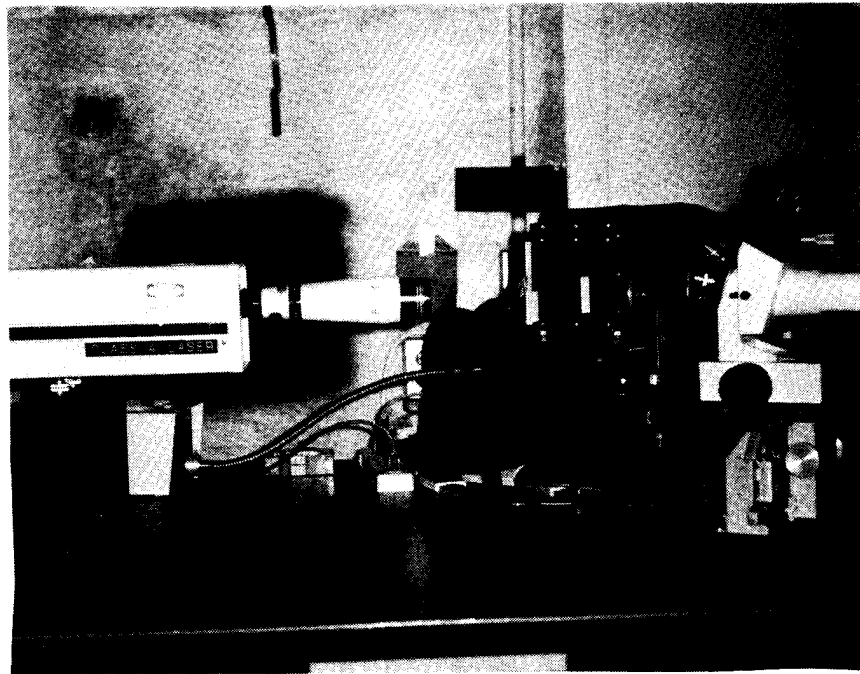
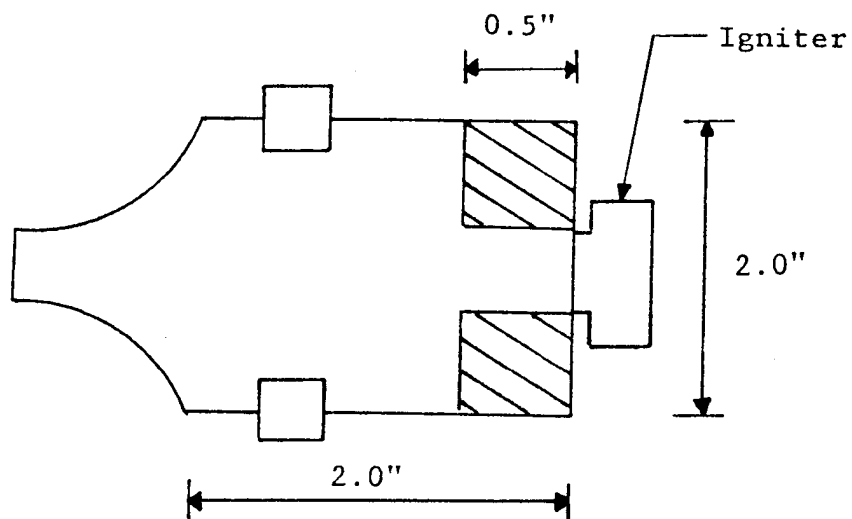
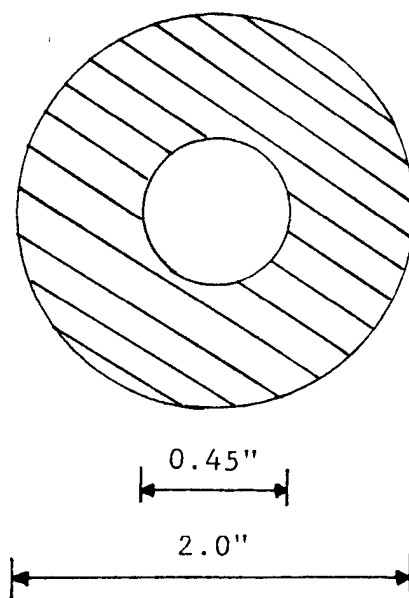


Figure 33. Hologram Reconstruction Apparatus



(a) Motor



(b) Grain Design, End-View

Figure 34. Schematic of Motor Used in Holographic Investigation

These calibration holograms resulted in a resolution of approximately 10 microns with diffuse illumination and less than 5 microns with collimated illumination. The best resolution was obtained using the bar target set inside the windowed motor and collimated light. The LEOS reticle yielded slightly less resolution, but the lower limit of this target was reached or comparable results might have been achieved. Overall, the different systems gave very similar results in their resolution as can be seen in Table 10. A typical photograph of a holographic reconstruction is shown in Figure 35.

TABLE 10 THE RESULTS OF RESOLUTION MEASUREMENTS			
Illumination	Resolution Target	Illumination Type	Resolution
Krypton	USAF	Diffuse	8.8 Microns
		Collimated	3.5 microns
	E-0	Diffuse	11.6 microns
		Collimated	6.8 microns
Ruby	USAF	Diffuse	8.8 microns
		Collimated	8.8 microns
	E-0	Diffuse	11.6 microns
		Collimated	8.9 microns
Windowed Ruby	USAF	Diffuse	9.9 microns
		Collimated	4.4 microns

RESULTS FROM MOTOR FIRINGS

Transmittance measurements were conducted using the 2% aluminized, AP/HTPB propellant in the three-dimensional motor. Two runs were performed, with each giving different results in the transmittance/pressure correlation. The first run was conducted with the head-end and sides inhibited, a 0.4 inch diameter center perforation and a 0.25 inch diameter exhaust nozzle. A pressure of 540 psi was reached with transmittance greater than zero to about 240 psi. The next run was conducted with the head-end and sides inhibited, a 0.8 inch diameter center perforation and a 0.3 inch diameter exhaust nozzle. A pressure of 270 psi was reached with a transmittance greater than zero until about 150 psi.

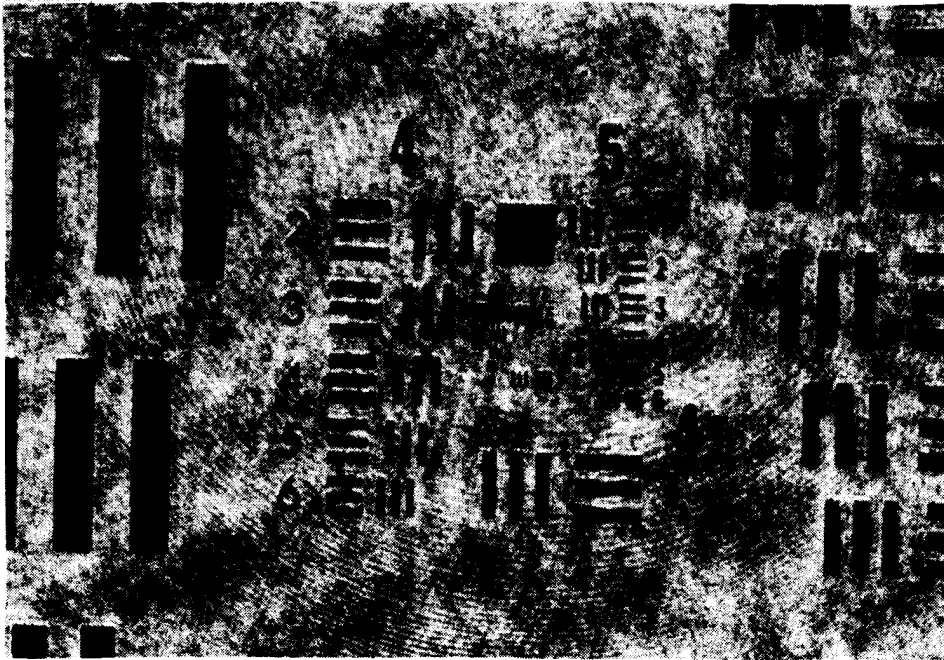


Figure 35. Photograph of Reconstructed Hologram of USAF Resolution Target Located Within Motor Cavity, Collimated Light Illumination

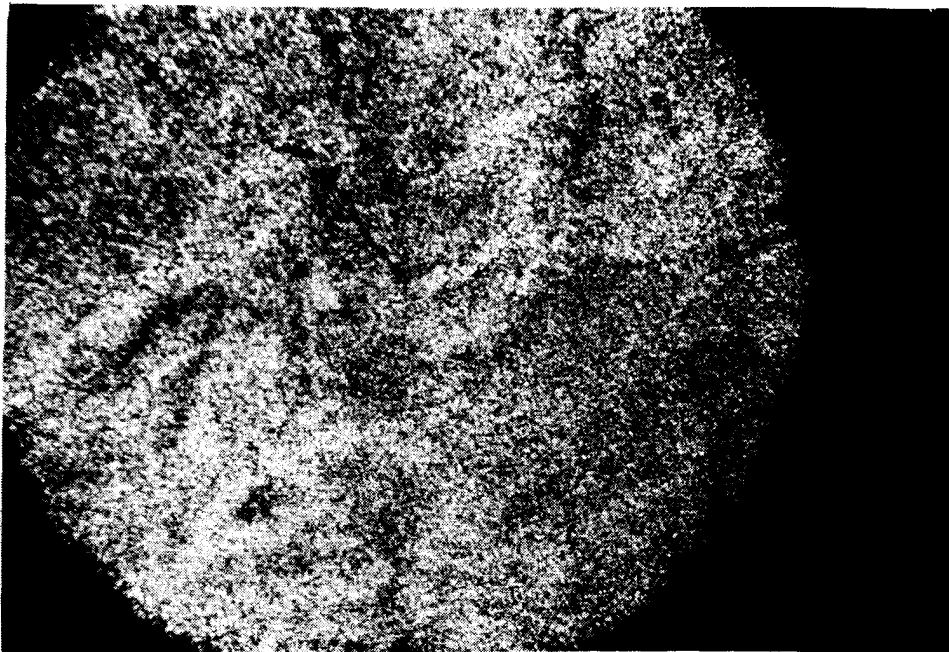


Figure 36. Photograph of Reconstructed Hologram of Propellant Burned at 280 psi

Holograms were obtained at 91, 110, and 280 psi. The particle distribution varied from run to run, with the greatest variation caused by variation of the center perforation diameter of the grain. The small diameter, 0.4 inch, had a dense center core of particles with a lighter distribution towards the walls. The larger diameter, 0.8 inch, resulted in a more even distribution throughout the motor volume. A photograph of a reconstructed hologram is shown in Figure 36.

CONCLUSIONS FROM HOLOGRAPHIC INVESTIGATION

Good quality holographs were obtained in a small 3-D motor using 2% aluminized, composite propellants to pressures of 280 psia. The inability to attain a neutral burn with the small motor, and the high opacity of the combustion products prevented holograms from being obtained at higher pressures and/or higher metal loadings.

AUTOMATED DATA RETRIEVAL FROM HOLOGRAMS

An investigation is underway to study the effects of addition of aluminum and other metallic particles on the magnitude of the performance losses in propellant motors. Performance is sensitive to the particle size distribution throughout the rocket motor and nozzle. Since no size distribution data exists in these regions of the motor for evaluation of existing analytical models, direct observation has been undertaken to provide the needed information.

Holographic techniques have been employed to capture the dynamics of the combustion chambers of small rocket motors while firing. These techniques are being refined and upgraded. Concurrently, improvements in the processing of the holograms to extract the particle size distributions are also necessary.

Once the hologram has been successfully recorded, it is desirable to have a computer process the image to measure the particle size and to produce a statistical description of the particle size distribution.

The steps required to produce this distribution follow. More complete descriptions of each step are included later in this report.

1. Image acquisition from the hologram reconstruction
2. Image digitization and storage on the computer system
3. Speckle reduction filtering to separate the particle image information from the overlaying speckle
4. Application of an image threshold to separate the image features from the background features
5. Feature identification finds connected feature pixels and "recognizes" the connected pixels as a single object

6. Feature sizing measures the number of features, the area, x-chord width, y-chord width, particle roundness, and centroid location, and
7. Histogram production using the size data of the prior step.

As an initial effort it was decided to proceed to implement the procedure described above, except for the speckle reduction which was treated as a separate problem. In this report the sizing problem is treated first and the speckle reduction technique are discussed in a separate section.

HOLOGRAPHIC RECONSTRUCTION

As mentioned in the introduction, holographic techniques are used to capture the image of a rocket combustion chamber during firing. The pulsed ruby laser utilized in the recording process uses a glass diffuser in its illumination path. This diffuser is necessary to cut down the presence of schlieren interference fringes produced by the thermal and density gradients surrounding the burning particles in the rocket motor (Refs 18 and 23).

The reconstruction process is shown in Figure 37. The hologram is reconstructed using a krypton laser and viewed through the microscope using 2x, 4x or 10x magnification. The diffuse light from the recording interferes with the reference wave of the krypton reconstruction laser. This random interference causes speckle to be introduced into the image. By attaching a 0.5 lux low-light-level camera and a video cassette recorder to the microscope, the speckle-corrupted image is recorded and preserved for later use. More detailed descriptions of the reconstruction process are in References 19, 23 and 24.

IMAGE DIGITIZATION AND PROCESSING

Once on VCR tape, the desired image is "grabbed" by either ImageAction or Itex/PC software. The digitized image then may be filtered immediately or stored on floppy disk for later use. The next step is to filter out as much speckle as possible without reducing resolution.

An IBM PC/AT is the heart of the entire process of image manipulation, from digitizing an image to speckle reduction to the counting of the features. Installed on the IBM PC/AT are a PC Vision frame-grabber board, ImageAction and Itex/PC software (all by Imaging Technology, Inc.), the computer monitor, a video monitor and a video cassette recorder.

A video image from the VCR can be "grabbed" by the frame-grabber under control of the special software. Each of the picture elements (pixels) in the 512x480 array comprising a video image is assigned an integer gray level from 0 to 255 by the frame-grabber. Level 0 on the gray scale is blackest-black. Level 255 is whitest-white, while values in between are various shades of gray. Each pixel is uniquely addressable and its gray level alterable, thereby allowing the capacity to achieve digital filtering.

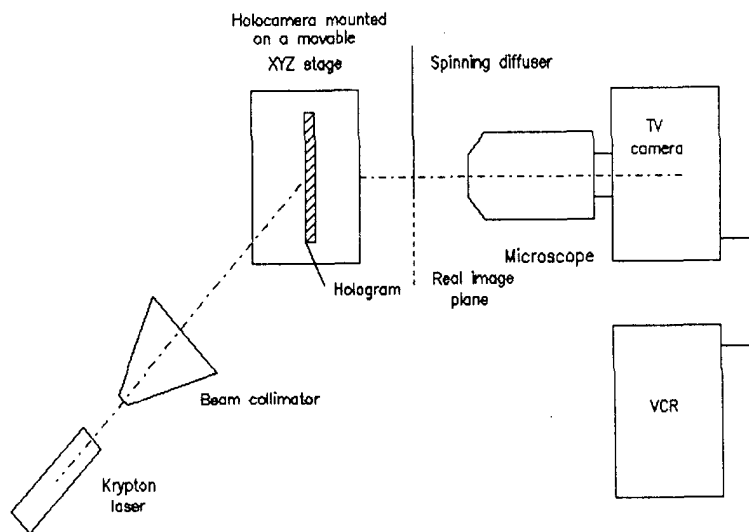


Figure 37. Hologram Reconstruction (Ref. 19)

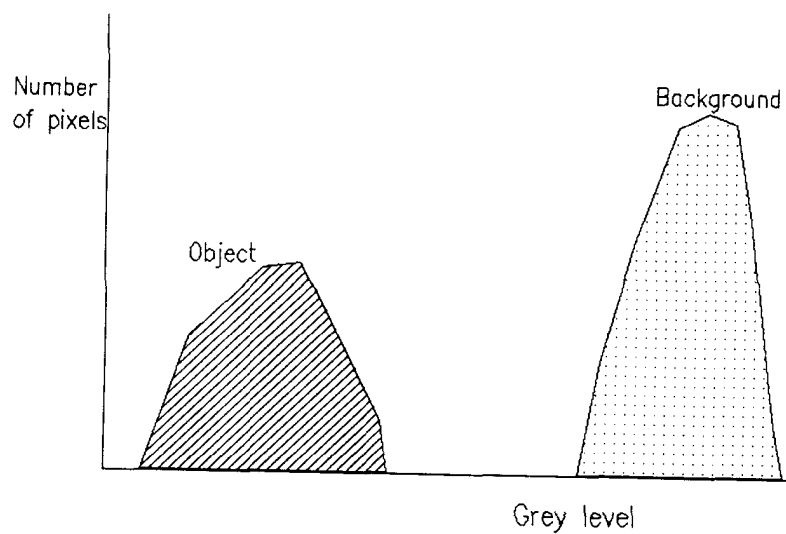


Figure 38. Ideal Histogram

The ImageAction software is a set of menu-driven routines for use with a mouse. A totally closed system, it can perform image graphics, image analysis, image processing and filtering. Particularly useful are the "grab" routine described in the preceding paragraph, and the "histogram" routine which outputs the image statistics (standard deviation, mean, variance) along with the image's histogram. More details are described in Reference 25.

The Itex/PC software performs most of the same functions as the ImageAction software (Ref. 26). An important advantage is that the Itex/PC Pascal subroutines are able to be called up in Microsoft versions of Pascal, C or Fortran programs. This allows the user a great deal of flexibility in programming.

Itex/PC consists of subroutines that may be called from a main program to perform a specific function or to return a certain value. For example, if the subroutine

```
CALL THRESH (lowcut, highcut)
```

is used to threshold an image, all the pixel values between the integers "lowcut" and "highcut" will be displayed as a new value of 255 (white). All other pixels will be displayed as 0 (black). If the "highcut" is set to 255 and "lowcut" varied by the user during run time, a binary image results which represents the black particles on a white background.

Sometimes an Itex/PC routine is treated as a function. An example is

```
L = RPIXEL (x,y).
```

Here, the gray level of the pixel located at (x,y) is read and the value is assigned to the integer L. The value of L may then be varied by one of the filtering algorithms and the new value written back into the pixel at (x,y) using

```
CALL WPIXEL (x,y,L).
```

Some specifics of Itex/PC bear mentioning. A standard television screen is made up of a 512x512 array of pixels. Of these, only 512x480 are actually visible. The lowest 32 rows are hidden out of view and may contain other information.

On the monochrome PC Vision frame-grabber board, four look-up tables (LUT's) may be utilized. A LUT serves to transform pixel values before they are displayed. The standard LUT is linear, meaning that the output values equal the input values. Certain actions, such as thresholding, change the LUT values. The actual values of the pixels in the frame-grabber board memory remain unchanged by the threshold, but are simply altered by the LUT in such a way that a binary image appears on the screen. If it is desired to make the threshold permanent and actually change the frame-grabber memory to their new values, the MAPLUT subroutine must be called. If not, a call to INITIA to initialize LUT's returns the screen to its "before-threshold" likeness.

The PC/Vision board was successfully installed in a PC/AT computer purchased to act as host. The ImageAction software proved to be extremely simple but powerful in manipulating the images. Late in the FY86, the ITEX/PC subroutine package was purchased and installed. It was successfully used in the study of speckle reduction techniques reported below.

THRESHOLDING

A histogram of an image consists of a bar graph. A separate bar exists at each gray level, with the height of the bar proportional to the number of pixels at that gray level. Thus, a histogram gives a visual representation of the general darkness or lightness of the image and how widely separated in gray level certain features may be. It can suggest where the best level to place a threshold might be.

Ideally, the feature data in an image would be very different from the background in gray level, as in Figure 38. A threshold could then be placed at a level midway between them with the result that the feature particles would be black and the background white. The program developed in Reference 25 could then be used to properly size and count the particles of interest.

In practice, Figure 39 is much more likely. Particles cover much of the range of gray levels, as does the background speckle. A threshold placed in an unfiltered image would cause portions of some particles to disappear while part of the speckle would appear as particles.

What is required is a method to process out the unwanted speckle noise in the background. With a clear separation between the particles of interest and the background, a threshold could then be applied with success.

TEST OBJECTS

Three test objects have been used in our investigations. These objects were imaged under white light as the highest contrast images with the most benign background. These images provide a resolution calibration. The objects were also recorded in holograms in the test setup to duplicate the test geometry.

The first object was a calibration reticle produced by LEOS, Inc. The circular portion of the reticle consist of approximately 10,000 opaque circular features of twenty-three sizes ranging from five to ninety-three micrometers in diameter. These circles are photodeposited in an eight millimeter circular area. An array to the right of the circular test pattern consists of the twenty-three standard sizes arranged in rows of five as seen as Figure 40.

The second object was the 1951 USAF Standard Resolution chart. This was used for resolution studies as it provides a more continuous measurement of resolution degradation than the Calibration array.

The final object was the reconstruction from rocket motor holograms recorded during firing using propellant samples supplied by the Air Force.

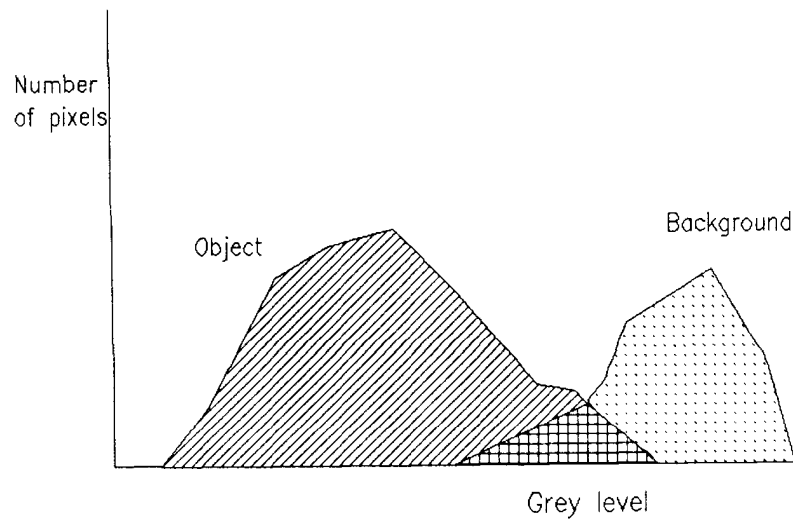


Figure 39. Histogram Showing an Overlap of Gray Levels

9	7	5		
27	24	21	17	12
43	40	37	34	31
61	56	52	50	47
93	87	81	74	67

Figure 40. Calibration Array Circle Sizes (in μm) and Relative Positions

SIZING INVESTIGATION

The initial effort (Ref. 25) focused on image capture, image digitization, and particle sizing. The ImageAction software was used under operator control to process the image to remove the speckle and background effects. Fortran programs were then used to process and size the images. Due to computation time and to computer memory size constraints, initial efforts worked with only one-quarter of the screen image (256x256 pixels). (Later improved programming and subroutines have removed those constraints.)

The processing of the digitized image proceeded as follows:

- o Image averaging to reduce speckle. Two techniques were explored: the first used a spinning mylar screen as the focus of the image. The motion of the mylar screen during the 1/30-th of a second scan time causes the speckle to blur and have reduce contrast compared to the particles. Alternatively, digital averaging of images taken without the mylar disk being present was used to reduce the speckle contrast. It was found that after approximately fifteen images were added, no further reduction of speckle was observed. Additionally the speckle reduction was found to be no better than obtained with the rotating mylar disk. Since the rotating disk was experimentally easier to implement, it was chosen for use with all subsequent recorded images.
- o The speckle was further reduced through a processing algorithm that was empirically designed. Using built-in routines of the ImageAction software, a blur filter was applied, followed by a lowpass filter. The two-step process was then repeated. When correct filtering was done the speckle was significantly reduced. It was noted, however, that resolution was also reduced and that close particles would tend to merge into one unresolved clump after processing. No attempt was made to quantize the loss of resolution at this point.
- o The next processing step was the application of a threshold to remove all information from the background. Figure 41 shows a comparison illustrating the filtering effect. Figure 41a is a thresholded image after the image was averaged but not filtered before applying the threshold. Significant error due to the speckle effects is present. Figure 41b shows the same image but with the speckle reduction filter applied before applying the threshold. Far less noise is present. (The calibration array object also suffered some physical damage before the image was made causing the loss of the center circle in the top row of Fig. 41b as well as some damage to some of the larger circles.)
- o The threshold image was then processed by the Fortran routine for object identification, counting and sizing. The object identification is done by scanning the data array for adjacent pixels (currently in the horizontal and vertical directions only, with no check made on diagonals). Adjacent pixels are joined to form one object or "feature". The area and maximum chord widths are then computed for each object and written into a data table. (If desired, a roundness test can applied to the chord length measurements to eliminate



nonspherical particles.) This data table is processed to produce the final histogram data on particle size.

MEASUREMENT RESULTS

Figure 42a shows the histogram of particle sizes on the calibration array as provided by the manufacturer. Imaging tests showed that the system was unable to resolve particles smaller than the size marked as "threshold" on Fig. 42b. This resolution threshold was approximate due to the quantization of the particle sizes in the sample. Removing particles smaller than the nominal resolution limit of 10 micrometers produced the histogram of Fig. 43a. Figure 43b shows a measured histogram from an image without speckle with 151 particles present in the image. The agreement in the shape was relatively good. There was a presence of small particles ($< 1 \mu\text{m}$) that was primarily due to the size quantization into pixels and partially due to noise spikes present in the image.

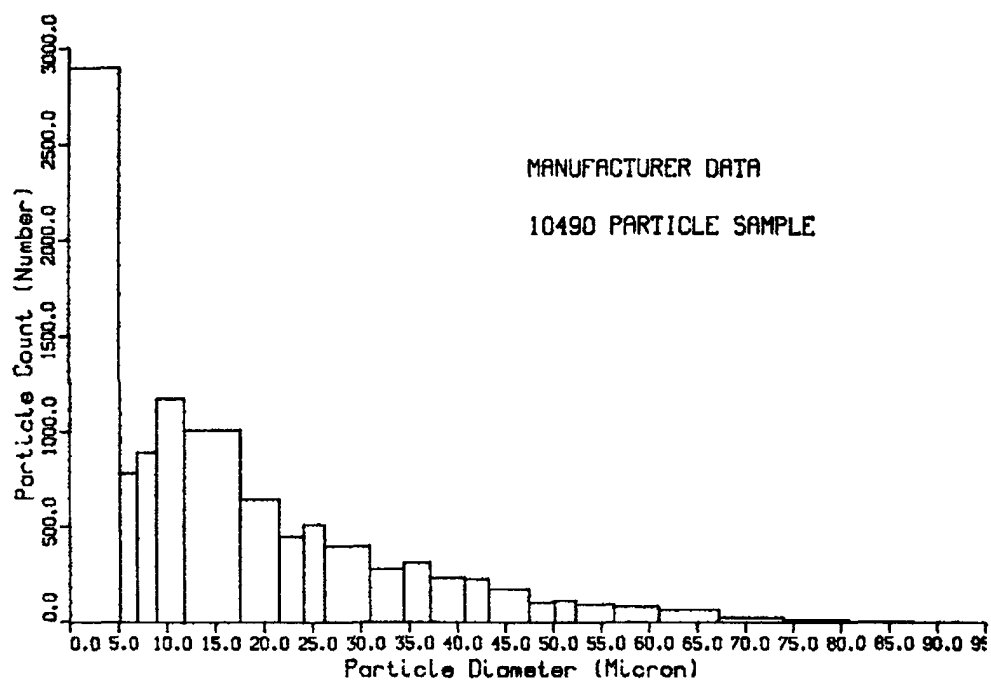
Using the hologram reconstruction system, the smallest particle resolved was on the order of $20 \mu\text{m}$. Adjusting the manufacturer's data for this resolution threshold produced the histogram of Fig. 44a. The measured histogram from a hologram reconstruction of the calibration array with 228 particles in the field of view is shown in Fig. 44b. Again the lower size bin was not empty due to quantization effects and noise, but the general shape of the curve was in agreement. From these preliminary results, it was decided to explore the loss of resolution in the processing steps further by using the Air Force Resolution chart as an object, since it has more steps in its quantization of resolution. Additionally, other techniques for the reduction of speckle were required for small objects since it was suspected that the smaller objects might have been removed by the blur filter steps. Also, the ITEX/PC subroutine package became commercially available in FY86, allowing the handling of full screen images in a time-efficient manner. The work on speckle reduction is reported below. The work on expanding the image handling capability to full screen images and studying the loss of resolution at each step of the processing is in progress in FY87.

SPECKLE

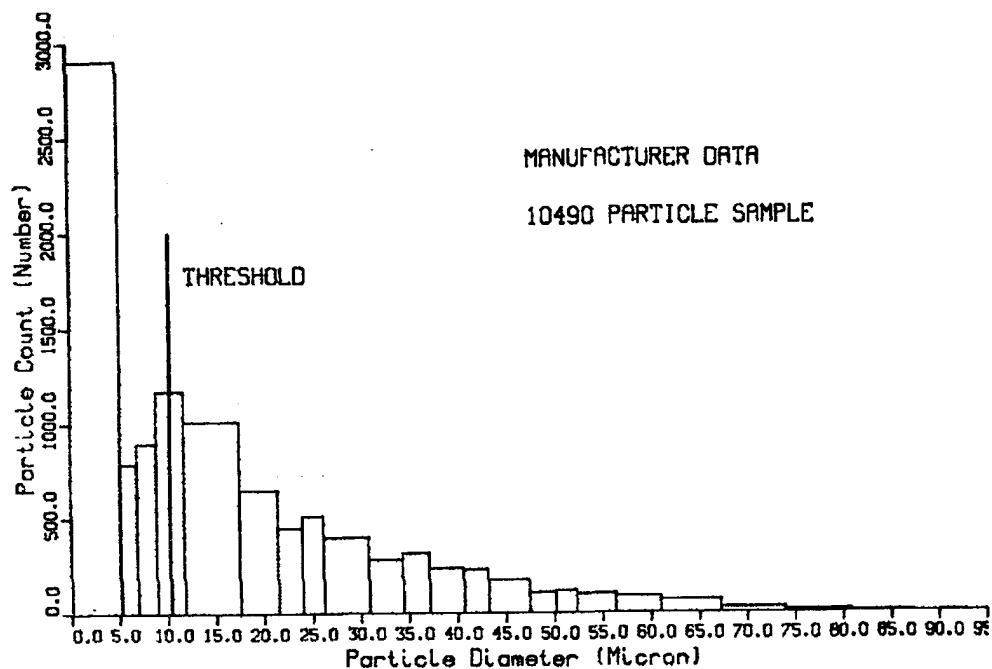
A problem arises during the processing of the digital image. During laser reconstruction of the hologram, speckle noise is introduced. This speckle noise can be of the same size as some of the smaller particles of interest, and so cause a faulty count in the number of features present.

In an attempt to reduce the speckle, Redman (Ref. 25) investigated a spinning mylar disk, averaging techniques, blurring and lowpass filtering. Twenty microns was the best resolution that was achieved by these means. Some of the loss in resolution may have been due to the optics involved; nevertheless, it became necessary to explore other means of filtering out the speckle to get the best possible resolution.

Edwards (Refs. 19) explored three speckle reduction algorithms suggested by work in the field of synthetic aperture radars. The initial step was to

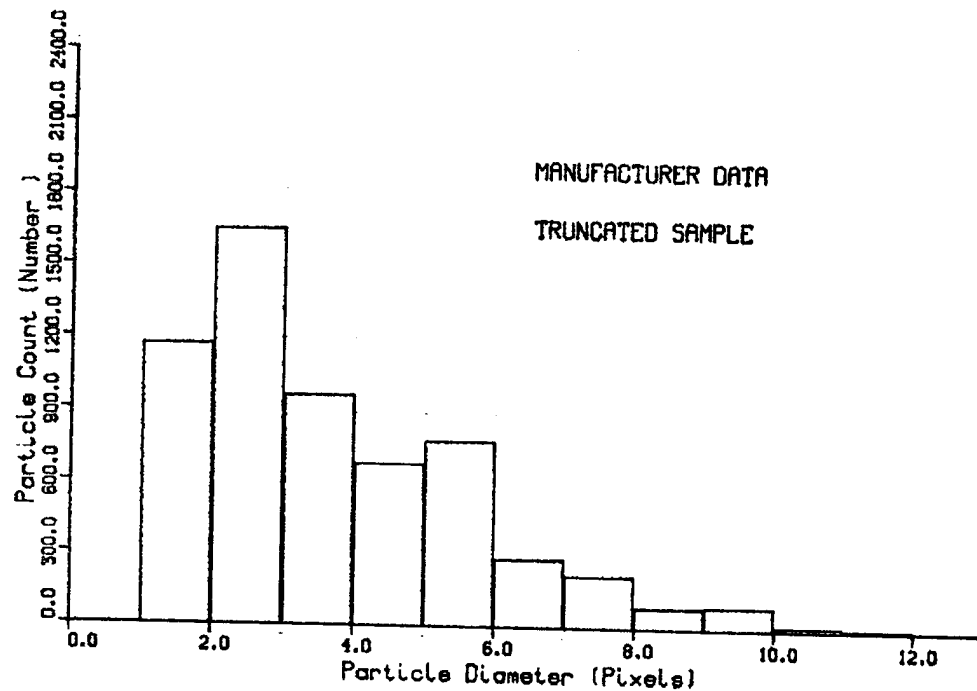


(a)

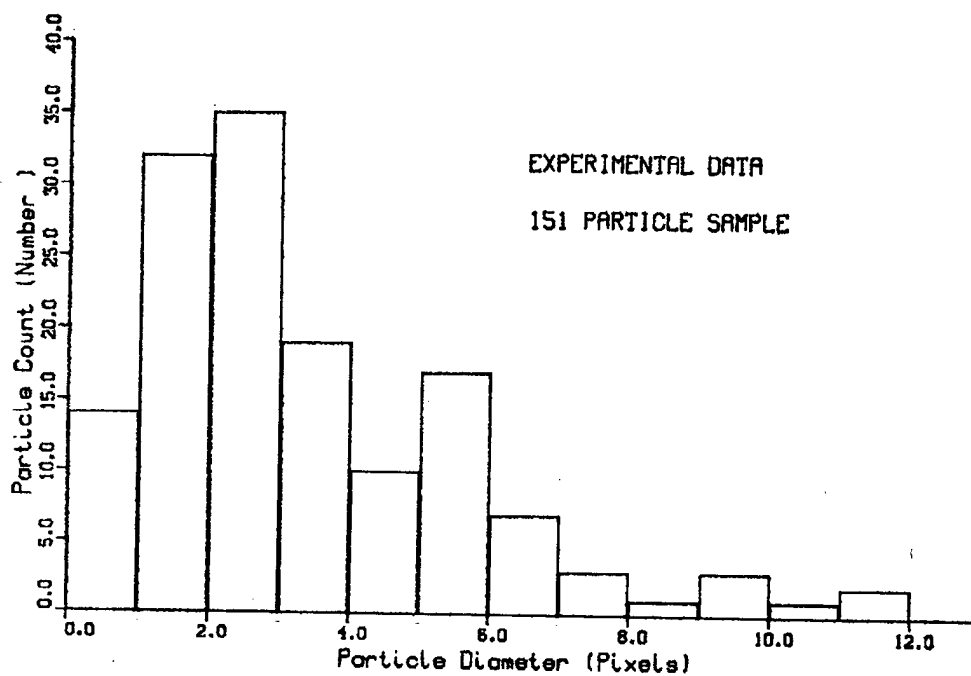


(b)

Figure 42. Histograms of (a) manufacturer's data, and
(b) manufacturer's data with resolution threshold shown

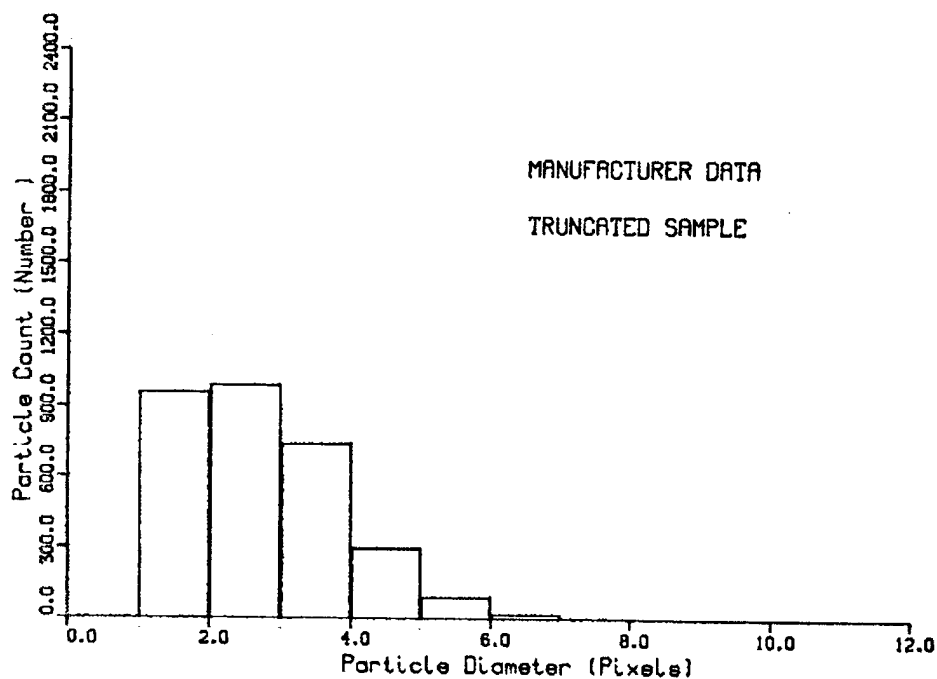


(a)

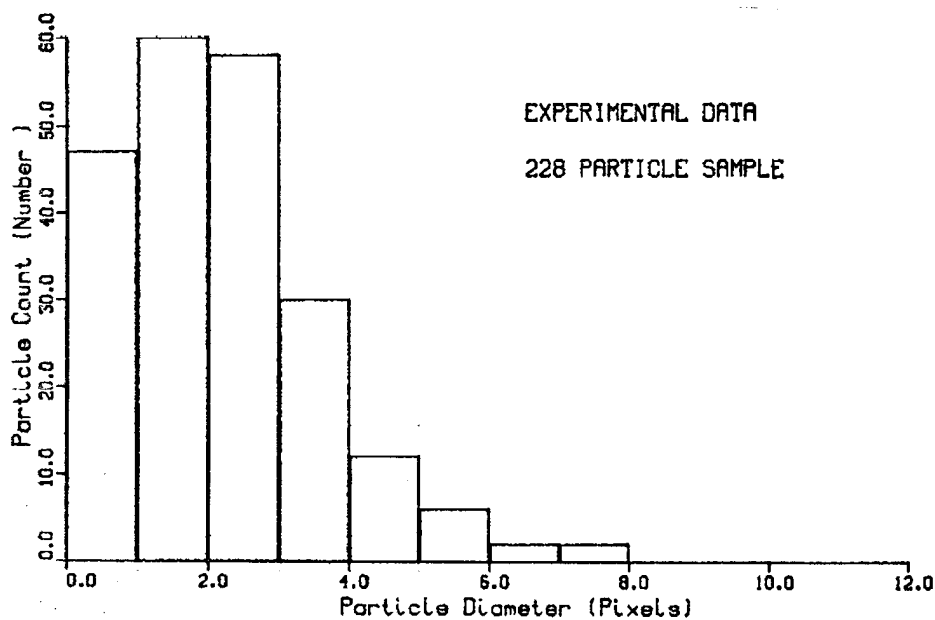


(b)

Figure 43. Histograms of (a) truncated manufacturer's data, and
(b) measured data truncated by resolution threshold



(a)



(b)

Figure 44. Histograms of (a) manufacturer's data with a 20 μm size threshold, and (b) experimental data from a hologram reconstruction

write computer programs to support each algorithm. Once the programs were running, a comparison was made to find which of the three was best at reducing speckle while retaining as much resolution as possible.

Speckle has the characteristics of random multiplicative noise in the sense that the noise level increases with the average gray level of a local area (Ref. 27). The presence of speckle reduces one's ability to resolve fine detail. Figure 45 shows an image with and without speckle present. It can be seen how the speckle is easily confused with the smaller feature particles.

As a figure of merit in determining the amount of speckle reduction, the "speckle index" was used. In Reference 28, Crimmins showed that the ratio of local deviation to local mean was a reasonable measure, due to the multiplicative nature of speckle noise.

To compute the speckle index, a Fortran subroutine was written. The algorithm used was (Ref. 28):

$$\text{speckle index} = \frac{1}{MN} \sum_{x=1}^M \sum_{y=1}^N \frac{\text{dev}}{\text{mean}} \quad (8)$$

where:

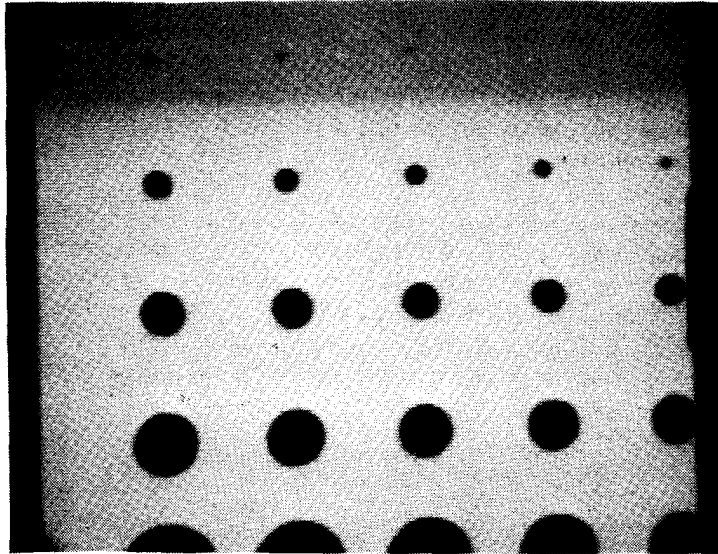
$$\text{dev} = \max_{-1 \leq a, b \leq 1} p(x+a, y+b) - \min_{-1 \leq a, b \leq 1} p(x+a, y+b) \quad (9)$$

$$\text{mean} = \frac{1}{9} \sum_{a, b=-1}^1 p(x+a, y+b) \quad (10)$$

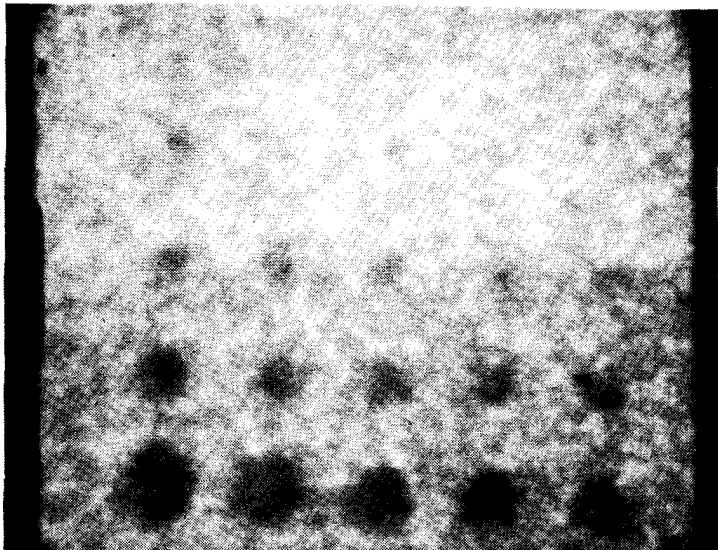
In the above equations, M and N are the dimensions of the array in the x and y directions, and p(x,y) is the gray level of an individual pixel located at x and y.

In simple terms, the local deviation is found by subtracting the smallest gray level of a particular pixel and its eight immediate neighbors from the largest gray level of the same nine pixels. The local mean is the average of the nine gray levels.

The subroutine was run with various values of M and N to determine good values. From Figure 46, it can be seen that a small array can distort the calculation if there is a sharp local disturbance. The values M = N = 240 were chosen as representative array dimensions for speckle index calculations. This size represents about 23% of the visible screen, yet does not take an excessive amount of time to calculate.



(a)



(b)

Figure 45. (a) Sample Image without Speckle,
(b) Same Image with Speckle Noise

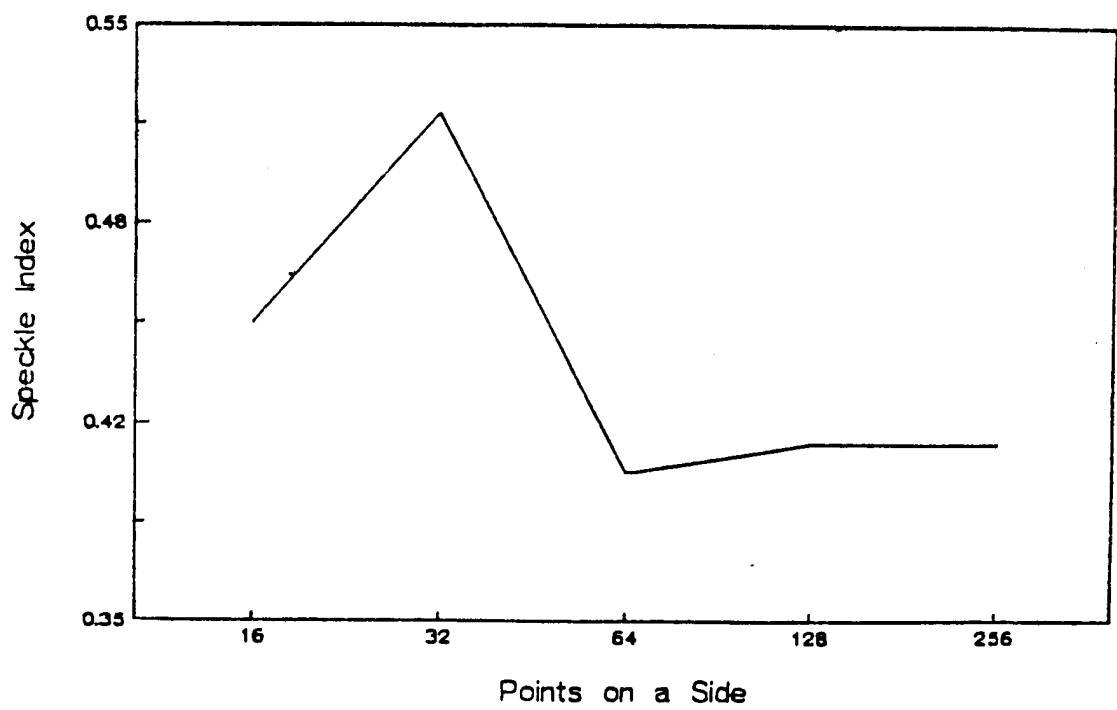


Figure 46. Speckle Index as a Function of Sample Size

The IBM PC/AT with the math coprocessor returns the speckle index of an image to the calling program in 75 seconds. Values for speckle index range from over 1.0 (rarely) to a theoretical limit of zero. The value of zero could only be achieved if the entire image was filtered to the point where every pixel had the same gray level. This is, of course, uninteresting.

SPECKLE REDUCTION FILTERS

Three filters were implemented in software and will now be discussed. All of them call subroutines "speckle" and "trash" to calculate the speckle index and threshold the image, respectively.

Two filters depend to a certain degree on the statistics of the image. The third filter uses a geometric hulling algorithm.

The Sigma Filter

The first speckle reduction filter is based on the standard deviation of a Gaussian distribution. By definition, 95.5% of all the pixels fall within two standard deviations on either side of the mean. Any pixels within two standard deviations of a given pixel's gray level are included in an averaging scheme, whereas those outside the "2-sigma" range are excluded. (Ref. 28)

Obviously, the standard deviation of the image must be known beforehand. ImageAction was used to find standard deviations and histogram plots very quickly and easily.

If a particular pixel is considerably different from its neighbors, perhaps none of the neighbors will be within the 2-sigma range. This would indicate a very sharp feature. To avoid the possibility that this sharp feature will not be subject to the averaging process at all, a cutoff is established. If the total number of pixels inside the 2-sigma range is less than this minimum cutoff number (2 was chosen), the four-neighbor average then replaces the central pixel's gray level value.

The sigma filter program uses the algorithm as follows (Ref. 29):

$g(x,y) =$

$$\frac{\sum_{i=x-2}^{x+2} \sum_{j=y-2}^{y+2} \delta(i,j)p(i,j)}{\sum_{i=x-2}^{x+2} \sum_{j=y-2}^{y+2} \delta(i,j)} \quad \text{if } \sum_{i=x-2}^{x+2} \sum_{j=y-2}^{y+2} \delta(i,j) > 2 \quad (11)$$

$$\frac{p(x-1,y)+p(x+1,y)+p(x,y)+p(x,y-1)+p(x,y+1)}{5}$$

otherwise,

where:

$p(x,y)$ = gray level of a pixel in 5x5 local array,

$g(x,y)$ = gray level of the filtered central pixel,

σ = standard deviation, and

$$\delta(x,y) = \begin{cases} 1 & \text{if } (1-2\sigma)p(x,y) < p(i,j) < (1+2\sigma)p(x,y) \\ 0 & \text{otherwise.} \end{cases} \quad (12)$$

By altering the value of σ , varying degrees of filtering result. If σ is increased, the sigma range is increased, and so more pixels are included in the average. For this investigation, however, the true standard deviation of each image was used when it was filtered.

For illustration of the sigma filter's effectiveness, images of the Air Force Resolution Target are presented. Figure 47 shows an image before and after two iterations of the filter. Visually the speckle has been reduced considerably, although the edges have been blurred and the resolution has decreased somewhat.

Histograms of these two images (Figure 48) show some separation between features and the background speckle after filtering. A threshold at 140 is suggested.

When this threshold is applied (Figure 49), the effectiveness of the sigma filter is most dramatically displayed. Now it is much more evident that good data can be retrieved from the filtered image, whereas the excessive speckle in the unfiltered image would lead to faulty data detection.

The Local Statistics Filter

This filter uses local estimates of the mean and variance in a 5x5 window about the central pixel in question (Ref. 29). These local statistics are used to calculate a weight k . The k value then determines where the new gray level of the central pixel will be placed: near the original value of the central pixel, near the linear average of all pixels in the 5x5 array, or somewhere in-between.

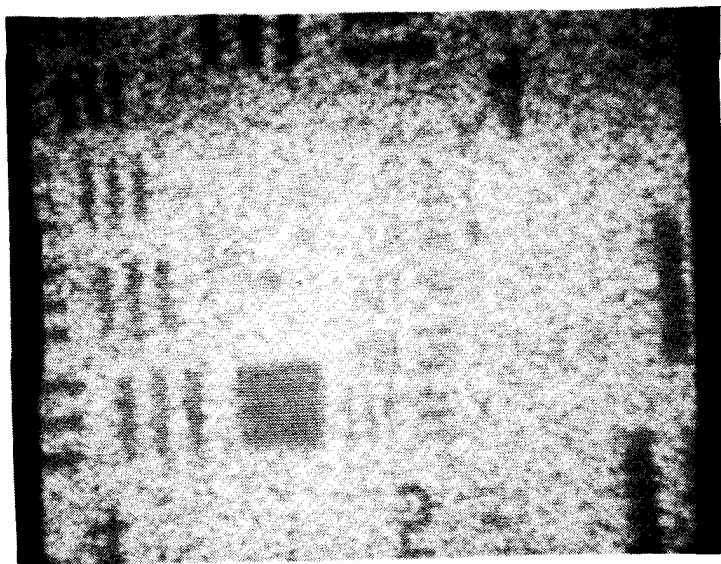
Throughout this algorithm, $p(x,y)$ represents unfiltered pixels and $g(x,y)$ represents the filtered central pixel. To compute the filtered gray level of a pixel using the local statistics method, the local mean $E\{g(x,y)\}$ and variance $\text{var}\{g(x,y)\}$ must first be estimated (Ref. 29):

$$E\{g(x,y)\} \approx \frac{1}{25} \sum_{i=x-2}^{x+2} \sum_{j=y-2}^{y+2} p(i,j) \quad (13)$$

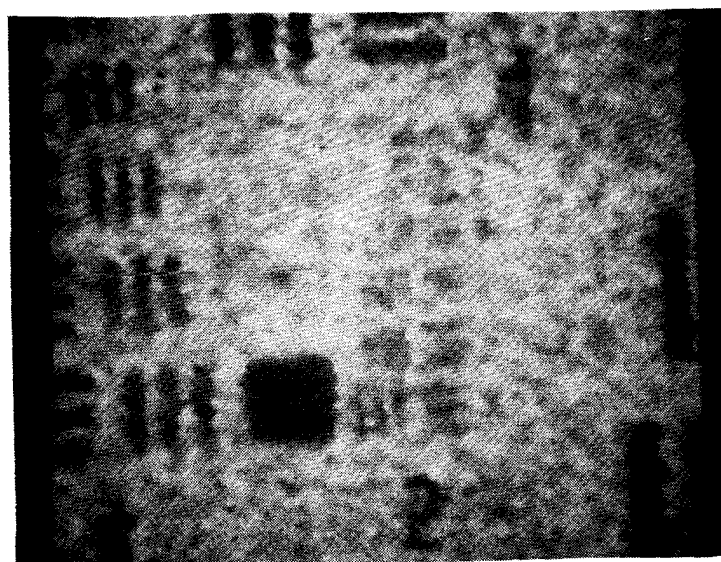
$$\text{var}\{g(x,y)\} \approx \frac{\text{var}\{p(x,y)\} + E^2\{g(x,y)\}}{\sigma^2 + 1} - E^2\{g(x,y)\} \quad (14)$$

where:

$$\text{var}\{p(x,y)\} \approx \frac{1}{25} \sum_{i=x-2}^{x+2} \sum_{j=y-2}^{y+2} [p(i,j) - E\{g(x,y)\}]^2 \quad (15)$$

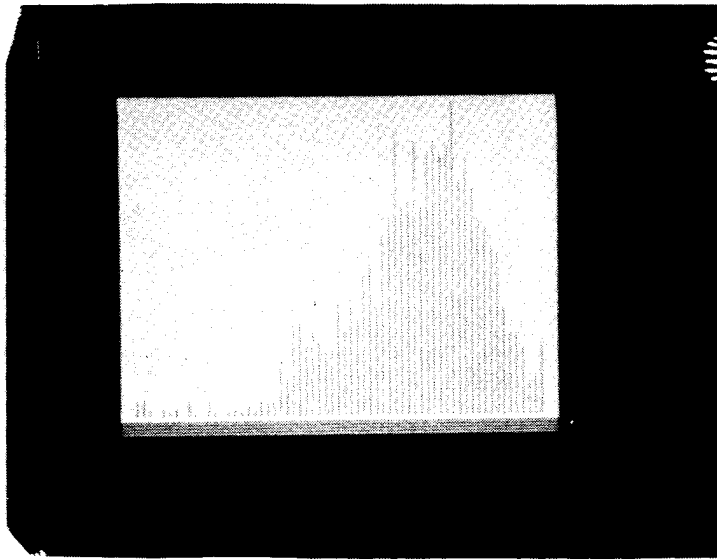


(a)

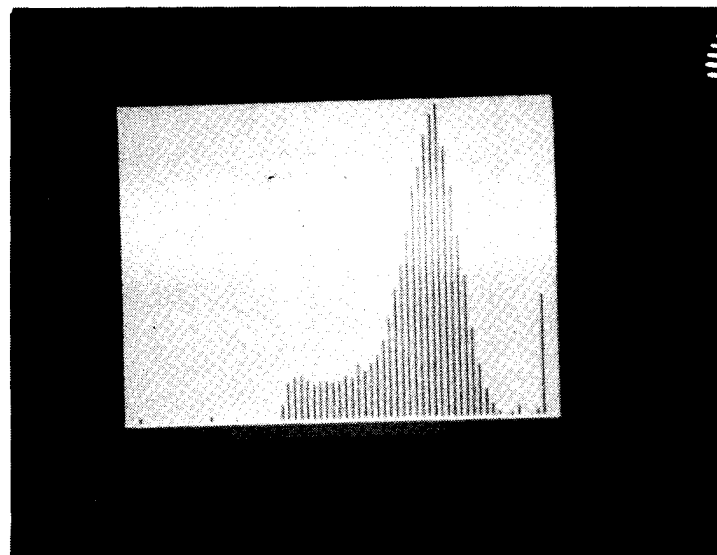


(b)

Figure 47. (a) Unfiltered Image of the Air Force Resolution Bar Target (S.I.=0.30549), (b) Same Image Filtered with the Sigma Filter (2 iterations, S.I.=0.10278)

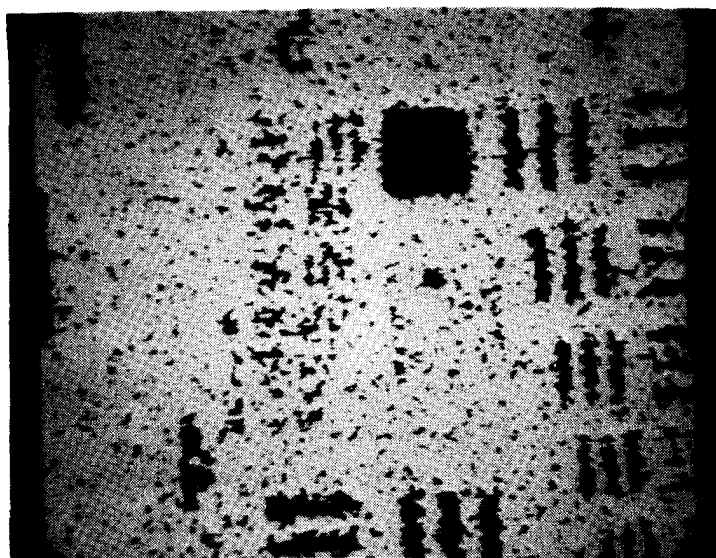


(a)



(b)

Figure 48. (a) Histogram of the Unfiltered Image,
(b) Histogram of the Sigma Filtered Image



(a)



(b)

Figure 49. (a) Unfiltered Image Thresholded at 140,
(b) Sigma Filtered Image Thresholded at 140

The weight k may then be calculated as:

$$k = \frac{\text{var}\{g(x,y)\}}{\sigma^2 E^2\{g(x,y)\} + \text{var}\{g(x,y)\}} \quad (16)$$

Finally, the estimate of $g(x,y)$ is:

$$g(x,y) = E\{g(x,y)\} + k\{p(x,y) - E\{g(x,y)\}\} \quad (17)$$

From close scrutiny of the algorithm, some of the equations may be better understood. Equation 13 states that the local mean is the average of the 25 pixels in the 5x5 local array. Equation 14 is the variance of the unfiltered pixels in the 5x5 array; the mean value of the local array from Equation 13 is subtracted from each of the pixels in turn. These differences are squared and then summed over the entire array. For more detail on how the remaining equations were developed, see Reference 29.

Consider a region of an image which is flat, meaning adjacent pixels have about the same gray level. Here, the variance approaches zero, and so k approaches zero. The new estimate of $g(x,y)$ is, therefore, close to the mean of the local 5x5 array. Consider now a region of high contrast, say the edge of a particle. Here, k approaches one and so $g(x,y)$ is close to the value of the central pixel. The filter, therefore, has a marked tendency toward the retention of high contrast edges (Ref. 29).

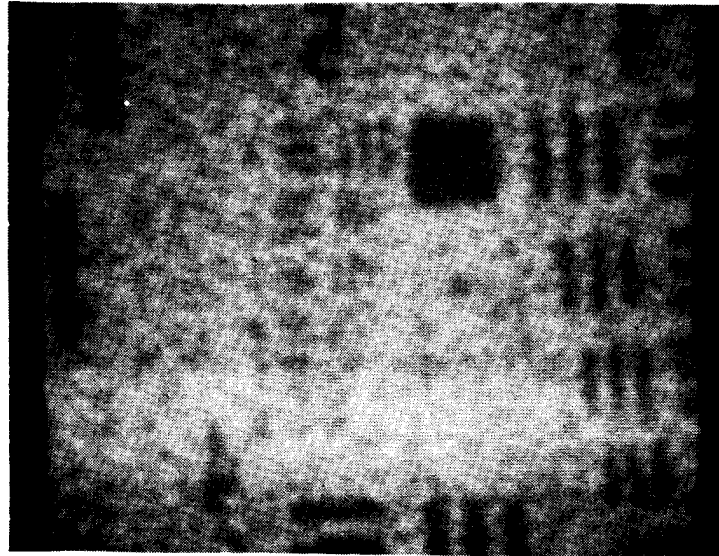
Figure 50 shows the Air Force Resolution Target after two iterations of the local statistics filter, both before and after thresholding at 140.

The Geometric Filter

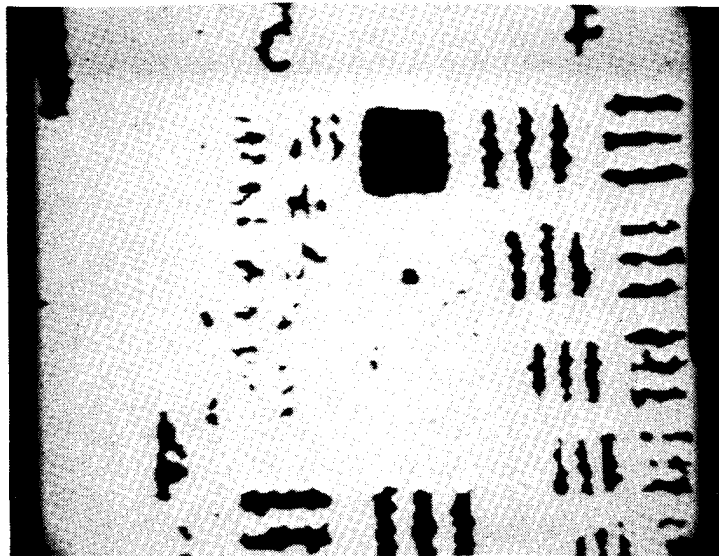
Whereas the previously discussed filters depend to a certain degree upon the statistics of the image to be filtered, the geometric filter is based on nonlinear geometric concepts.

The algorithm was developed in References 27 and 28. It is a one-dimensional routine which is run horizontally, vertically and then in the two diagonal directions. It applies, in each direction, a geometric hulling algorithm to the image and then to the image's complement. The algorithm (Ref. 27) for this filter follows:

1. Let $a = 1$, $b = 0$. (This sets the values for a horizontal run.)



(a)



(b)

Figure 50. (a) Image Filtered with the Local Statistics Filter
(2 iterations, S.I.=0.11484), (b) The Local Statistics Filtered Image
Thresholded at 140

2. Let $c = 3$. (This is a counter to determine when to change directions.)
3. Let $d = 1$. (This controls whether the image or its complement is being filtered.)

4. Compute

$$g(x,y) = \max[p(x,y), \min\{p(x-a,y-b)-1, p(x,y)+1\}]$$

$$\text{for } 1 \leq x \leq M, 1 \leq y \leq N. \quad (18)$$

5. Compute

$$p(x,y) =$$

$$\max [g(x,y), \min\{g(x-a, y-b), g(x,y) + 1, g(x+a, y+b) + 1\}]$$

$$\text{for } 1 \leq x \leq M, 1 \leq y \leq N. \quad (19)$$

6. If $d = 1$, let $a = -a$, $b = -b$, $d = 0$ and go to Step 4.
If $d = 0$, let $d = 1$ and go to Step 7.

7. Compute

$$g(x,y) = \min[p(x,y), \max\{p(x-a, y-b) + 1, p(x,y) - 1\}]$$

$$\text{for } 1 \leq x \leq M, 1 \leq y \leq N. \quad (20)$$

8. Compute

$$p(x,y) =$$

$$\min[p(x,y), \max\{g(x-a, y-b), g(x,y) - 1, g(x+a, y+b) - 1\}]$$

$$\text{for } 1 \leq x \leq M, 1 \leq y \leq N. \quad (21)$$

9. If $d = 1$, let $a = -a$, $b = -b$, $d = 0$ and go to Step 7.
If $d = 0$, let $d = 1$, and go to Step 10.
10. If $c = 3$, let $a = 0$, $b = 1$, $c = 2$ and go to Step 4. (This sets up a vertical run.)
If $c = 2$, let $a = 1$, $b = 1$, $c = 1$ and go to Step 4. (This sets up a diagonal run.) If $c = 1$, let $a = 1$, $b = -1$, $c = 0$ and go to Step 4. (This sets up the other diagonal.)

11. If $c = 0$, stop.

The algorithm used exhibits the interesting property that it will allow a certain curvature in the terrain, but will tear down anything more drastic. With a few exceptions (Ref. 27), a curve sharper than 45 degrees at any vertex will be filtered. What this means is that the narrow valleys comprising speckle will be filled in and the walls torn down after sufficient iterations of the filter. Of course, the objects of interest that should be preserved are also filled in and torn down, but at a much slower rate. Generally, the larger and darker the feature, the more slowly it will be degraded.

If an object of interest is almost as narrow as the speckle, they both will be reduced at about the same rate. Hopefully, the object is much darker than the speckle, so the speckle will be beaten down after a number of iterations, leaving the object of interest largely intact.

Figure 51a shows the Air Force Resolution Chart after three iterations of the geometric filter. Figure 51b shows the same filtered image thresholded at a gray level of 140.

COMPARISON OF THE FILTERS

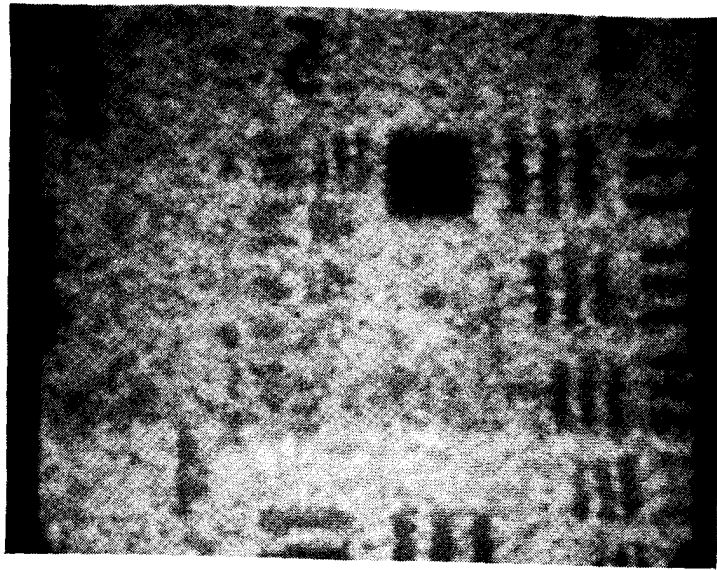
This section will compare the three filters using the speckle index as a figure of merit in gauging how much speckle has been removed. The filters will be compared in how much speckle they remove per iteration, the time per iteration, histogram differences, and, of course, visual differences.

Speckle Index Comparison

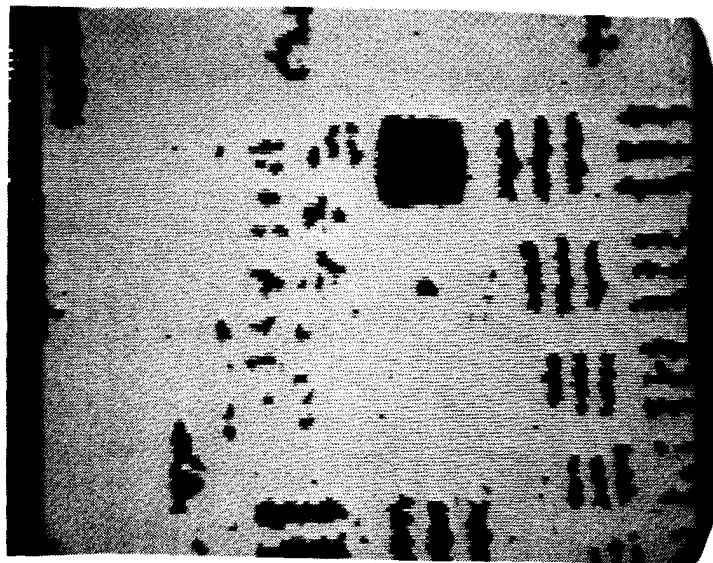
All three filters reduce speckle at their own rate. Figure 52 shows this fact. The sigma and local statistics filters both reduce speckle by almost a factor of two after only one iteration, but then dramatically "slow down" with increased iterations. This may be attributed to the fact that both filters are actually various themes on the blurring technique. More iterations serve to merely increase the blur.

Figure 52 shows that the geometric filter's curve is more gradual, allowing the user to stop at a less severe level of filtering. This is a particularly desirable trait, because resolution degradation becomes a problem after only a few iterations. It should be noted that filtering cannot stop at an arbitrary value of speckle index, only at discrete levels depending on how many iterations have occurred. It is foreseeable that a given filter may allow a degree of speckle reduction not achievable by the others.

On the basis of Figure 52, the geometric filter ranks first in its ability to control the amount of speckle reduction, followed by the local statistics filter.



(a)



(b)

Figure 51. (a) Image Filtered with the Geometric Filter
(3 Iterations, S.I.=0.12918), (b) Geometric Filtered Image
Thresholded at 140

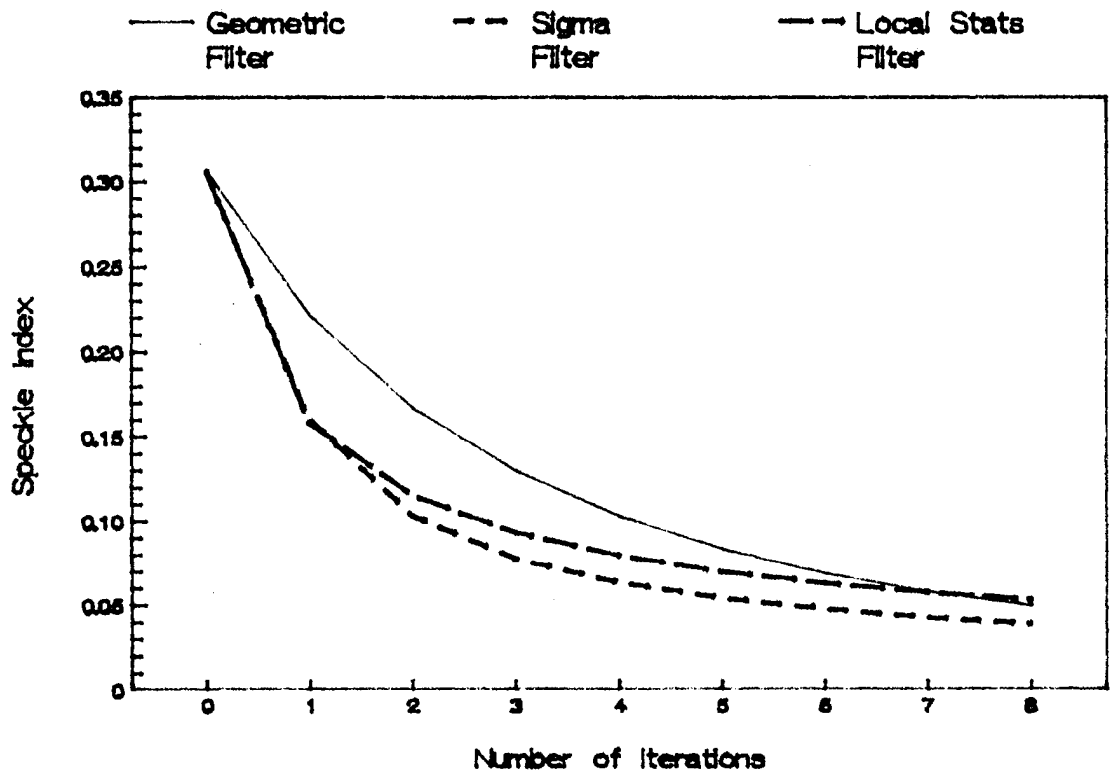


Figure 52. Speckle Reduction Comparison

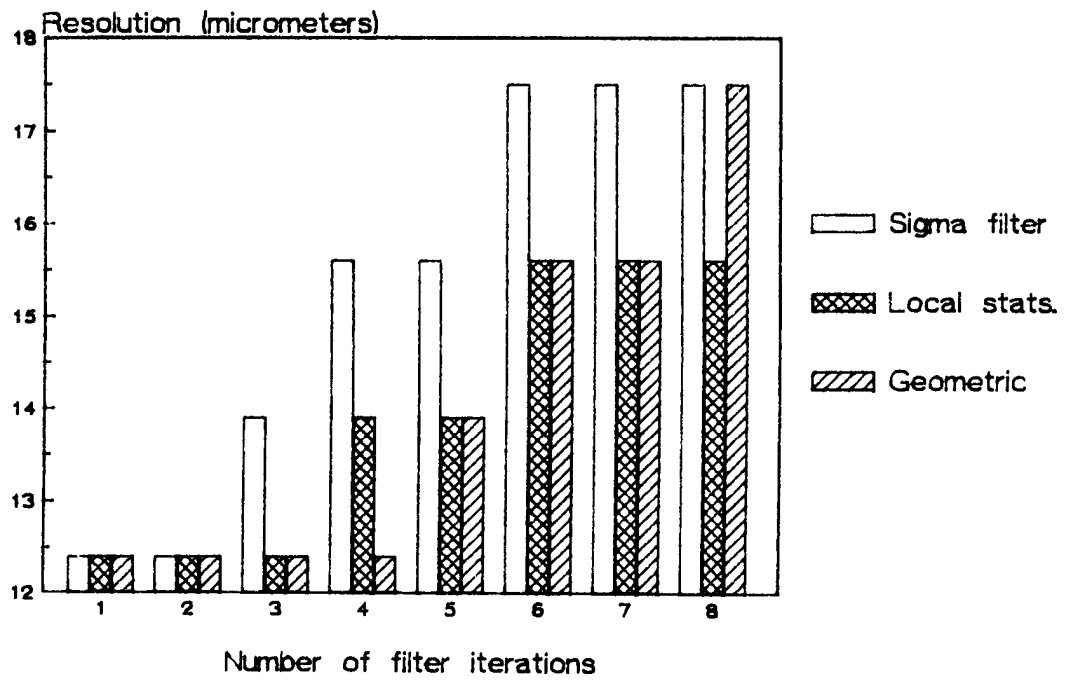


Figure 53. Resolution degradation of images

Resolution Comparison

Speckle reduction is a fundamental tradeoff against image resolution. Figure 53 shows a comparison of the measured resolution for each of the filter types. The horizontal axis shows the number of iterations of the filter. (Each iteration reduces the speckle further.) It is observed that the resolution degrades from about 12 μm to almost 18 μm after several iterations of the filters. The geometric and local statistics filters are comparable to each other up through seven iterations, and are superior to the sigma filter in preserving the resolution of the image.

Time Comparison

The times for an iteration of each filter are shown in Table 10. The local statistics filter is slow due to the nested do-loops, frequent calls to subroutines and large number of calculations required inside each do-loop. It should be noted that speed is of secondary importance since there is no requirement in this application to achieve results within a given time limit. Also, dedicated image-processing equipment can do the calculations much more efficiently and faster. For example, Reference 29 reports times of 14 seconds per iteration for the geometric filter using a VAX 11/780 and DeAnza IP-5500 digital video processor.

TABLE 10

TIME PER ITERATION (512 x 512 IMAGE, PC/AT)

<u>FILTER</u>	<u>TIME</u>
Sigma	7 min, 20 sec
Geometric	18 min, 50 sec
Local Statistics	39 min, 45 sec

Visual Comparison

The ultimate test of any procedure dealing with images is how the image looks to the viewer. Comparisons of this type are difficult to justify, for each person sees an image slightly differently. Nevertheless, based on numerous runs of the filters, the geometric filter is judged best at retaining the edges, basic shape and size of objects of interest while beating down the speckle. This can be seen by close comparison of Figures 47b, 50a, and 51a. All three Figures are close in speckle index, yet the local statistics and sigma filters tend to smear and spread particle edges more than does the geometric filter. This observation has been verified in runs using other images as well.

Once the threshold at 140 is applied (Figures 49b, 50b, and 51b), the sigma filter is definitely seen as the inferior of the three. The other two are very close. Examination reveals a few small particles of speckle that the geometric filter failed to eliminate which the local statistics filter successfully handled. This is a consequence of the filtering stopping at discrete levels. In most other cases, the geometric filter is superior.

Histogram Comparison

All three filters produced histograms generally similar in shape and distribution. Figure 54 shows the histograms of two filtered images. Notable differences include the geometric filter's reduction of the spike at 255, the way it retained virtually intact the darker features and its more pronounced "valley" between the two "humps".

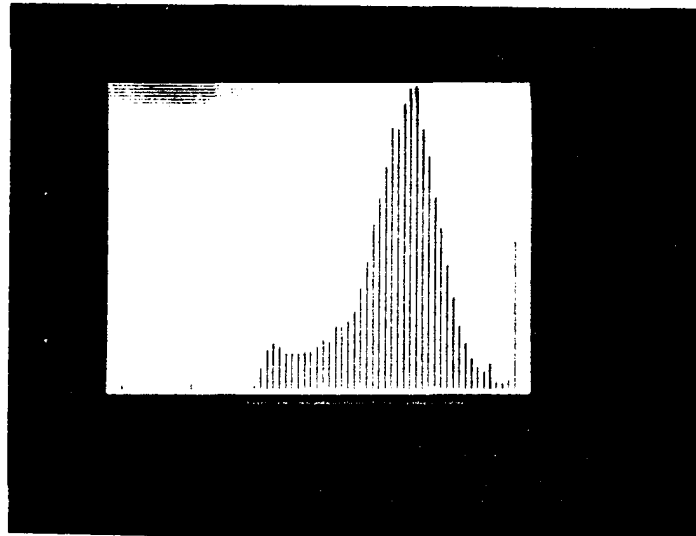
The claim was made earlier that the geometric filter had a tendency to reduce smaller (hopefully speckle) particles much faster than the dark features. The retention of the darker pixels in the histograms is evidence that this claim is valid.

All the filtered histograms pointed to a threshold at about 140. Thus, this was the value used on all the images, including the original, for comparison purposes.

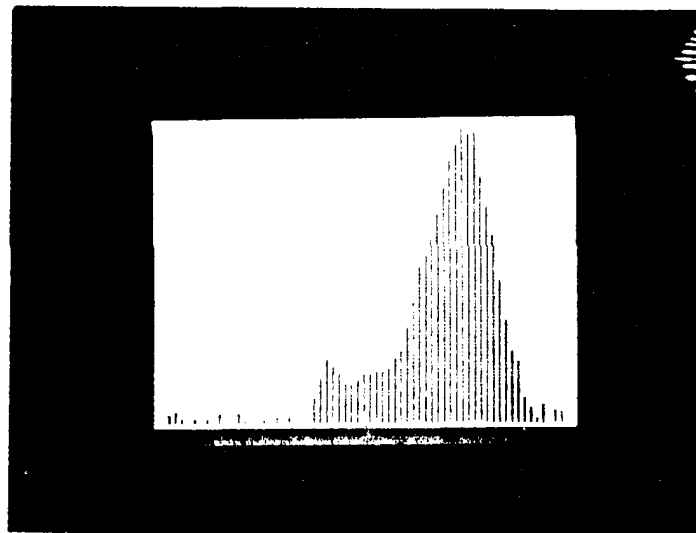
CONCLUSIONS, RECOMMENDATIONS AND CURRENT EFFORTS

High intensity white-light and monochromatic light have been used to eliminate the flame envelopes that surround burning aluminum particles from the recorded images in high speed motion pictures in an earlier investigation [Ref. 17].

Light scattering measurements have been used to successfully measure the change in D_{32} across the exhaust nozzle of a small solid propellant rocket motor. However, the present optical arrangement limits the minimum particle size for accurate measurement to approximately three microns. This can be improved by increasing the diameters of the motor windows (if they can then be kept clean) and/or by changing the size and location of the transform lens. Measurements were readily made in the exhaust jet, but measurements through the motor windows proved to be much more difficult. This difficulty resulted both from the long optical path through the particles and the slight deflection of the laser beam when pressure gradients were present. Neutral burns and shorter optical paths can be more easily attained in small motors if they are two-dimensional. In addition, the effects of slight movements of the illumination beam on the scattered profile would be minimized through the use of ring diode arrays (vs. the narrow linear diode used in the present apparatus). A wider spacing or increased number of the diodes would also permit a wider range of scattering angles to be measured, resulting in smaller particles being detected. The latter is currently being implemented through the use of two-inch (vs. the current one-inch) diode arrays.



(a)



(b)

Figure 54. (a) Histogram of Local Statistics Filtered Image,
(b) Histogram of Geometric Filtered Image

Injection of particles with known size distribution and composition into the port of a burning, non-metallized propellant was also shown to be a viable means for separating the gas phase particle behavior from the propellant surface processes.

In earlier investigations [Refs. 17 and 18] good quality holograms of burning propellant strands were obtained with pressures to 68 atm and aluminum loadings to 15%. Success was also attained using miniature 2-D motors with (1) pressures to 59 atm and aluminum loadings to 5% and (2) pressures to 33 atm and aluminum loadings to 10%.

In the present investigation, good quality holograms were obtained in a small 3-D motor using 2% aluminized propellant to pressures of 280 psia. Neutral burning and reduced optical depths would also greatly improve the obtainable holographic data.

In order to continue to improve the capabilities of the present diagnostic apparatus for obtaining particle size data in the solid propellant rocket motor environment several improvements have been recently made.

- (1) A new 2-D motor has been designed (and is being constructed) which will provide a neutral burn with burn times exceeding two seconds, large windows for light scattering measurements and holography, and a much reduced (0.25") optical depth through the particle laden flow.
- (2) A Malvern particle sizer has been purchased and is being used to measure particle size distributions. This instrument uses a ring diode array and is said to have a resolution limit of 0.5 microns. It also permits multiple, rapid pulses to be made during a single firing.
- (3) A two-inch linear diode array will replace the one-inch array, allowing scattered light to be recorded within a 6° increment (vs. the present 3° increment.) This, coupled with the larger windows, will permit particles as small as 1 micron to be detected while maintaining the ability to accurately detect the larger particles.

The IBM PC/AT with dedicated software and hardware is a viable system to reduce speckle in reconstructed holograms. The ITEX/PC software with the PC Vision frame-grabber board may be used in conjunction with Fortran programs to achieve the filtering desired.

While all three filters are superior to current techniques, the geometric filter has been found to be the best of the three investigated. It combines the ability to hold the edges and shape of objects with the desirable trait of less filtering per iteration. In this way, the user has more control over the amount of filtering to be done and to what degree the speckle will be reduced.

While the geometric filter has been found to be the best overall filter, it may not be superior in every particular circumstance. It has been noted that due to the discrete jumps in speckle index which occur after every iteration, one filter may be able to reach the region of optimum filtering when another cannot. For this reason, the local statistics filter should be used

along with the geometric filter and the results after 2 or 3 iterations compared.

Resolution of the original image was about 12 microns. This was degraded to about 14 microns in the filtered images. It is doubtful that much more improvement can be made toward reducing the speckle degradation due to filtering. Any further resolution improvements most likely will have to occur in the recording and reconstruction process, and better optics. Some improvements have been made recently in this area. As discussed above, resolutions of 8 microns, and in certain cases 4 microns, have been achieved. Taking into account the degradation after filtering, a conservative estimate of 10 microns resolution is now possible in the finished filtered and thresholded image.

REFERENCES

1. George, D., Recent Advances in Solid Rocket Motor Performance Prediction Capability, AIAA Paper No. AIAA-81-033, 19th Aerospace Sciences Meeting, Jan 12-15, 1981.
2. Hermesen, R.W., Aluminum Oxide Particle Size for Solid Rocket Motor Performance Prediction, AIAA 19th Aerospace Sciences Meeting, Jan 12-15, 1981.
3. Dobbins, R.A., "Remote Size Measurements of Particle Product of Heterogeneous Combustion," Eleventh Symposium (International) on Combustion, The Combustion Institute, 1967, p. 921.
4. Dobbins, R.A. and Strand, L.D., "A Comparison of Two Methods of Measuring Particle Size of Al_2O_3 Produced by a Small Rocket Motor," AIAA J. Vol. 8, pp. 1544-1550, 1970.
5. Cashdollar, K.L., Lee, C.K. and Singer, J.M., "Three Wavelength Light Transmission Technique to Measure Smoke Particle Size and Concentration," Applied Optics, Vol. 18, No. 11, pp. 1763-1769, June 1979.
6. Gumprecht, R.O. and Sliepcevich, C.M., "Scattering of Light by Large Spherical Particles," J. Physical Chem., Vol. 57, pp. 90-94, Jan 1953.
7. Dobbins, R.A., Crocco, L. and Glassman, I., "Measurement of Mean Particle Size of Sprays from Diffractively Scattered Light," AIAA J. Vol. 1, No. 8, pp. 1882-1886, 1963.
8. Roberts, J.H. and Webb, M.J., "Measurements of Dropplet Size for Wide Range Particle Distributions," AIAA J., Vol. 2, No. 3, pp. 583-585, 1964.
9. Mugele, R.A. and Evans, H.D., "Dropplet Size Distribution in Sprays," Ind. and Eng. Chem., Vol. 43, pp. 1317-1324, 1951.
10. Dobbins, R.A. and Jizmagian, G.S., "Optical Scattering Cross-Sections for Polydispersions of Dielectric Spheres," J. Optical Soc. of Am., Vol. 56, No. 10, pp. 1345-1350, 1966.
11. Dobbins, R.A. and Jizmagian, G.S., "Particle Measurement Based on Use of Mean Scattering Cross-Sections," J. Optical Soc of Am., Vl. 56, No. 10, pp. 1351-1354, 1966.
12. Hodkinson, J.R., "Particle Sizing by Means of the Forward Scattering Lobe," Applied Optics, Vol. 5, pp. 839-844, 1966.
13. Powell, E.A., Cassanova, R.A., Bankston, C.P. and Zinn, B., Combustion Generated Smoke Diagnostics by Means of Optical Measurement Techniques, AIAA Paper No. 76-67, AIAA 14th Aerospace Sciences Meeting, Jan. 1976.
14. Buchele, D.R., Particle Sizing by Measurement of Forward Scattered Light at Two Angles, NASA TP 2156, May 1983.

15. Van de Hulst, H. C., Light Scattering by Small Particles, John Wiley and Sons, Inc., New York, 1957.
16. Karagounis, S.G. et. al., An Investigation of Experimental Technique for Obtaining Particulate Behavior in Metallized Solid Propellant Combustion, AFRPL-TR-82-051, Air Force Rocket Propulsion Laboratory Report, Edwards AFB, July 1982.
17. Cramer, R.G. et. al., An Investigation of Experimental Techniques for Obtaining Particulate Behavior in Metallized Solid Propellant Combustion, AFRPL-TR-84-014, Air Force Rocket Propulsion Laboratory, Edwards AFB, CA, Feb. 1984.
18. Netzer, D.W. and Powers, J.P., Experimental Techniques for Obtaining Particle Behavior in Solid Propellant Combustion, AGARD-CP-391, No. 19, AGARD Conference on Smokeless Propellants, Florence, Italy, 12-13 Sept. 1985.
19. Edwards, T., Horton, K.G., Redman, D., Rose, J.S., Robin, J.B., Yoon, S.C. Powers, J.P., Netzer, D.W., Measurements of Particulates in Solid Propellant Rocket Motors, 23rd JANNAF Combustion Meeting, Langley, VA, 1986.
20. Hirleman, E.D., On-Line Calibration Technique for Laser Diffraction Dropplet Sizing Investments, ASME 83-GT-232.
21. Briones, R.A. and Wuerker, R.F., Instruction Manual for the Improved Ruby Holographic Illuminator, AFRPL-TM-78-11, Air Force Rocket Propulsion Laboratory, Edwards AFB, CA, July 1978.
22. Briones, R.A. and Wuerker, R.F., Operation Manual for the Lens Assisted Multipurpose Holocamera wit Reflected Light Option, AFRPL-TM-78-12, Air Force Rocket Propulsion Laboratory, Edwards AFB, CA, July 1978.
23. Netzer, D. W. and Powers, J. P., Particle Sizing in Rocket Motor Studies Utilizing Hologram Image Processing, presented at NASA Workshop on Data Reduction From Images and Interferograms, NASA/Ames Research Center, January 1985.
24. Shook, M. P., Computer-Controlled Image Analysis of Solid Propellant Combustion Holograms Using a Quantimet 720 and a PDP-11, M.S. Thesis, Naval Postgraduate School, Monterey, California, September 1985.
25. Redman, D. N., Image Analysis of Solid Propellant Combustion Holograms Using an ImageAction Software Package, M.S. Thesis, Naval Postgraduate School, Monterey, California, June 1986.
26. Imaging Technology Incorporated, The ITEX/PC Programmer's Manual, Part Number 47-s00005-01, Revision 1.1, September 1985.
27. Crimmins, T. R., "Geometric Filter for Speckle Reduction," Applied Optics, Vol. 24, No. 10, May 1985.

28. Crimmins, T. R., Geometric Filter for Reducing Speckle," Optical Engineering, Vol. 25, No. 5, May 1986.
29. Lee, J. S., "Speckle Suppression and Analysis for Synthetic Aperture Radar," Optical Engineering, Vol. 25, No. 5, May 1986.